DRAFT

Electronic Structure Properties and High Pressure Experimentation of Superconducting or Possibly Superconducting Systems

By

HAHNBIDT RHEE
B.S. (Iowa State University) 2004

DISSERTATION

Submitted in partial satisfaction of the requirements for the degree of

DOCTOR OF PHILOSOPHY

in

Physics

in the

OFFICE OF GRADUATE STUDIES

of the

UNIVERSITY OF CALIFORNIA

DAVIS

Approved:

Warren E. Pickett, Chair

Richard T. Scalettar

William J. Evans

Committee in Charge

2012

To my mother and father, Hyorim and Joo Yull,
and Casey

CONTENTS

LIST OF FIGURES

List of Tables

ABSTRACT OF THE DISSERTATION

Electronic Structure Properties and High Pressure Experimentation of Superconducting or Possibly Superconducting Systems

The following compounds were studied primarily for their superconducting properties or their potential to exhibit superconductivity.

The layered ternary *sp* conductor NaAlSi, possessing the iron-pnictide "111" crystal structure, superconducts at 7 K. Using density functional methods, it is shown that this compound is an intrinsic (self-doped) low-carrier-density semimetal with a number of unusual features. Covalent Al-Si valence bands provide the holes, and free-electron-like Al 3*s* bands, which propagate in the channel between the neighboring Si layers, dip just below the Fermi level to create the electron carriers. The Fermi level lies in a narrow and sharp peak within a pseudogap in the density of states. The small peak arises from valence bands which are nearly of pure Si, quasi-two-dimensional, flat, and coupled to Al conduction bands. The possibility of a non-phononic pairing mechanism is discussed.

The hexagonal Laves phase of $CaLi_2$, nonsuperconducting at ambient pressure, is a strong candidate for superconductivity at higher pressures. Zero resistance has been observed in $CaLi_2$ at pressures above 11 GPa and temperatures as high as 13 K. However, it hasn't been ruled out that superconducting elemental Li instead may be the source of the superconductivity. The crystallographic structure of $CaLi_2$ has been studied via powder x-ray diffraction at high pressures and low temperatures in a diamond anvil cell, in an attempt to create the structural phase diagram in the superconducting regime.

$PuPt_2In_7$ does not superconduct down to 2 K, despite its electronic and structural similarities with superconductor $PuCoGa_5$ and other Pu-based superconductors. Results of generalized gradient approximation (GGA)+U calculations on $PuPt_2In_7$ and on hypothetical $PuPt_2Ga_7$ are discussed. The strength of the c-f hybridization of $PuPt_2In_7$ is similar to that of $PuCoIn_5$, while $PuPt_2Ga_7$ is less localized and more like $PuCoGa_5$. The bare and f-weighted susceptibility within the constant matrix element approximation is calculated, showing a maximum at $q_x = q_y = 0.5$. A similar and slightly stronger maximum is also found in $PuCoGa_5$ and $PuCoIn_5$. The absence of superconductivity in $PuPt_2In_7$ is examined based on the results of the calculations.

Acknowledgments

I am first and foremost enormously indebted to my UC Davis advisors Warren Pickett and Richard Scalettar, whom I look up to not only as scientists but as exemplary figures of compassion. My deepest gratitude goes to Filip Ronning for his patience and ready willingness to mentor me. I cannot imagine where I would be if it were not for the consistent help I received from Erik Ylvisaker. I am also very thankful for all the guidance Will Evans, Hyunchae Cynn, and Choong-Shik Yoo have given me at LLNL. I will always be grateful to Lilia Boeri for her lessons and (really good) espresso. And I am blessed to have benefited from the fruitful discourses as well as friendships of the wonderful people that are Amy Lazicki, Bruce Baer, Zsolt Jenei, Ken Visbeck, Magnus Lipp, Chantel Aracne-Ruddle, Jae-Hyun Park Klepeis, Aman Kaur, Zhiping Yin, Swapnonil Banerjee, Brian Neal, Simone Chiesa, and Victor Pardo.

I want to thank my parents for their unconditional love and support and for believing in me when I doubted myself the most. I want to thank my little brother Hahnsoll, who's day of birth was the happiest day of my life. Finally, I thank Casey, the most selfless person I know, for making me the luckiest gal in the world, and for making me strive to be a better human being.

I acknowledge financial support from Stewardship Science Academic Alliance Program.

Chapter 1

Introduction

It is now well known that superconductivity is more prevalent, and comes in more flavors, than ever thought. In spite (and as a consequence) of this, it has become more challenging to devise a methodical approach to predicting new superconductors with higher T_c's; accidental discoveries, such as that of the iron-arsenide superconductors as late as 2008, still play a major part in influencing the field. The common goal of the bodies of work comprised in this thesis is to gain more insight into the underpinnings of superconductivity in different systems, and to ultimately get us closer to systemetizing the theoretical models of superconductors.

While the fortuitous findings of superconductors have been pivotal, the success and importance of calculated predictions should not be understated, as electronic structure tools such as density functional theory have been essential in directing us in the right directions. All of the theoretical work in this dissertation is based on density functional methods, which will be reviewed in Chapter 3. The preceding chapter will go over key concepts of superconductivity. A nonsuperconductor can suddenly become superconducting merely by changing the distance between its atoms via, e.g., application of pressure. High pressure experiments were conducted on one of the materials ($CaLi_2$) covered in this thesis; the methods are presented in Chapter 4.

The chapters thereafter detail the research performed on three compounds: NaAlSi, $CaLi_2$, and $PuPt_2In_7$. NaAlSi crystallizes into a tetragonal structure that is, aside from the iron-pnictide 111s, a a rare find within superconductors. In Chapter 5, we present results of our density functional-based calculations of 7 K superconductor NaAlSi. The band structure reveals NaAlSi to be an intrinsically doped semimetal, in which the Al atoms offer nearly free electron carriers and the covalent Al-Si system provides the holes. Isostructural NaAlGe, which is not superconducting above 1.6 K, is shown to have a nearly-identical band structure near the Fermi level, save for a missing piece of Fermi surface. Certain deformation potentials induced by Si and Na displacements along the c-axis are calculated and discussed. It may be that the mechanism of pairing is related to that of several other lightly doped two-dimensional nonmagnetic semiconductors (TiNCl, ZrNCl, HfNCl), which is not well understood but apparently not of phonon origin.

In Chapter 6, $CaLi_2$ is examined experimentally. It has been reported that $CaLi_2$ becomes superconducting above 10 GPa, but theoretical works of past disagree as to whether or not the compound breaks down at such pressures into its elemental constituents, so that Li may superconduct. X-ray diffraction measurements at low temperature and high pressure were carried out in order to obtain the structural phase diagram in the superconducting region and beyond.

It is as important to understand how materials superconduct, as it is to learn why other related materials don't. $PuPt_2In_7$, interesting for its structural and electronic relation to 18 K superconductor $PuCoGa_5$, is a mass-enhanced paramagnet and does not superconduct above 2 K. The absence of superconductivity is explored via the generalized gradient approximation in the density functional scheme, with the addition of orbital dependence. Hypothetical $PuPt_2Ga_7$ is calculated and discussed correspondingly.

Chapter 2

Superconductivity

2.1 Introduction

It has been 100 years since the discovery of superconductivity, and the field has grown to massive breadths. Many questions regarding superconductivity have since been answered, but the continual string of new discoveries has elicited new questions to tackle. Once thought to be an uncommon phenomenon, it has come to the realization of the scientific community that superconductivity is ubiquitous—exhibited in metals, magnets, ceramics, and organic materials. Fifty-two elements in the periodic table superconduct at ambient and/or higher pressure [4], and more are suspected to be superconducting, provided the ultra-low temperatures and/or ultra-high pressures. We now know there are different classes of superconductivity with different types of mechanisms, and the technicalities are still being debated highly. The picture is growing in complexity and much has yet to be understood.

Physicists and engineers have been trying to exploit the fact that superconductors pass high electrical currents with no energy loss. One prospect is using superconducting pipelines in electrical smart grids to greatly increase efficiency. The applicability is very much limited at the moment however, and one reason is that the energy to keep the superconducting material below the superconducting transition temperature outweighs the energy saved due to the lack of resistance. In search of higher-temperature superconductivity, a multitude of superconductors have been discovered. Some of these discoveries had been predicted, but oftentimes they were by chance. In order to improve on smart discoveries, rather than serendipitous ones, the physics of the mechanisms needs to be better understood.

2.2 History of Superconductivity

Superconductivity was first discovered in 1911, when Onnes found that, below a certain temperature, the electrical resistance of mercury dropped to zero [16]. Mercury has a superconducting transition temperature of $T_c = 4.2$ K. Three years prior, Onnes conveniently had liquefied helium for the first time [17]. By dipping mercury in liquid helium, Onnes was able to bring its temperature down low enough to observe the phenonmenon of superconductivity.

In 1933, Meissner and Oschenfeld demonstrated with tin and lead that, in a weakly applied magnetic field, superconductors expel nearly all magnetic flux from their interior [18]. This is called the Meissner effect. The external field induces electric currents on (and near) the surface of the superconductor, creating a magnetic field within the bulk that opposes the externally applied field. Hence, the bulk superconductor acts like a perfect diamagnetic atom [19]. The Meissner effect and zero-resistivity characteristic explained in the paragraph above are very much related, as it is imperative to have a resistanceless current in order to maintain flux exclusion.

Phenomenological theories subsequently emerged. The first was the London brothers' theory [20, 21], based on electromagnetism, which was able to explain the Meissner effect and quantify the depth of penetration of an external field into a superconductor (the penetration depth). Another is the Ginzburg-Landau theory [22], an extension of the London theory based on Landau's theory of second-order transitions, and it introduced a characteristic length called the coherence length, which is the minimum length over which the superconducting order parameter (see next section) varies considerably.

While these theories describe well the macroscopic properties, the information of microscopic effects is absent in them. But in 1957, Bardeen, Cooper, and Schrieffer [23] proposed the first complete microscopic understanding of superconductivity, now known as the BCS theory. BCS theory explains that in superconductors, the energy of the system is lowered by the existence of pairs of electrons, coined Cooper pairs, which are indirectly attracted to each other via lattice vibrations. Hence it is also known as phonon-mediated superconductivity. (Phonon-mediated superconductivity later became known as conventional superconductivity, after theories for other types of superconductivity came to light.) BCS theory achieved excellent agreement with experimental observations such as the Meissner effect and the isotope effect [24, 25], which was first observed in 1950. Bogoliubov and Valatin independently and simultaneously also explained superconductivity that was consistent with the BCS description. But instead of the variational approach taken by Bardeen *e*t al., Bogliubov [26] and Valatin [27] adopted the canonical method; required is the Bogliubov-Valatin transformation of the creation and destruction operators in order to diagonalize the hamiltonian. This is better suited for studying excited states, as the gap equation is defined for temperatures above absolute zero.

A major turning point in the history of superconductivity was the discovery of the 30 K superconductor La-Ba-Cu-O by Bednorz and Müeller [28] in 1986. La-Ba-Cu-O was the first ceramic material and first of many copper-oxide perovskites to superconduct, had the highest observed T_c at the time, and did not conform to the conventional theory of BCS. Many more cuprate superconductors subsequently have come to light, and they have the highest T_c's yet known (e.g., Y-Ba-Cu-O with a T_c of 93 K, and Bi-Sr-Ca-Cu-O , whose T_c is 105 K). Thus a new class of superconductivity was born, called high-temperature superconductivity.

La-Ba-Cu-O was not the first unconventional (high T_c) superconductor to have been found. It was $CeCu_2Si_2$, which Steglich *e*t al. discovered in 1979 [29]. They observed superconductivity below 1 K. Steglich and others demonstrated that magnetic correlations, not phonons, were responsible for superconductivity. Indeed, many materials exhibiting type-II superconductivity—characterized by the creation of vortices, through which magnetism penetrates—are also antiferromagnetic (AFM). $CeCu_2Si_2$ is also the first heavy fermion superconductor discovered. Superconductivity persists in numerous heavy fermion materials, despite the presence of strong local moments on the f electrons. Within the BCS framework this would prevent superconductivity. But in these systems, the moments fluctuate when interacting with the itinerant conduction electrons to form Cooper pairs [30].

Another breakthrough took place in 2001 when Nagamatsu *e*t al. [31] found MgB_2 to have a T_c of 39 K, the highest transition temperature of all non-copper-oxides to date (with the exception of some of the new iron-based superconductors). MgB_2 is a common material that can be synthesized in wire form, which makes it a promising candidate for applications. It is a phonon-mediated superconductor, but also type II. This and other intriguing properties of MgB_2, especially the existence of two superconducting gaps, generated a surge of interest in the material and had physicists revisiting fundamental questions.

Most recently, the iron-based superconductors have been garnering much attention. In 2008, superconductivity in doped LaOFeAs below 26 K was discovered [32], which led to a whole class of iron-based, layered superconductors, with a mechanism that is not phononic nor like that of the cuprates. There is strong experimental and theoretical evidence that spin fluctuations give rise to superconductivity in the iron pnictides, as they do in the cuprates and heavy fermion superconductors. But iron pnictides are not Mott insulators, nor do they possess strong local moments. On the contrary, the electrons are more delocalized in these iron-based systems. Many assert, supported by phase diagrams, that the superconducting state competes with a spin-density wave due to a Fermi surface instability.

The discoveries throughout history have provided us with indispensible knowledge of the physics underlying superconductivity, and in turn the knowledge is being used to unearth novel superconductors. More classes of materials and different kinds of mechanism are expected to be discovered, thereby contributing to the enrichment of the science of superconductivity.

2.3 BCS Superconductivity

2.3.1 BCS theory

The microscopic theory of Bardeen, Cooper, and Schrieffer [23] correctly predicts the macroscopic properties of superconductors (e.g., the gap equation as a function of T_c, the isotope effect, the discontinuity in the specific heat, etc.). Here we present the BCS pairing theory (variational method) as outlined by Schrieffer [33].

We start with the reduced hamiltonian of the interacting electron system in secondquantized form,

$$\hat{H} = \sum_{\mathbf{k}\sigma} \varepsilon_{\mathbf{k}} n_{\mathbf{k}\sigma} + \sum_{\mathbf{k}\mathbf{k}'} V_{\mathbf{k}'\mathbf{k}} b^{\dagger}_{\mathbf{k}'} b_{\mathbf{k}}, \tag{2.1}$$

where the matrix element $V_{\mathbf{k}\mathbf{k}'}$ of the attractive pairing potential is

$$V_{\mathbf{k}'\mathbf{k}} = V(\mathbf{k}' - \mathbf{k}) = \langle \mathbf{k}', -\mathbf{k}' | V | \mathbf{k}, -\mathbf{k} \rangle, \tag{2.2}$$

and the operators $n_{\mathbf{k}\sigma}$, $b^{\dagger}_{\mathbf{k}}$, and $b_{\mathbf{k}}$ can be written in terms of the single-particle creation and destruction operators $c^{\dagger}_{\mathbf{k}\sigma}$ and $c_{\mathbf{k}\sigma}$:

$$n_{\mathbf{k}\sigma} = c^{\dagger}_{\mathbf{k}\sigma} c_{\mathbf{k}\sigma}, \tag{2.3}$$

$$b^{\dagger}_{\mathbf{k}} = c^{\dagger}_{\mathbf{k}\uparrow} c^{\dagger}_{-\mathbf{k}\downarrow}, \tag{2.4}$$

$$b_{\mathbf{k}} = c_{-\mathbf{k}\downarrow} c_{\mathbf{k}\uparrow}, \tag{2.5}$$

where σ is the spin index that is either ↑ or ↓. Note that this reduced hamiltonian takes into account only zero-momentum ($\mathbf{q} = \mathbf{k}' - \mathbf{k} = 0$) pairs of opposite spin. The hamiltonian is rewritten as

$$\hat{H} = 2 \sum_{\mathbf{k}} \varepsilon_{\mathbf{k}} b^{\dagger}_{\mathbf{k}} b_{\mathbf{k}} + \sum_{\mathbf{k}\mathbf{k}'} V_{\mathbf{k}'\mathbf{k}} b^{\dagger}_{\mathbf{k}'} b_{\mathbf{k}}. \tag{2.6}$$

The form of the BCS ground-state wavefunction was influenced by the work of Lee, Low, and Pines [34] (who related a simple wavefunction for the polaron):

$$|\psi_0\rangle \propto \prod_{\mathbf{k}} e^{g_{\mathbf{k}} b^{\dagger}_{\mathbf{k}}} |0\rangle \simeq \prod_{\mathbf{k}} \left(1 + g_{\mathbf{k}} b^{\dagger}_{\mathbf{k}}\right) |0\rangle, \tag{2.7}$$

where $g_{\mathbf{k}}$ is a variational parameter and $|0\rangle$ is the vacuum state. With the proper normalization,

$$|\psi_0\rangle = \prod_{\mathbf{k}} \frac{1 + g_{\mathbf{k}} b^{\dagger}_{\mathbf{k}}}{\sqrt{1 + g^2_{\mathbf{k}}}} |0\rangle. \tag{2.8}$$

$g_{\mathbf{k}}$ can be chosen such that the mean number of particles is constrained:

$$\langle \psi_0 | \sum_{\mathbf{k}\sigma} n_{\mathbf{k}\sigma} | \psi_0 \rangle = N_0. \tag{2.9}$$

The Lagrange multiplier method is used to minimize the Lagrange function:

$$0 = \delta \langle \psi_0 | \hat{H} - \mu \sum_{\mathbf{k}\sigma} n_{\mathbf{k}\sigma} | \psi_0 \rangle \tag{2.10}$$

$$= \delta \left[\sum_{\mathbf{k}} 2(\varepsilon_{\mathbf{k}} - \mu) v^2_{\mathbf{k}} + \sum_{\mathbf{k}\mathbf{k}'} V_{\mathbf{k}'\mathbf{k}} u_{\mathbf{k}} v_{\mathbf{k}} u_{\mathbf{k}'} v_{\mathbf{k}'} \right], \tag{2.11}$$

where μ is the chemical potential and $u_{\mathbf{k}}$ and $v_{\mathbf{k}}$ are defined as

$$u_{\mathbf{k}} \equiv \frac{1}{\sqrt{1+g_{\mathbf{k}}^2}} \tag{2.12}$$

and

$$v_{\mathbf{k}} \equiv \frac{g_{\mathbf{k}}}{\sqrt{1+g_{\mathbf{k}}^2}}, \tag{2.13}$$

such that $u_{\mathbf{k}}^2 + v_{\mathbf{k}}^2 = 1$. Upon minimization, we get

$$u_{\mathbf{k}}^2 = \frac{1}{2}\left(1 + \frac{\varepsilon_{\mathbf{k}} - \mu}{E_{\mathbf{k}}}\right), \tag{2.14}$$

$$v_{\mathbf{k}}^2 = \frac{1}{2}\left(1 - \frac{\varepsilon_{\mathbf{k}} - \mu}{E_{\mathbf{k}}}\right), \tag{2.15}$$

and

$$u_{\mathbf{k}} v_{\mathbf{k}} = \frac{\Delta_{\mathbf{k}}}{2E_{\mathbf{k}}}, \tag{2.16}$$

where $\Delta_{\mathbf{k}}$ and $E_{\mathbf{k}}$, the order parameter (energy gap) and quasi-particle excitation energy, respectively, are defined by

$$\Delta_{\mathbf{k}} \equiv -\sum_{\mathbf{k}'} V_{\mathbf{k}'\mathbf{k}} u_{\mathbf{k}'} v_{\mathbf{k}'}, \tag{2.17}$$

$$E_{\mathbf{k}} \equiv \sqrt{(\varepsilon_{\mathbf{k}} - \mu)^2 + \Delta_{\mathbf{k}}^2}. \tag{2.18}$$

Substituting Eq. (2.16) into Eq. (2.17) gives the self-consistent condition

$$\Delta_{\mathbf{k}} = -\sum_{\mathbf{k}'} V_{\mathbf{k}'\mathbf{k}} \frac{\Delta_{\mathbf{k}'}}{2E_{\mathbf{k}}}. \tag{2.19}$$

A simple solution is achieved when the potential is approximated. An attractive potential of s-wave symmetry and with an energy cutoff of ω_c,

$$V_{\mathbf{k}'\mathbf{k}} = \begin{cases} -V_0 < 0 & \text{for } |\varepsilon_{\mathbf{k}} - \mu| < \omega_c \\ 0 & \text{otherwise,} \end{cases} \tag{2.20}$$

is used in the original BCS theory. In this case, the energy gap is just

$$\Delta_{\mathbf{k}} = \begin{cases} \Delta_0 & \text{for } |\varepsilon_{\mathbf{k}} - \mu| < \omega_c \\ 0 & \text{otherwise,} \end{cases} \tag{2.21}$$

where Δ_0 is a constant. To solve for Δ_0, we substitute $-V_0$ and Δ_0 in for their **k**-dependent counterparts in Eq. (2.19),

$$\Delta_0 = \sum_{\mathbf{k}} V_0 \frac{\Delta_0}{2E_{\mathbf{k}}}. \tag{2.22}$$

and divide both sides of the equation by Δ_0 and transform the summation into an integral (with the variable $\xi \equiv \varepsilon_{\mathbf{k}} - \mu$):

$$\begin{aligned} 1 &= \frac{V_0}{2} \sum_{\mathbf{k}} \frac{1}{\sqrt{(\varepsilon_{\mathbf{k}} - \mu)^2 + \Delta_0^2}} && (2.23) \\ &\longrightarrow \frac{N(0)V_0}{2} \int_{-\omega_c}^{\omega_c} \frac{d\xi}{\sqrt{\xi^2 + \Delta_0^2}} && (2.24) \\ &= N(0)V_0 \sinh^{-1} \frac{\omega_c}{\Delta_0}, && (2.25) \end{aligned}$$

where $N(0)$ is the density of states (DOS) at the Fermi energy. In the weak-coupling limit $N(0)V_0 << 1$,

$$\Delta_0 = \frac{\omega_c}{\sinh\left[N(0)V_0\right]^{-1}} \approx 2\omega_c e^{-1/N(0)V_0}. \tag{2.26}$$

The energy gap, which can be measured via tunneling spectroscopy, is the forbidden energy range between the ground-state and quasi-particle energies. The value of the gap is the critical energy below which Cooper pairs cannot be broken into two quasiparticles. When the analysis is generalized to finite temperatures, T_c can be determined by letting the gap go to zero, and we get

$$k_B T_c = 1.13\omega_c e^{-1/N(0)V_0}. \tag{2.27}$$

The relation $\Delta(0) = 1.76 k_B T_c$, which follows from (2.26) and (2.27), has been tested experimentally and turns out to be quite reasonable. $N(0)V_0 \equiv \lambda$ is referred to as the electron-phonon coupling (EPC) constant.

2.3.2 Superconductivity of MgB$_2$ and electron-phonon coupling

The discovery of $T_c = 39$ K in magnesium diboride [31] garnered instant and massive attention, and thanks to the tremendous amount of theoretical [35, 36] and experimental [37–39] work it attracted, the understanding of the mechanism behind the superconductivity in this binary intermetallic compound is now well established. MgB$_2$ is a prime example of a good phonon-driven superconductor, but some of its physical and electronic

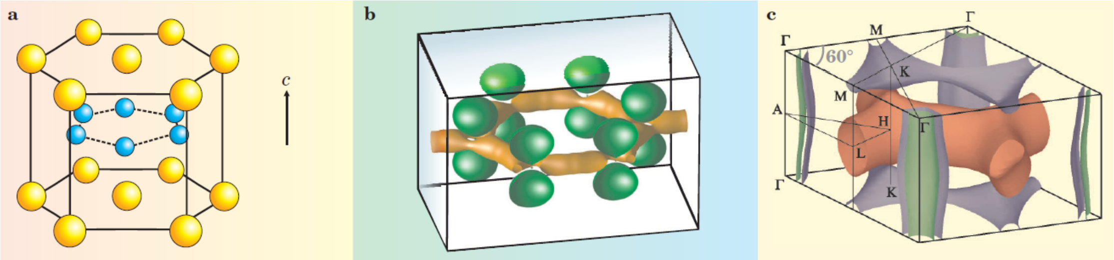

Figure 2.1. a) Crystal structure of MgB_2 (space group $P\ 6/mmm$, no. 191), where yellow (blue) atoms correspond to Mg (B). b) Constant charge density contour of σ (tan) and π (green) bonds. c) Fermi surface of MgB_2, where the 2D hole tubes are centered at Γ. Figures courtesy of Ref. 1

properties were quite different when compared to other BCS superconductors that had come before it. MgB_2 broke the once conventional theory that crystal systems of cubic symmetry are most favorable for BCS superconductivity. As shown in Fig. 2.1, MgB_2 instead possesses a two-dimensional hexagonal lattice, with layers of Mg sandwiched between layers of B. Yet it has the highest superconducting transition temperature of all BCS superconductors.

Its two-dimensionality is one reason why superconductivity in MgB_2 wasn't discovered sooner, despite its being a common laboratory substance since the 1950s. Another reason for the late revelation is its low DOS at the Fermi level, due to the lack of a transition metal (although the lighter atom and very strong bonding yield a higher Debye frequency). A larger DOS provides more carriers for pairing and thus better superconductivity, as is evident in Eq. (2.27).

It turns out that the layeredness of MgB_2's electronic structure allows for selective coupling between certain electronic states and phonons to thrive, resulting in a large V_0 in Eq. (2.27). Density functional theory calculations [35] show that the attractiveness of the Mg plane, due to the ionic nature between it and the B plane, pulls the p_z (π) bands down closer to the Fermi energy and leads to a $\sigma \to \pi$ transfer of electrons. Therefore, two-dimensional, covalently bonded σ (sp^2) states of B are self-doped with holes, which are enclosed in the cylindrical Fermi surfaces shown in c) of Fig. 2.1.

EPC in superconducting metals of weak to intermediate coupling strength, like MgB_2, can be obtained from Migdal-Eliashberg (ME) theory [40, 41]. In ME theory, the electron-phonon matrix element $g_{i\mathbf{k},j\mathbf{k}+\mathbf{q};\nu}$ represents the scattering of an electron in

Bloch state $|i\mathbf{k}\rangle$ to $|j\mathbf{k}+\mathbf{q}\rangle$ due to absorbing or emitting a phonon of reduced mass M, wave vector $\mathbf{q}$, and frequency $\omega_{\nu\mathbf{q}}$, and is written as [42]

$$g_{i\mathbf{k},j\mathbf{k}+\mathbf{q};\nu} = \frac{1}{\sqrt{2M\omega_{\nu\mathbf{q}}}}\langle i\mathbf{k}|\frac{\partial V}{\partial u_{\nu\mathbf{q}}}|j\mathbf{k}+\mathbf{q}\rangle, \tag{2.28}$$

where ν is the phonon branch index (each atom has three, corresponding to the three spatial directions), V is the crystal potential, and $u_{\nu\mathbf{q}}$ is the displacement of the phonon mode ν. The EPC constant λ can be decomposed into contributions $\lambda_{\nu\mathbf{q}}$ of each phonon mode and each phonon wave vector [42],

$$\lambda_{\nu\mathbf{q}} = \frac{2}{N_\sigma(0)\omega_{\nu\mathbf{q}}}\sum_{ij\mathbf{k}}|g_{i\mathbf{k},j\mathbf{k}+\mathbf{q};\nu}|^2\delta(\varepsilon_{i\mathbf{k}})\delta(\varepsilon_{j\mathbf{k}+\mathbf{q}}-\varepsilon_{i\mathbf{k}}-\omega_{\nu\mathbf{q}}), \tag{2.29}$$

where $N_\sigma(0)$ is the electronic DOS per spin at the Fermi energy. The form comes from its relation to the phonon linewidth $\gamma_{\nu\mathbf{q}}$, by

$$\lambda_{\nu\mathbf{q}} = \frac{1}{\pi N_\sigma(0)}\frac{\gamma_{\nu\mathbf{q}}}{\omega^2_{\nu\mathbf{q}}}. \tag{2.30}$$

The Eliashberg spectral function $\alpha^2F(\omega)$ is the spectral distribution of the total EPC:

$$\alpha^2F(\omega) = \frac{1}{2}\sum_{\nu\mathbf{q}}\omega_{\nu\mathbf{q}}\lambda_{\nu\mathbf{q}}\delta(\omega-\omega_{\nu\mathbf{q}}). \tag{2.31}$$

The total coupling λ is related to $\alpha^2F(\omega)$ by

$$\lambda = 2\int\frac{d\omega}{\omega}\alpha^2F(\omega). \tag{2.32}$$

Several groups applied ME theory to the electronic structure of MgB_2 derived from density functional theory calculations [43–46]. While the variation in their techniques gave rise to a range of EPC values ($\lambda = 0.73$–0.87), they all agreed that the large EPC in MgB_2 is attributed to the extremely strong coupling between the B σ state and the in-plane B-B stretch (E_{2g}) mode, and the coupling of the π state is considerably weaker. The anisotropy in the EPC explains the existence of, interestingly, two superconducting gaps in MgB_2, which explains the shoulder observed in the electronic specific heat curve below 10 K [47], and as evidenced by tunneling experiments [48].

Naturally, scientists began searching for novel MgB_2-type superconductors—i.e., *sp*, layered, metallic materials that are similar in structure and chemistry. Kuroiwa *et* al. discovered isostructural CaAlSi with a T_c of 8 K [49]. First principles calculations done by Rosner *e*t al.

showed that hole-doped LiBC, another compound with the MgB_2 structure, would have an even higher EPC than MgB_2 [50] (but synthesis has been unsuccessful). Boeri *e*t al.ś calculations on hole-doped diamond revealed it is also an MgB_2 type superconductor, albeit three-dimensional and with a lower T_c (4 K), with hole-doped σ bands coupling to zone-center, bond-stretching phonons [51].

2.4 Heavy Fermion Superconductivity

Superconductivity in heavy fermion materials is very different from conventional superconductivity. Heavy fermion metals are materials which contain atoms with a partially filled f shell, namely the lanthanides and actinides. At room temperature, in heavy fermion metals, the local moments of the f electrons weakly interact with the conduction electrons, and they can be described as a fermi gas. However, heavy fermion metals typically refer to those at lower temperatures, at which there is strong coupling between the f electron and conduction cloud (the so-called Kondo effect [52]); this is better represented by Landau's fermi liquid picture. Such interaction entails consequences to the magnetic, electronic, and thermodynamic properties of the material—e.g., AFM (often) or ferromagnetic (rarely) correlations, massive f-electron quasiparticles (that can be up to 1000 times heavier than a free electron), and a large specific heat.

When $CeCu_2Si_2$ was found to be superconducting in 1979 [29], the discovery was initially met with skepticism. The common notion at the time was that superconductivity and magnetism could not mutually exist, and cases of superconductivity being destroyed upon incorporation of magnetic impurities reaffirmed this. This is indeed true in BCS superconductors, as the spin moments would obstruct the formation of the attractive singlet pairs. As more heavy-fermion superconductors were discovered (UBe_{13} [53], UPt_3 [54], URu_2Si_2 [55], etc.), it became evident that magnetism doesn't play just an idle role in superconductivity. Oftentimes the superconducting transition lies at or close to a magnetic instability, implying that superconductivity in these systems are very much affected by the behavior of local moments.

Due to their small energy scale, heavy-fermion superconductors tend to have a lower T_c than their cuprate counterparts and conventional superconductors. It however makes

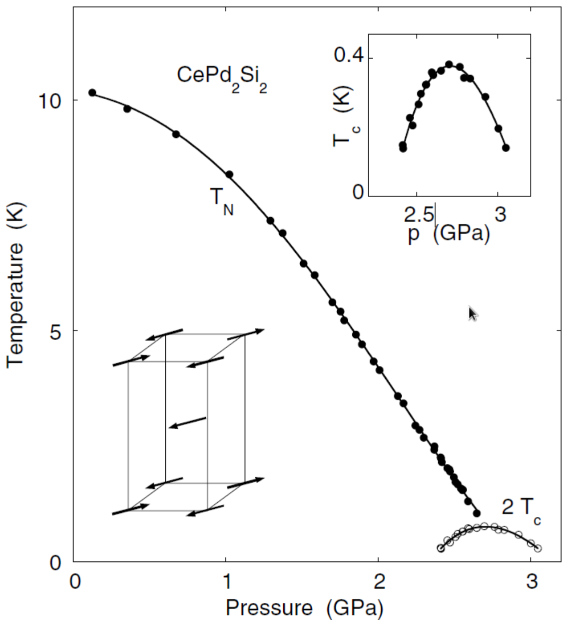

Figure 2.2. Temperature-pressure phase diagram of $CePd_2Si_2$ [2]. The AFM transition line meets with the superconducting dome at the maximum superconducting transition temperature.

tuning of their properties (by means of pressurization, chemical doping, or other) relatively easy. Looking at Fig. 2.2, the entire temperature-pressure phase diagram phase diagram of $CePd_2Si_2$ fits within 3 GPa and 10 K. In the figure, it can be seen that a magnetic quantum critical point (QCP) would lie at 2.9 GPa, if it weren't for superconductivity. The explanation is that a delicate balance between spin fluctuations and itinerant magnetism is required for superconductivity to take place. Some compounds, such as Ge-doped $CeCu_2Si_2$, exhibit two separate superconducting transitions, as shown in Fig. 2.3. The left-hand-side transition is at an AFM instability, not unlike that in Fig. 2.2. The other lies on the border of a volume collapse transition.

Although a microscopic theory for magnetically mediated superconductivity has not been fully established, it is now widely accepted that local-moment fluctuations are to heavy-fermion superconductivity as lattice vibrations are to BCS superconductivity. Monthoux *e*t al.

[3] have recently presented a phenomenological understanding that explains the spin-spin pairing in (both anti- and ferro-) magnetic or nearly magnetic superconductors mediated by magnetic fluctuations, as well as the secondary superconducting transition mediated

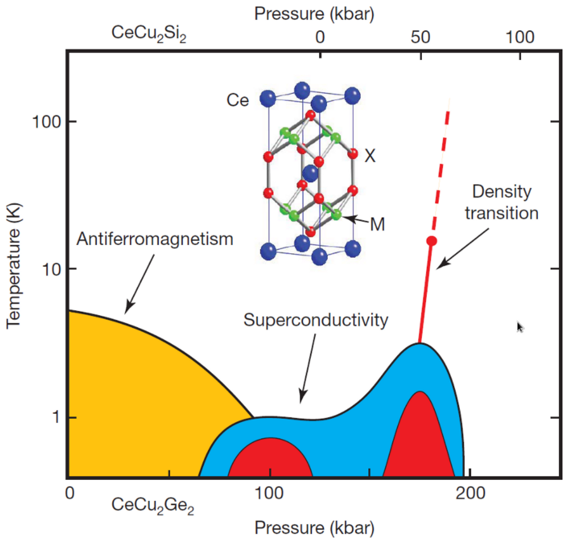

Figure 2.3. Temperature-pressure phase diagram of CeCu$_2$Si$_2$ and CeCu$_2$Ge$_2$, as well as Ge-doped CeCu$_2$Si$_2$ [3]. The superconducting region separates into two domes (in red) for the doped case; the two phases overlap for the two pure compounds (blue).

by density fluctuations.

The effort to find more heavy fermion superconductors has been accelerated shortly after the turn of the century, on account of the unearthing of superconductivity in PuCoGa$_5$ [56]. This revelation was notable not only in that its superconducting transition temperature ($T_c = 18.5$ K) is at least an order of a magnitude higher than any of the heavy fermion materials that have come before (and after) it, but it is the first Pu-compound superconductor to have been discovered. Our investigation into PuPt$_2$In$_7$ was elicited in part due to this exciting finding.

2.5 Superconductivity At High Pressure

Applying pressure on elements and compounds is a powerful way to better understand their intrinsic properties and to explore new territories. Pressure possesses the widest range of variation of all thermodynamic variables—from 10^{-35} Pa in outer space to 10^{35} Pa in the center of neutron stars—so studying the effects of pressure on a material helps to understand the material on a very broad level (so long as the pressures are attainable!), incomparable to what, e.g., temperature can achieve. Doping a material to reduce or increase the unit-cell size gives a similar effect; but by replacing an atom with

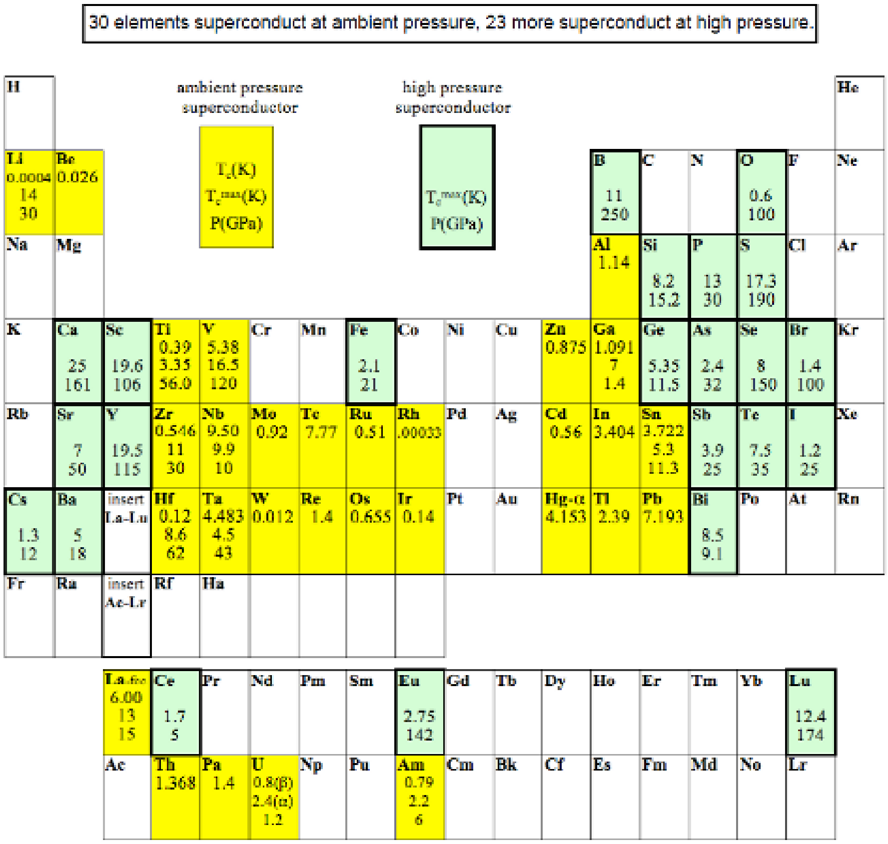

Figure 2.4. Period table, with information related to superconductivity, of elements [4]. Elements which superconduct at ambient pressure are filled in yellow, and those that superconduct at higher pressures have a bold frame.

a different one (or a void) the chemical composition is changed, thereby leaving much room for ambiguity when it comes to interpreting the results. Pressurization can be a more systematic method of research, as less variables need be taken into account.

High pressure physics is a growing field that brings to light interesting and peculiar phenomena. When enough pressure is applied to a material, the electronic structure may change drastically so that a new phase appears. For example, Yoo *et* al. [57] studied MnO at extreme pressures and observed a rich phase diagram: a paramagnetic (PM)-AFM transition, accompanied by a structural distortion, at 30 GPa; a magnetic transition back to PM, along with a structural transition, at 90 GPa; and a Mott insulator-to-metal transition, as well as a volume collapse, at 100 GPa.

Superconductivity is another phase of great interest that may arise upon compression of a material. The first pressure experiment performed on superconductors was in

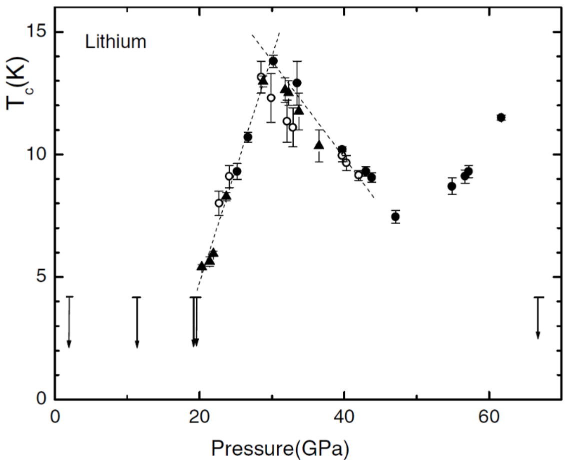

Figure 2.5. T_c-pressure phase diagram of Li under hydrostatic pressure [5].

1925 by Sizoo and Onnes [58], who took Sn and In to 0.03 GPa and observed in both materials a decrease in the superconducting transition temperature. As seen in Fig. 2.4, superconductivity actually turns out to be quite common amongst the elemental materials (there are 23), especially when superconductivity under pressure is included (a total of 52!). Sometimes the superconducting transition temperature goes down when pressure is applied (as is the case for Sn and In, and in accordance with fundamental BCS theory), but sometimes it goes up, which leaves scientists with a desire to understand why and has them searching for materials and pressures that could push T_c even higher. Li has a distinctive superconducting phase diagram under pressure, shown in Fig. 2.5. Li has a superconducting transition temperature of 4 mK at ambient pressure [59], but it jumps to 5.5 K at 20 GPa. After a steep rise to $T_c = 14$ K at 30 GPa, it descends and again goes up, after which superconductivity disappears at 62 GPa. The pressures at which dT_c/dP changes sign coincide with structural changes, supporting the idea that superconductivity in Li competes with the symmetry breaking due to structural transitions.

Light elements, such as Li and Ca (another superconductor at extreme pressures [60, 61]), and materials consisting of light elements are easier to squeeze than their heavier counterparts, and therefore have the potential to exhibit very different and exotic physical properties at extreme pressures. After the prediction by Feng *et* al. [62] of a superconducting phase for $CaLi_2$ at high pressure, followed by experimental evidence of bulk superconductivity in the sample [14], we were motivated to look at the compound theoretically and experimentally. Conflicting views as of late, on whether the observed superconducting phase is due to the compound CaLi_2 or the dissociated elemental Li [63, 64], have given us all the more reason to study the material.

Chapter 3

Density Functional Theory

3.1 Introduction

Electronic structure calculations provide us with means to describe the physical and chemical properties of matter. Our knowledge of electronic structure has come a long way since 1896, when Zeeman discovered the splitting of spectral lines by a strong magnetic field, and attributed this phenomenon, known as the Zeeman effect, to negatively charged particles with a very small mass: the electron [65]. With the advent of band theory and the increasing power of computers, quantitative calculations on electron systems, such as density functional theory (DFT), have become widespread in the modern era.

DFT is the most common electronic structure method of today. First developed by Hohenberg & Kohn [66] and Kohn & Sham [67], it is the successor to the many-electron method of Hartree-Fock [68], which, like DFT, determines the ground-state density and energy of a system in a self-consistent field. Hartree-Fock involves solving the 3N-dimensional Schrödinger equation, but DFT greatly simplifies in principle the problem by replacing this with a three-dimensional single-electron equation. The new problem that arises from this approach is that it requires a good approximation of the exchange-correlation functional (electron-electron correlations are not even taken into account in the Hartree-Fock scheme, only the exclusion principle). However, existing approximations, popular ones being the local density approximation and the generalized gradient approximation, are accurate enough to render DFT much more practical and efficient a method for electronic structure calculations than previous ones.

3.2 Born-Oppenheimer Approximation

DFT is based on the approximation that the nuclear mass is infinite when compared to the electronic mass, so that the nuclear and electronic degrees of freedom can be decoupled. It is called the Born-Oppenheimer (BO) approximation [69]. Within this approximation, there is no exchange of energy between the electrons and infinitely massive nuclei; hence it is also referred to as the adiabatic approximation. The BO approximation provides also the basis for electron-phonon coupling theory.

The formulation of the BO approximation, as laid out by Martin [70], exploits the fact that the nuclear kinetic energy is small and treats it as a perturbation. The hamiltonian for a system of nuclei and electrons is

$$\hat{H} = \hat{T}_N + \hat{T}_e + \hat{V} \tag{3.1}$$

$$= -\frac{1}{2}\sum_I \frac{1}{M_I}\nabla_I^2 - \frac{1}{2}\sum_i \nabla_i^2 + \hat{V}, \tag{3.2}$$

where $\hat{T}_N$ and $\hat{T}_e$ are the kinetic energy operators for the nuclei and electrons, respectively, M_I is the nucleus mass, and $\hat{V}$ is the operator for all potential energy terms. The eigenvalue E_s and wavefunction $\Psi_s(\{\mathbf{r},\mathbf{R}\})$ of the coupled system are dependent on the set of the coordinate parameters of all the nuclei, $\{\mathbf{R}\}$, and the index s denotes a particular state of the coupled system of $\{\mathbf{R}\}$ and the electrons' positions $\{\mathbf{r}\}$:

$$\hat{H}\Psi_s(\{\mathbf{r},\mathbf{R}\}) = E_s\Psi_s(\{\mathbf{r},\mathbf{R}\}). \tag{3.3}$$

$\Psi_s(\{\mathbf{r},\mathbf{R}\})$ can be written in terms of the electronic wavefunction $\Phi_i(\{\mathbf{r}\} : \{\mathbf{R}\})$,

$$\Psi_s(\{\mathbf{r},\mathbf{R}\}) = \sum_i \chi_{si}(\{\mathbf{R}\})\Phi_i(\{\mathbf{r}\} : \{\mathbf{R}\}), \tag{3.4}$$

where the coefficients $\chi_{si}(\{\mathbf{R}\})$ of wavefunctions $\Phi_i(\{\mathbf{r}\} : \{\mathbf{R}\})$ represent the electron-nuclear coupling. Multiplying $\Phi_i(\{\mathbf{r}\} : \{\mathbf{R}\})$ to the hamiltonian yields the electronic eigenvalue $E_i(\{\mathbf{R}\})$ of the adiabatic contribution:

$$\hat{H}\Phi_i(\{\mathbf{r}\} : \{\mathbf{R}\}) = (\hat{T}_e + \hat{V})\Phi_i(\{\mathbf{r}\} : \{\mathbf{R}\}) = E_i(\{\mathbf{R}\})\Phi_i(\{\mathbf{r}\} : \{\mathbf{R}\}), \tag{3.5}$$

where the nuclear positions $\{\mathbf{R}\}$ are fixed for the calculation. Plugging Eq. (3.4) into

Eq. (3.3) gives

$$\hat{H}\Psi_s(\{\mathbf{r},\mathbf{R}\}) = \hat{H}\sum_i \chi_{si}(\{\mathbf{R}\})\Phi_i(\{\mathbf{r}\}:\{\mathbf{R}\}), \tag{3.6}$$

$$= -\frac{1}{2}\sum_I \frac{1}{M_I}\nabla_I^2 \sum_i \chi_{si}\Phi_i + \sum_i \chi_{si}\hat{T}_e\Phi_i + \sum_i \chi_{si}\hat{V}\Phi_i, \tag{3.7}$$

$$= -\frac{1}{2}\sum_I \frac{1}{M_I}\nabla_I^2 \sum_i \chi_{si}\Phi_i + \sum_i E_i(\{\mathbf{R}\})\chi_{si}\Phi_i. \tag{3.8}$$

$$= E_s\hat{H}\sum_i \chi_{si}\Phi_i. \tag{3.9}$$

The first term on the right-hand side of (3.8) can be written as

$$-\frac{1}{2}\sum_{iI}\frac{1}{M_I}\nabla_I^2\chi_{si}\Phi_i = -\frac{1}{2}\sum_{iI}\frac{1}{M_I}\left[(\nabla^2\Phi_i)\chi_{si} + 2\boldsymbol{\nabla}\Phi_i\cdot\boldsymbol{\nabla}\chi_{si} + \Phi_i\nabla^2\chi_{si}\right] \tag{3.10}$$

$$= -\frac{1}{2}\sum_{iI}\frac{1}{M_I}\left[(\nabla^2\Phi_i)\chi_i + 2\boldsymbol{\nabla}\Phi_i\cdot\boldsymbol{\nabla}\chi_{si}\right] + \sum_i \Phi_i\hat{T}_N\chi_{si}. \tag{3.11}$$

Multiplying Eq. (3.3) by Φ_i^* after an $i \leftrightarrow i'$ index swap, and integrating over $\{\mathbf{r}\}$, leaves us with

$$\langle\Phi_i|\hat{H}|\Psi_s\rangle = \sum_{i'} C_{ii'}\chi_{si} + E_i(\{\mathbf{R}\})\chi_{si} = E_s\chi_{si}, \tag{3.12}$$

where the matrix elements $C_{ii'}$ are defined by

$$C_{ii'}(\{\mathbf{R}\}) \equiv -\sum_I \frac{1}{M_I}\left[\frac{1}{2}\langle\Phi_i|\nabla^2|\Phi_{i'}\rangle\chi_{si} + \langle\Phi_i|\boldsymbol{\nabla}|\Phi_{i'}\rangle\cdot\boldsymbol{\nabla}\chi_{si}\right]. \tag{3.13}$$

In the BO approximation the off-diagonal terms are set to zero, as adiabaticity allows no change in the electronic state. When electron-phonon interaction is being calculated, the off-diagonal terms are not ignored and represent an exchange between different electronic states.

3.3 Hohenberg-Kohn Theorems

The Hohenberg-Kohn theorems [66] set the foundation for DFT. The first theorem states that the ground-state density of a system of interacting particles in an external potential uniquely determines that external potential. As a corollary, so long as we know the density of the ground state, we can completely determine all of the system's properties. To prove this, it has to be shown first that two potentials that differ by more than a trivial constant will give two different ground states. Let the two external potentials be

$\hat{V}_{\text{ext}}$ and $\hat{V}'_{\text{ext}}$. The Schrödinger equations for their respective ground-state wavefunctions, Ψ_0 and Ψ'_0, are

$$\hat{H}\Psi_0 = (\hat{T} + \hat{V} + \hat{V}_{\text{ext}})\Psi_0 = E_0\Psi_0, \tag{3.14}$$

$$\hat{H}'\Psi'_0 = (\hat{T} + \hat{V} + \hat{V}'_{\text{ext}})\Psi'_0 = E'_0\Psi'_0, \tag{3.15}$$

where $\hat{H}$ is the Hamiltonian, $\hat{T}$ is the kinetic energy, $\hat{V}$ is the Hartree term, and E is the ground-state energy. The proof is carried out by *reductio ad absurdum.* Let us assume $\Psi_0 = \Psi'_0$. Subtracting (3.15) from (3.14),

$$(\hat{V}_{\text{ext}} - \hat{V}'_{\text{ext}})\Psi_0 = (E - E')\Psi_0. \tag{3.16}$$

The equation above tells us that the potentials differ by no more than a constant, as $E - E'$ is just that. This is in contradiction with the original supposition. Hence, no two different potentials can lead to the same ground state.

Next, we have to prove that no two different potentials can lead to the same ground-state *density.* In the nondegenerate case, we have the following inequality per the variational principle and proof asserting $\Psi_0 \neq \Psi'_0$:

$$E_0 = \langle\Psi_0|\hat{H}|\Psi_0\rangle < \langle\Psi'_0|\hat{H}|\Psi'_0\rangle. \tag{3.17}$$

The last term above can be written as

$$\langle\Psi'_0|\hat{H}|\Psi'_0\rangle = \langle\Psi'_0|\hat{H}'|\Psi'_0\rangle + \langle\Psi'_0|\hat{H} - \hat{H}'|\Psi'_0\rangle \tag{3.18}$$

$$= E'_0 + \int n'(\mathbf{r})[V_{\text{ext}}(\mathbf{r}) - V'_{\text{ext}}(\mathbf{r})]d^3r, \tag{3.19}$$

where $n'_0(\mathbf{r})$ is the ground-state density of the primed system. We rewrite the inequality as

$$E_0 < E'_0 + \int n'(\mathbf{r})[V_{\text{ext}}(\mathbf{r}) - V'_{\text{ext}}(\mathbf{r})]d^3r. \tag{3.20}$$

The primed and unprimed terms can be interchanged, so we also have

$$E'_0 < E_0 + \int n(\mathbf{r})[V'_{\text{ext}}(\mathbf{r}) - V_{\text{ext}}(\mathbf{r})]d^3r. \tag{3.21}$$

We again prove by contradiction. Suppose the unprimed system and primed system have identical ground-state densities: $n(\mathbf{r}) = n'(\mathbf{r})$. Adding the two inequalities above,

$$E_0 + E'_0 < E'_0 + E_0, \tag{3.22}$$

which is incorrect. We can conclude that if two potentials differ by more than a constant, their ground-state electronic densities are necessarily different. In other words, V_{ext} is a unique *functional* of $n(\mathbf{r})$. This is the first of two Hohenberg-Kohn theorems, and it can be generalized to apply to degenerate ground states.

Since all properties are functionals of the ground-state density, so are the kinetic and interaction energies. The second Hohenberg-Kohn theorem asserts that there exists a functional for the energy, $E[n(\mathbf{r})]$, that is a unique functional of the density, and a universal functional that is independent of the external potential; and the true ground-state density is one which minimizes the energy functional. $E[n]$ is defined as

$$E[n(\mathbf{r})] \equiv \langle \Psi[n] | \hat{H} | \Psi[n] \rangle = T[n] + V[n] + \int n(\mathbf{r}) V_{\text{ext}}(\mathbf{r}) d\mathbf{r}. \tag{3.23}$$

As a consequence of the first theorem, a unique ground-state density $n(\mathbf{r})$ is determined for an external potential $V_{\text{ext}}(\mathbf{r})$, and the energy takes on the value $E[n(\mathbf{r})] = E_0$. Let there be a different density $n'(\mathbf{r})$ necessarily corresponding to different a wavefunction Ψ'. By the Rayleigh-Ritz principle, the energy E_0' corresponding to $n'(\mathbf{r})$ is

$$E_0' = \langle \Psi' | \hat{H} | \Psi' \rangle > \langle \Psi | \hat{H} | \Psi \rangle = E_0. \tag{3.24}$$

This proves the second Hohenberg-Kohn theorem. As a corollary, the ground-state density and energy can be found by varying the density to minimize the energy, so long as we know the form of the energy functional. While in practice an approximate form of the energy functional is used, DFT is in principle an exact theory—i.e., minimizing the exact energy functional leads to the exact ground-state density.

3.4 The Self-Consistent Kohn-Sham Equations

Kohn and Sham [67] proposed a way in which the Hohenberg-Kohn theorems can be applied to establish a computationally feasible problem. The Kohn-Sham (KS) approach replaces the interacting many-body system with a fictitious non-interacting single-particle system, but that which is in an effective potential v_{eff} that produces the same ground-state density as the original. This, as we shall see, allows for the use of density as the basic variable to solve the hamiltonian, a method which was already proven in principle to work by Hohenberg and Kohn. The hamiltonian of the auxiliary KS system is made up of kinetic and effective potential terms,

$$\hat{H}_{\text{KS}}\psi_i(\mathbf{r}) = \left[-\frac{1}{2}\nabla^2 + v_{\text{eff}}(\mathbf{r})\right]\psi_i(\mathbf{r}) = \varepsilon_i, \tag{3.25}$$

where the index i labels both spin and orbital quantum numbers, and ε_i are the eigenvalues. The density is derived from the occupied wavefunctions $\psi_i(\mathbf{r})$ of the individual non-interacting states (so called Kohn-Sham orbitals),

$$n(\mathbf{r}) = \sum_i^{\text{occ}} |\psi_i(\mathbf{r})|^2, \tag{3.26}$$

and it is subject to the constraint of the total number of electrons,

$$N = \int n(\mathbf{r}) d\mathbf{r}. \tag{3.27}$$

The functional to be minimized is

$$E[n] - \mu N[n] = 0, \tag{3.28}$$

where μ, the chemical potential, is the Lagrange multiplier. The unique KS energy functional is

$$E_{\text{KS}}[n] = T_s[n] + \int n(\mathbf{r}) v_{\text{eff}}(\mathbf{r}) d\mathbf{r}, \tag{3.29}$$

where $T_s[n]$ is the kinetic energy of the non-interacting system. Let us rewrite the energy functional of the real, interacting system from Eq. (3.23),

$$\begin{aligned} E[n] =& T[n] + V[n] + \int n(\mathbf{r}) v_{\text{ext}}(\mathbf{r}) d\mathbf{r} \\ =& T_s[n] + \frac{1}{2}\int \frac{n(\mathbf{r})n(\mathbf{r}')}{|\mathbf{r}-\mathbf{r}'|} d\mathbf{r}d\mathbf{r}' + \int n(\mathbf{r}) v_{\text{ext}}(\mathbf{r}) d\mathbf{r} \\ &+ \left\{ T[n] - T_s[n] + V[n] - \frac{1}{2}\int \frac{n(\mathbf{r})n(\mathbf{r}')}{|\mathbf{r}-\mathbf{r}'|} d\mathbf{r}d\mathbf{r}' \right\}, \end{aligned} \tag{3.30}$$

where we have added and subtracted the kinetic energy and Hartree energy of the non-interacting body. The terms inside the braces make up the many-body exchange-correlation (XC) energy functional,

$$E_{\text{xc}}[n] \equiv T[n] - T_s[n] + V[n] - \frac{1}{2}\int \frac{n(\mathbf{r})n(\mathbf{r}')}{|\mathbf{r}-\mathbf{r}'|} d\mathbf{r}d\mathbf{r}'. \tag{3.31}$$

Taking the functional derivative,

$$\frac{\delta E[n]}{\delta n(\mathbf{r})} - \mu = \frac{\delta T_s[n]}{\delta n(\mathbf{r})} + 2\cdot\frac{1}{2}\int \frac{n(\mathbf{r}')}{|\mathbf{r}-\mathbf{r}'|} d\mathbf{r}' + v_{\text{ext}}(\mathbf{r}) + \frac{\delta E_{\text{xc}}[n]}{\delta n(\mathbf{r})} = 0, \tag{3.32}$$

and similarly,

$$\frac{\delta E_{\mathrm{KS}}[n]}{\delta n(\mathbf{r})} - \mu = \frac{\delta T_s[n]}{\delta n(\mathbf{r})} + v_{\mathrm{eff}}(\mathbf{r}) = 0. \tag{3.33}$$

The form of the effective potential of the fictitious non-interacting system that leads to the same density can be seen from the last two equations,

$$v_{\mathrm{eff}}(\mathbf{r}) = \int \frac{n(\mathbf{r}')}{|\mathbf{r}-\mathbf{r}'|} d\mathbf{r}' + v_{\mathrm{ext}}(\mathbf{r}) + v_{\mathrm{xc}}[n(\mathbf{r})], \tag{3.34}$$

where the last term is the XC potential

$$v_{\mathrm{xc}}(\mathbf{r}) \equiv \frac{\delta E_{\mathrm{xc}}}{\delta n(\mathbf{r})}. \tag{3.35}$$

With an unknown density and effective potential, the KS scheme is a self-consistent scheme. In practice, an initial, approximate form of $n(\mathbf{r})$ is guessed and plugged into Eq. (3.34) to get v_{eff}, which is then inserted into Eq. (3.25) to solve for the KS orbitals ψ_i. The orbitals are used in (3.26) to obtain the new density, which is ready for the next iteration. When the densities of two consecutive iterations are sufficiently close, the true ground-state density of the system has been found. These three equations are called the Kohn-Sham equations.

The KS method is built on the ansatz that there exists a system of non-interacting electrons, whose ground-state density is exactly equal to that of a system of interacting electrons. Though a rigorous proof has not been found, there hasn't been any evidence disproving the ansatz, and it has been validated for simple systems.

Note that the KS orbitals ψ_i and energies ε_i do not translate to anything physical; they must not be mistaken for excited states and energies. The only connections they have to the real system are the direct relation between ψ_i and the density $n(\mathbf{r})$, and that the highest occupied energy ε_{N} is equal to the real system's exact ionization energy [71].

3.5 The Exchange-Correlation Energy Functional

Opting for simplicity comes at a cost to accuracy, in that the exchange-correlation energy functional contains many-body terms whose exact forms are generally unknown. The two most popular approximations to the XC functional, the local density approximation (LDA) and the generalized gradient approximation (GGA), are fortunately quite accurate for many types of systems, such as insulators and wide-band metals. They are not suitable for strongly correlated systems, such as copper oxides and heavy fermion materials, and corrections for such cases will be discussed.

3.5.1 Local (spin) density approximation

Many solids can closely resemble an interacting homogeneous electron gas (HEG) model (or jellium model, and the local density approximation exploits this connection: while there is variation in the density, in the local regime, the density is approximated as constant. Hence it is more accurate for a system of a slowly varying density. The LDA XC functional is

$$E_{\mathrm{xc}}^{\mathrm{LDA}}[n(\mathrm{r})] = \int n(\mathrm{r})\epsilon_{\mathrm{xc}}(n(\mathbf{r}))d\mathbf{r}, \tag{3.36}$$

where $\epsilon_{\mathrm{xc}}(n(\mathbf{r})) = \epsilon_{\mathrm{x}}(n(\mathbf{r}))+\epsilon_{\mathrm{c}}(n(\mathbf{r}))$, the XC energy per particle of a uniform interacting gas of density $n(\mathbf{r})$, is not a functional but an ordinary function, and at r it is dependent on the density only in some neighborhood of r. The local density *spin* approximation (LSDA, often called “LDA” as well) is a generalized form of the LDA that takes into account electron spin, which is crucial for spin-polarized cases. In LSDA, the functional will be dependent on both the up- and down-spin densities,

$$E_{\mathrm{xc}}^{\mathrm{LSDA}}[n_{\uparrow}(\mathbf{r}), n_{\downarrow}(\mathbf{r})] = \int n(\mathrm{r})\epsilon_{\mathrm{xc}}(n_{\uparrow}(\mathbf{r}), n_{\downarrow}(\mathbf{r}))d\mathbf{r}. \tag{3.37}$$

Using the simpler no-spin LDA form, the XC potential, from (3.35), is

$$v_{\mathrm{xc}}(\mathbf{r}) = \epsilon_{\mathrm{xc}}(n(\mathbf{r})) + n(\mathbf{r})\frac{\delta\epsilon_{\mathrm{xc}}(n(\mathbf{r}))}{\delta n(\mathbf{r})}. \tag{3.38}$$

The LDA exchange energy $E_{\mathrm{x}}^{\mathrm{LDA}}$ is analytical and the same as that of the HEG, evaluated in the separate works of Bloch [72] and Dirac [73], then later of Slater [74] to simplify the Hartree-Fock method. The Hartree-Fock exchange energy per particle of the HEG is determined as

$$E_{\mathrm{x}}^{\mathrm{LDA}}[n(\mathrm{r})] = \frac{3}{4}\left(\frac{3}{\pi}\right)^{1/3} n(\mathrm{r})^{1/3}. \tag{3.39}$$

The correlation energy $E_{\mathrm{c}}^{\mathrm{LDA}}$, except for in the high- and low-density limits, is not known analytically, and therefore has to be approximated. The Green’s function quantum Monte Carlo method gives highly accurate expressions for intermediate densities. The most well-known and well-used correlation energy functionals are interpolations based on the Monte Carlo data of Cerperley and Alder [75], and they are the Vosko-Wilk-Nusair [76], Perdew-Zunger [77], Cole-Perdew [78], and Perdew-Wang [79] functionals.

Even for systems described by a rapidly varying density, the LDA is surprisingly in good agreement with experimental measurements. As mentioned before, however, the LDA does not work well for materials with strong local moments. It is also inaccurate for simpler systems, as van der Waals forces are not accounted for, and hydrogen bonding is overestimated in the LDA.

3.5.2 Generalized gradient approximation

The generalized gradient approximation is considered a "semi-local" approximation, in which the XC energy is a functional not only of the density but of the gradient of the density $\nabla n(\mathrm{r})$ as well:

$$E_{\mathrm{xc}}^{\mathrm{GGA}}[n_{\uparrow}(\mathbf{r}), n_{\downarrow}(\mathbf{r})] = \int f_{\mathrm{xc}}(n_{\uparrow}(\mathbf{r}), n_{\downarrow}(\mathbf{r}), |\nabla n_{\uparrow}|, |\nabla n_{\downarrow}|) d\mathbf{r}. \tag{3.40}$$

A similar, earlier approach, called the gradient expansion approximation, was introduced in the original Hohenberg-Kohn paper [66], but the second-order gradient expansion for the Fourier-transformed exchange-correlation hole potential diverges for small wave vectors and thus violates the sum rule, making it at times even less accurate than the LDA. This problem is remedied in the GGA by cutting off the spurious terms to satisfy the sum rule. This and other corrections to the gradient expansion approximation were first presented by Langreth & Mehl [80] and Langreth & Perdew [81]. A real-space cutoff method was later implemented by Perdew and Wang [82].

The analytic parameterized function f_{xc} in Eq. (3.40) comes in many forms, of which the Becke [83], Perdew-Wang [84] (not to be confused with the LDA of Perdew and Wang [79]), and Perdew-Burke-Ernzerhof [85] versions are most common. The GGA results in more accurate binding energies, atomic energies, and bond lengths when compared to the LDA, but is worse in other cases. The GGA does not improve much on the LDA for strongly correlated systems.

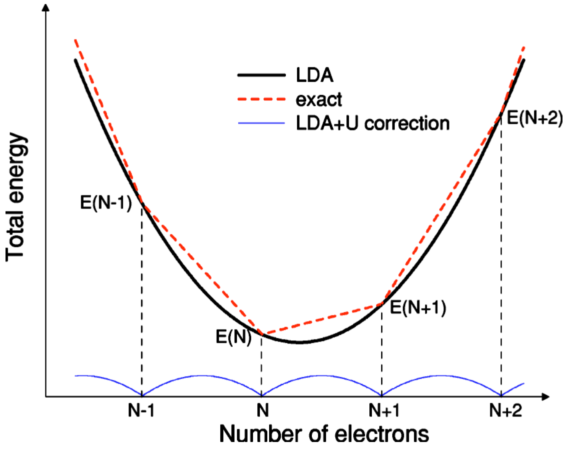

Figure 3.1. Generic sketch [6] of total energy as a function of number of electrons from an LDA calculation, and the exact version. LDA+U attempts to correct the difference.

3.5.3 The LDA+U method

That DFT is inadequate to represent localized states of d and f orbitals is its key failure. The LDA+U method [86] was first formulated to compensate for this flaw when treating transition metal oxides (TMOs). In TMOs, the d orbitals constitute the outermost shell. The electrons of the extended and partially filled d orbitals interact strongly with each other, so they feel a stronger effective Coulomb repulsion than the other electrons in the system. The charge hopping needed for electronic conduction is thus suppressed, rendering TMOs insulating rather than metallic.

While the deficiency to properly describe these systems stems not from DFT per se but the more fundamental formalism of band theory, DFT plays an additional and direct role in the band-gap problem through the XC term. The total energy as a function of the total number of electrons $N = M + \omega$, where M is a non-negative integer and $0 < \omega < 1$, is written as [87]

$$E(N) = (1 - \omega)E_M + \omega E_{M+1}, \tag{3.41}$$

which, due to the XC energy, has a discontinuous derivative at integer values of N [87] (see Fig. 3.1). The XC energy used in the LDA however does not. Godby et al. [88] pointed out the significance of the discontinuity, showing its absence leads to the underestimation of the band gap, as seen in many insulators and semiconductors.

First proposed by Anisimov et al. in 1991 [86], the LDA+U scheme incorporates in

DFT an extra step of adding an on-site Hubbard U on the d (or f) electrons.[1] The additional term essentially drives the system to prefer integer orbital occupancy. The total energy of the localized states in LDA+U is not only a functional of the electron densities $\rho_\sigma(\mathrm{r})$ but also the orbital occupation numbers $n_{\sigma,mm'}$ [89],

$$E[\rho_\uparrow(\mathrm{r}),\rho_\downarrow(\mathrm{r}),\{n_{\sigma,mm'}\}] = E^{\mathrm{LSDA}}[\rho_\uparrow(\mathrm{r}),\rho_\downarrow(\mathrm{r})] + E_U[\{n_{\sigma,mm'}\}] - E_{\mathrm{dc}}[\{n_\sigma\}] \tag{3.42}$$

(to avoid confusion with the density matrix element $n_{\sigma,mm'}$, where m denotes the magnetic quantum number and $n_\sigma = \mathrm{Tr}(n_{\sigma,mm'})$, the previous notation in this document for the total spin-σ charge density, "$n_\sigma(\mathrm{r})$", has been replaced with "$\rho_\sigma(\mathrm{r})$"). E^{LSDA} is the energy from the standard LSDA and E_U is the additional Hubbard-U contribution. E_{dc} is an important and necessary term, for it cancels out correlations effects that are double counted, in E^{LSDA} and in E_U.

In the original work of Anisimov, Zaanen, and Andersen [86], the functional (3.42) was dependent on the choice of coordinate system, making it theoretically troubling. The rotationally invariant form that is widely used today, by Liechtenstein, Anisimov, and Zaanen, came out four years later [90]. The rotationally invariant Hubbard energy is

$$\begin{aligned} E_U[\{n_{\sigma,mm'}\}] = \frac{1}{2}\sum_{\sigma,\{m\}} & [\langle\, m,m''|V_{ee}|m',m'''\rangle n_{\sigma,mm'} n_{-\sigma,m''m'''} \\ & + \left(\langle m,m''|V_{ee}|m',m'''\rangle - \langle m,m''|V_{ee}|m''',m'\rangle\right) n_{\sigma,mm'} n_{\sigma,m''m'''}\big] , \end{aligned} \tag{3.43}$$

where $\langle m,m''|V_{ee}|m',m'''\rangle$ are the matrix elements of the onsite electron-electron interaction and can be expressed in terms of complex spherical harmonics Y_{kq} and effective Slater integrals F^k,

$$\langle m,m''|V_{ee}|m',m'''\rangle = \sum_k a_k(m,m',m'',m''')F^k, \tag{3.44}$$

$$a_k(m,m',m'',m''') = \frac{4\pi}{2k+1}\sum_{q=-k}^{k} \langle lm|Y_{kq}|lm'\rangle \cdot \langle lm''|Y^*_{kq}|lm'''\rangle, \tag{3.45}$$

where l denotes the orbital quantum number and $0 \leq k \leq 2l$. The Gaunt coefficients a_k represent the angular contribution, as the Slater integrals represent the radial. The

---

[1] "LDA+U" is often used as a general term that includes LSDA+U and GGA+U as well, and will be used in such context throughout the thesis unless specified otherwise.

Slater integrals need to be determined (F^0, F^2, and F^4 for d electrons, an additional F^6 for f electrons) by the parameters U and J:

$$\begin{aligned} U =& \frac{1}{(2l+1)^2}\sum_{mm'}\langle m, m'|V_{ee}|m, m'\rangle = F^0, & (3.46)\\ J =& U - \frac{1}{2l(2l+1)}\sum_{mm'}[\langle m, m'|V_{ee}|m, m'\rangle - \langle m, m'|V_{ee}|m', m\rangle] & (3.47)\\ =& \frac{1}{2l(2l+1)}\sum_{m\neq m'}\langle m, m'|V_{ee}|m', m\rangle & (3.48)\\ =& \begin{cases} \frac{1}{14}(F^2+F^4) \text{ for } d \text{ electrons} \\ \frac{1}{6435}(286F^2+195F^4+250F^6) \text{ for } f \text{ electrons.} \end{cases} & (3.49) \end{aligned}$$

Knowledge of ratios of the F^k's are needed as well. For d orbitals,

$$\frac{F^4}{F^2} = \frac{5}{8}, \tag{3.50}$$

and for f orbitals,

$$\frac{F^2}{F^4} = \frac{675}{451}, \tag{3.51}$$

$$\frac{F^2}{F^6} = \frac{2025}{1001}. \tag{3.52}$$

When it comes to the double-counting term, there are two functionals that are popular. The fully-localized-limit (FLL), or atomic-limit, functional was formulated by Czyżyk et al. [91] and is written as

$$E_{\text{dc}}^{\text{FLL}}[\{n_\sigma\}] = \frac{1}{2}Un(n-1) - \frac{1}{2}J[n_\uparrow(n_\uparrow - 1) + n_\downarrow(n_\downarrow - 1)], \tag{3.53}$$

where U and J are the Coulomb and exchange parameters, and $n = n_\uparrow + n_\downarrow$. The other common double-counting correction is what is now referred to as the around-mean-field (AMF) functional. Its form is derived from the original fluctuation form of Anisimov's LDA+U functional [86], but with spin-splitting effects taken into account. Often the AMF double-counting term is used in conjunction not with the fluctuation-based E_U [86, 91], but with the basis set-independent form [90] (e.g., in WIEN2K [92, 93] and FPLO [94]). The AMF functional is

$$E_{\text{dc}}^{\text{AMF}}[\{n_\sigma\}] = \frac{1}{2}Un^2 - \frac{U+2lJ}{2(2l+1)}\sum_\sigma n_\sigma^2. \tag{3.54}$$

The AMF scheme has a tendency to suppress magnetic moments, favoring nonmagnetic solutions [95]. In general, FLL is better suited for systems possessing stronger correlations, while AMF is used for weaker interactions.

3.5.4 Basis sets

Before DFT can be applied, a basis set for the Kohn-Sham orbitals (the ψ_i in Eq. (3.26)) has to be chosen. The eigenstate expansion would be exact if the basis set were complete. Naturally the accuracy of the calculation is dependent on the size of the basis set. More basis functions however also means a higher computational cost, and the type of basis set also affects accuracy. It is important to balance accuracy and efficiency by choosing a good basis set and size. The vast majority of the computational research presented in this disseration is done in WIEN2K [92, 93], which utilizes linearized augmented plane waves (LAPWs), and FPLO (Full Potential Local Orbital) [94], which uses local orbitals.

The APW and LAPW methods

The LAPW method [96, 97] is an improvement from the augmented plane-wave (APW) method presented by Slater in 1937 [98]. It adopts the muffin-tin (MT) approximation, which was introduced by Slater at the same time and serves as the foundation for other augmented methods, such as the Korringa-Kohn-Rostocker [99, 100] and muffin-tin orbital [101] methods. In the MT approximation, the space in which the electrons and ions reside is separated into two distinct regions, based on how the potential is expanded. The MT spheres of some desired radius r_{MT} are centered at the atomic sites, and the rest of the space is called the interstitial region. In the APW scheme, the interstitial space is treated with a simple plane-wave expansion, but within the MT spheres the plane waves are augmented by a linear combination of atomic-like functions, so as to properly represent the complex nodal structure of the wavefunctions near the nucleus. The APW basis function is written as

$$\phi^{\mathrm{APW}}_{\mathbf{k}+\mathbf{G}}(\mathbf{r},E) = \begin{cases} \sum_{lm} A_{lm,\mathbf{k}+\mathbf{G}} u_l(r,E) Y_{lm}(\hat{\mathbf{r}}), & r < r_{\mathrm{MT}} \\ \frac{1}{\sqrt{\Omega}} e^{i(\mathbf{k}+\mathbf{G})\cdot\mathbf{r}}, & r > r_{\mathrm{MT}}. \end{cases} \tag{3.55}$$

The $u_l(r,E)$ are the radial solutions to the Schrödinger equation and the $Y_{lm}(\hat{\mathbf{r}})$ are spherical harmonics. $\mathbf{G}$ denotes the reciprocal lattice vectors and Ω is the volume of the unit cell. In practice, the summation over the orbital number l is finite and cut at a value $l_{\max}$ of choice. The coefficients $A_{lm,\mathbf{k}+\mathbf{G}}$ and the energy E are parameters that are to be determined. The $A_{lm,\mathbf{k}+\mathbf{G}}$ are found by matching each plane wave with its augmented counterpart at the sphere boundary $r = r_{\mathrm{MT}}$, to ensure continuity. E is to equal the eigenvalue ϵ_k of the Kohn-Sham hamiltonian at each k and band (and spin if relevant), so it has to be solved self-consistently. The coefficients to the basis functions to construct the KS orbital (the band index i is omitted),

$$\psi_{\mathbf{k}} = \sum_{\mathbf{G}} c_{\mathbf{G}} \phi_{\mathbf{k}+\mathbf{G}}, \tag{3.56}$$

are determined via the Rayleigh-Ritz variational principle, and $\psi = \sum_{\mathbf{k}} \psi_{\mathbf{k}}$ is equivalent to the ψ_i in Eq. (3.26) used to obtain the electronic density.

A shortcoming of the APW method is that the secular equation is energy-dependent. As a consequence, there exists a secular equation for each k point of each band that need be solved. This slows down the calculation immensely. Another problem is the asymptote problem: a singularity arises in $A_{lm,\mathbf{k}+\mathbf{G}}$ when $u_l(r_{\mathrm{MT}}, E) = 0$. This is particularly problematic for d- and f-orbital systems.

These issues were ameliorated by the linearization of the APWs. First suggested in 1967 by Marcus [102] and formulated in 1975 by Andersen [97] and Koelling & Arbman [96], the LAPW method added a term, the energy derivative of the radial function, to the augmented portion of the basis function,

$$\phi^{\mathrm{LAPW}}_{\mathbf{k}+\mathbf{G}}(\mathbf{r}) = \sum_{lm} \left[A_{lm,\mathbf{k}+\mathbf{G}} u_l(r, E_l) + B_{lm,\mathbf{k}+\mathbf{G}} \dot{u}_l(r, E_l) \right] Y_{lm}(\hat{\mathbf{r}}) \tag{3.57}$$

(the plane-wave construction outside the sphere remains unchanged). The added term is merely the second term of the Taylor expansion of $u_l(E_l)$ about the guessed value of E_l. Two sets of coefficients, $A_{lm,\mathbf{k}+\mathbf{G}}$ and $B_{lm,\mathbf{k}+\mathbf{G}}$, now have to be solved, by matching the basis functions at the boundary not just in value but also in slope. While the APW had one E for all orbitals, the LAPW has an energy E_l for each l. In the LAPW scheme, E_l does not have to equal a KS eigenenergy, but is set to be near the middle of the range of eigenvalues that are of character l (the range is determined by imposing the empirical Wigner-Seitz rule [103, 104] on u_l). Herein lies the crucial difference between the APW and LAPW methods: through the linearization and by fixing the energy values E_l, the energy-independent secular equations become linear, making it possible to get the band energies with a single diagonalization of the hamiltonian matrix. The asymptote problem is also eliminated, for the form of $A_{lm,\mathbf{k}+\mathbf{G}}$ (and $B_{lm,\mathbf{k}+\mathbf{G}}$ as well) in the LAPW formalism does not have a vanishing denominator, which was the source of the singularity in the APW. Another difference is that full-potential calculations are possible in LAPW but not in APW.

WIEN2K has implemented an improved approach, proposed by Singh in 1991 [105], to the LAPW method. Denoted as LAPW+LO, it has extra functions in the basis set for the augmented portion of space, called local orbitals (LOs), to better describe semi-core states. The LO for a particular l and m is written as

$$\phi^{\mathrm{LO}}_{\mathbf{k}+\mathbf{G},lm}(\mathbf{r}) = \begin{cases} [A^{\mathrm{LO}}_{lm,\mathbf{k}+\mathbf{G}} u_l(r,E_{1l}) + B^{\mathrm{LO}}_{lm,\mathbf{k}+\mathbf{G}} \dot{u}_l(r,E_{1l}) & \\ \quad + C^{\mathrm{LO}}_{lm,\mathbf{k}+\mathbf{G}} u_l(r,E_{2l})] Y_{lm}(\hat{\mathbf{r}}), & r < r_{\mathrm{MT}} \\ 0, & r > r_{\mathrm{MT}}. \end{cases} \tag{3.58}$$

The second energy, E_{2l}, is the energy corresponding to the semi-core band. The decrease in efficiency, due to the larger basis set, is more than compensated for by the increase in accuracy.

FPLO

The FPLO method [94] is a full-potential scheme that uses a linear combination of nonorthogonal atomic-like basis orbitals which overlap. It will be shown that the size matrix of the eigenvalue problem is reduced to that of a minimum valence basis set. The Bloch wavefunction is written as

$$\psi_{\mathbf{k}n}(\mathbf{r}) = |\mathbf{k}n\rangle = \sum_{\mathbf{R}\mathbf{s}L} C_{\mathbf{s}L,\mathbf{k}n} |\mathbf{R}\mathbf{s}L\rangle e^{i\mathbf{k}\cdot(\mathbf{R}+\mathbf{s})}, \tag{3.59}$$

where $\mathbf{R}$ is a Bravais vector, $\mathbf{s}$ is a basis vector, and L denotes the set of quantum numbers l, m. $C_{\mathbf{s}L,\mathbf{k}n}$ is the coefficient of the basis orbital $|\mathbf{R}\mathbf{s}L\rangle$, which is made up of a localized radial function and a spherical harmonic function,

$$|\mathbf{R}\mathbf{s}L\rangle \equiv \phi_{\mathbf{s}l}(|\mathbf{r}-\mathbf{R}-\mathbf{s}|) Y_L(\mathbf{r}-\mathbf{R}-\mathbf{s}). \tag{3.60}$$

Plugging this into $\hat{H}|\mathbf{k}n\rangle = |\mathbf{k}n\rangle \epsilon_{\mathbf{k}n}$, the secular equation becomes

$$\sum_{\mathbf{R}\mathbf{s}L} \left(\langle \mathbf{0}\mathbf{s}'L'|\hat{H}|\mathbf{R}\mathbf{s}L\rangle - \langle \mathbf{0}\mathbf{s}'L'|\mathbf{R}\mathbf{s}L\rangle \epsilon_{\mathbf{k}n} \right) C_{\mathbf{s}L,\mathbf{k}n} e^{i\mathbf{k}\cdot(\mathbf{R}+\mathbf{s}-\mathbf{s}')} = 0. \tag{3.61}$$

The Hamiltonian matrix and the overlap matrix are respectively defined to be

$$H_{\mathbf{s}'L',\mathbf{s}L} = \sum_{\mathbf{R}} \langle \mathbf{0}\mathbf{s}'L'|\hat{H}|\mathbf{R}\mathbf{s}L\rangle e^{i\mathbf{k}\cdot(\mathbf{R}+\mathbf{s}-\mathbf{s}')}, \tag{3.62}$$

$$S_{\mathbf{s}'L',\mathbf{s}L} = \sum_{\mathbf{R}} \langle \mathbf{0}\mathbf{s}'L'|\mathbf{R}\mathbf{s}L\rangle e^{i\mathbf{k}\cdot(\mathbf{R}+\mathbf{s}-\mathbf{s}')}. \tag{3.63}$$

In FPLO, valence states (indexed as v) and core states (c) are separated to reduce the size of the matrix problem. Thus the overlap matrix can be presented in four blocks,

$$S = \begin{bmatrix} S_{cc} & S_{cv} \\ S_{vc} & S_{vv} \end{bmatrix}, \tag{3.64}$$

where

$$S_{cc} = \langle \mathbf{R}'\mathbf{s}'c'|\mathbf{R}\mathbf{s}c\rangle = \delta_{c'c}\delta_{\mathbf{R}'+\mathbf{s}',\mathbf{R}+\mathbf{s}}, \tag{3.65}$$

$$S_{cv} = \langle \mathbf{R}'\mathbf{s}'c'|\mathbf{R}\mathbf{s}v\rangle = S_{vc}^{\dagger}, \tag{3.66}$$

$$S_{vv} = \langle \mathbf{R}'\mathbf{s}'v'|\mathbf{R}\mathbf{s}v\rangle. \tag{3.67}$$

And the Hamiltonian matrix becomes

$$H = \begin{bmatrix} H_{cc} & H_{cc}S_{cv} \\ S_{vc}H_{cc} & H_{vv} \end{bmatrix}, \tag{3.68}$$

where

$$H_{cc} = \langle \mathbf{R}'\mathbf{s}'c'|\hat{H}|\mathbf{R}\mathbf{s}c\rangle = \epsilon_{\mathbf{s}c}\delta_{c'c}\delta_{\mathbf{R}'+\mathbf{s}',\mathbf{R}+\mathbf{s}}, \tag{3.69}$$

$$H_{vv} = \langle \mathbf{R}'\mathbf{s}'v'|\hat{H}|\mathbf{R}\mathbf{s}v\rangle. \tag{3.70}$$

A Cholesky factorization is applied to the overlap matrix,

$$S = S^l S^r = \begin{bmatrix} 1 & 0 \\ S_{vc}^l & S_{vv}^l \end{bmatrix} \begin{bmatrix} 1 & S_{cv}^r \\ 0 & S_{vv}^r \end{bmatrix}, \tag{3.71}$$

which implies

$$S_{vc} = S_{vc}^l = S_{cv}^{r\dagger} = S_{cv}^{\dagger}, \tag{3.72}$$

$$S_{vv}^l S_{vv}^r = S_{vv} - S_{vc}S_{cv} \tag{3.73}$$

The secular equation (3.61), simplified to $HC = SC\epsilon$, can be diagonalized:

$$(S^l)^{-1}H(S^r)^{-1}(S^rC) = (S^rC)\epsilon, \tag{3.74}$$

where $S^r C \equiv D$ is the unitary matrix. With

$$(S^l)^{-1} = \begin{bmatrix} 1 & 0 \\ (S^l_{vv})^{-1} S_{vc} & (S^l_{vv})^{-1} \end{bmatrix} \tag{3.75}$$

and

$$(S^r)^{-1} = \begin{bmatrix} 1 & -S_{cv}(S^r_{vv})^{-1} \\ 0 & (S^r_{vv})^{-1} \end{bmatrix}, \tag{3.76}$$

we get

$$(S^l)^{-1} H (S^r)^{-1} = \begin{bmatrix} 1 & 0 \\ (S^l_{vv})^{-1} S_{vc} & (S^l_{vv})^{-1} \end{bmatrix} \begin{bmatrix} H_{cc} & 0 \\ S_{vc} H_{cc} & (H_{vv} - S_{vc} H_{cc} S_{cv})(S^r_{vv})^{-1} \end{bmatrix} \tag{3.77}$$

$$= \begin{bmatrix} H_{cc} & 0 \\ 0 & (S^l_{vv})^{-1}(H_{vv} - S_{vc} H_{cc} S_{cv})(S^r_{vv})^{-1}. \end{bmatrix} \tag{3.78}$$

which leads to

$$D = \begin{bmatrix} 1 & 0 \\ 0 & D_{vv} \end{bmatrix}. \tag{3.79}$$

Therefore, our eigenvalue problem is greatly reduced, to

$$(S^l_{vv})^{-1}(H_{vv} - S_{vc} H_{cc} S_{cv})(S^r_{vv})^{-1} D_{vv} = D_{vv} \epsilon_v, \tag{3.80}$$

and the coefficient matrix is

$$C = (S^r)^{-1} D = \begin{bmatrix} 1 & -S_{cv}(S^r_{vv})^{-1} D_{vv} \\ 0 & (S^r_{vv})^{-1} D_{vv} \end{bmatrix}. \tag{3.81}$$

Chapter 4

High Pressure Physics Experimentation

4.1 Introduction

High pressure physics aims to study the properties of matter which undergo extreme application of pressure. It uses pressure, which is the perpendicular force applied on an object per unit area, as a thermodynamic parameter, to bring to light interesting and peculiar phenomena that can sometimes change dramatically the nature of the material that is otherwise inaccessible (see Fig. 4.1, for example). Superconductivity, superfluidity, insulator-to-metal transitions, volume collapse transitions, etc. are some of the changes that are observed when certain materials are compressed. Compressing matter can provide us with a wide range of interatomic distances, from which we can also study gradually varying states of electronic, magnetic, and structural properties.

4.2 Diamond Anvil Cell

High pressure physics is highly dependent on the available technology of apparatuses that can compress materials to such high pressures. Before the 20th century, the maximum pressure that could be achieved in the laboratory was 3 kbar (3000 atm). After a stagnancy in the field, Bridgman brought high pressure research into a more active era in the 1900s with his development of the piston-cylinder device [106] and the opposed anvil cell [107], both of which increased laboratory pressures to an order of 10 GPa (100 kbar).

In 1959, Weir et al. [108] took the concept of Bridgman's opposed anvils to invent the first single-crystal diamond anvil cell (DAC). Before the DAC, the best anvils were

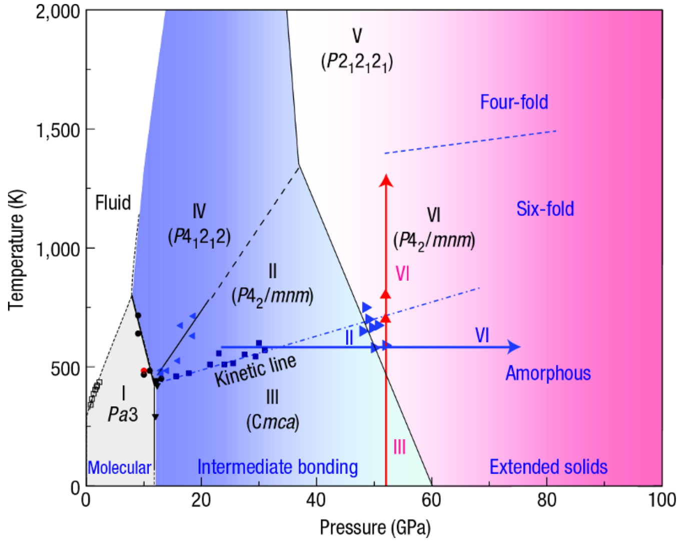

Figure 4.1. The rich phase diagram of CO_2 courtesy of Ref. 7. CO_2 has multiple phases at different temperatures and pressures, ranging from a simple molecular gas to a fully covalent solid.

made of tungsten carbide (WC), which is a very hard compound in its own right but yet requires a bulky contraption to get to pressures of only a few tens of gigapascals. With the switchover to diamond, the strongest and hardest material in the world, such is not necessary. Today, DACs, a schematic of which is shown in Fig. 4.2, can put forth static pressures of over 300 GPa, and is the only device that can do so. The DAC uses two opposing diamonds—cut to have culets—as the anvils, and a gasket is placed between the culets to create a chamber which holds the sample of interest. Force is exerted on the tables of the diamonds and is concentrated at the culets to produce ultra-high local pressure within the chamber.

Another very useful and convenient trait of diamond is its high transparency. This is fully exploited in DACs for optical experiments. In fact, utilization of diamond for its transparency was realized before its effectiveness for achieving high pressure. In 1950, before the invention of the DAC, Lawson and Tang [9] replaced the cast beryllium in their Be bomb [109]—developed for obtaining x-ray powder diffractions—with diamond, in order to avoid the Debye-Scherrer rings diffracted by Be. In the "split-diamond" bomb (see Fig. 4.3), two single-crystal diamonds are cut in half and cleaved together with their tables touching. The chamber is created by drilling a hole through the center of the diamond configuration, parallel to the faces. While the Be bomb went up to 1 GPa, the

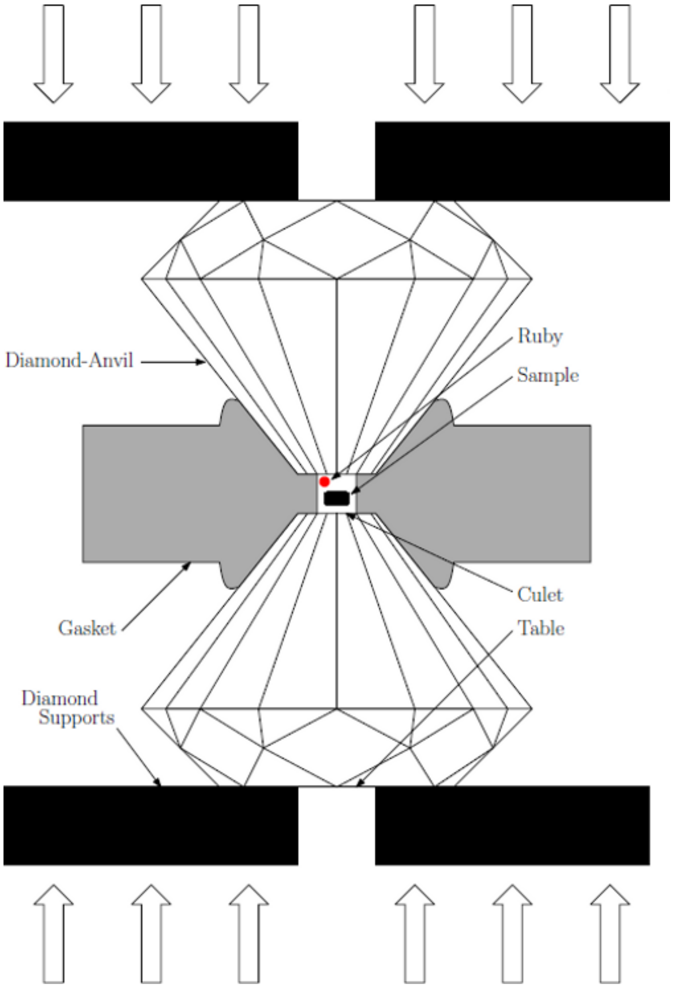

Figure 4.2. The diamond anvil cell (image taken from Ref. 8). The ruby in the sample chamber is used as a pressure sensor (see text). The diamond seats with a hole in the center for optical transmission are colored in black. The arrows indicate the direction of force applied by the cell.

split-diamond bomb could maintain a load of 2.5 GPa, and with only a few Laue spots tainting the diffraction pattern. This work paved the way for Jamison, Lawson, and Nachtrieb [110] to construct their own version of a DAC, almost concurrently (in 1959) but independently of Weir, Lippincott, and Van Valkenburg [108]. The DAC by Weir et al. also was designed with diamond's optical properties in mind (they used theirs for infrared absorption measurements).

The DAC was further improved in 1978 by Mao and Bell [111], who were able to apply pressures of up to 170 GPa [112]. Prior to this, the highest pressure one could attain was 0.5 GPa–with an NBS (National Bureau of Standards) [113] or Bassett [114] DAC. The

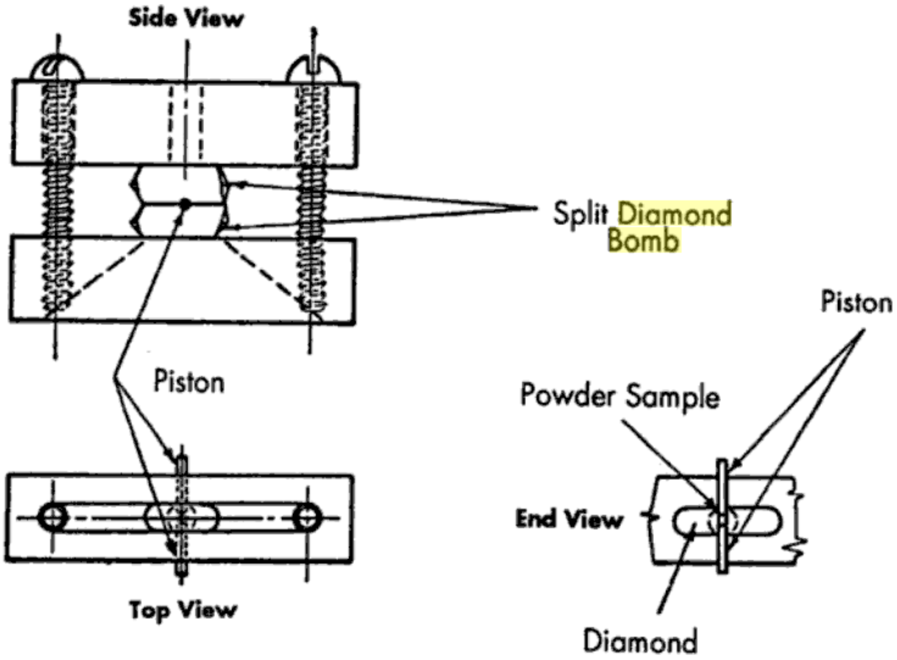

Figure 4.3. Schematic, taken from Ref. 9, of the split-diamond bomb, the first high pressure tool to utilize diamond.

Mao-Bell DAC set the basis for the membrane DAC, which was conceived and fabricated by scientists at Lawrence Livermore National Laboratory (LLNL). The membrane DAC was used in the high pressure experiments discussed in this dissertation. It employs the piston-cylinder mechanism as well as opposing anvils. A diagram and picture of the membrane DAC can be seen in Fig. 4.4. The piston and cylinder are held together by four pressure screws, which can be tightened manually to increase pressure inside the cell. But the membrane DAC gets its name due to the use of a metal membrane which holds an easily adjustable amount of inert gas, and when the membrane expands the pressure of the sample goes up. The gas is metered by a pressure controller which is connected to a standard gas cylinder as the pressure source. The controller comes with a precise metering valve so that fine tuning of the pressure is possible. The membrane DAC is highly efficient for cryogenic and x-ray diffraction (XRD) measurements, as the pressure in the cell can be altered without having to take it off its mount or disrupt the x-ray beam. In short, the membrane DAC offers remote, precise, and systematic changes in pressure.

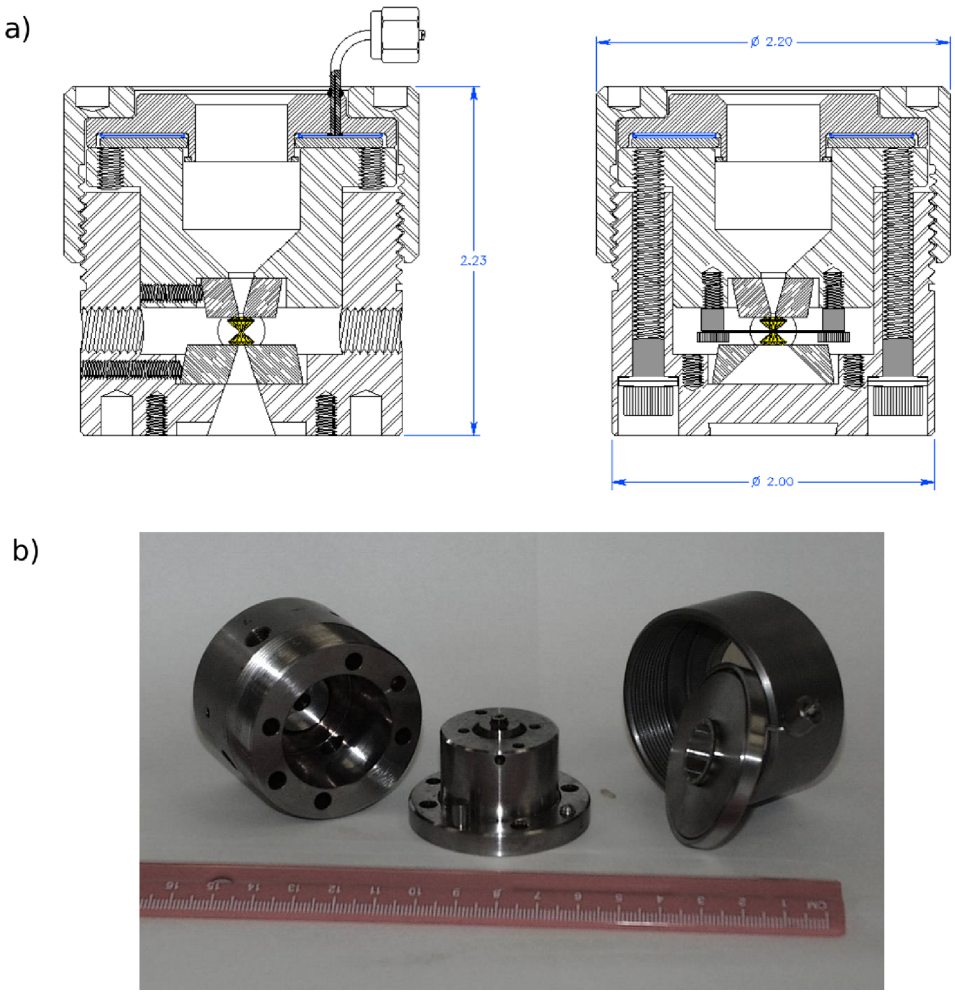

Figure 4.4. a) Mechanical drawing of two different cross-sections of the membrane DAC developed at LLNL. Numbers are in units of inches. b) Picture of the same membrane DAC, dissassembled. From left to right are the cylinder, piston, the pressure membrane, and the lid which screws onto the cylinder to keep the membrane in place. The piston pictured shows also the WC seat which is adjusted and set in place by set screws, and sitting on the seat is a diamond. A similar setup is attached to the cylinder but hidden in this view.

4.2.1 Complex components of the DAC

Diamonds

The diamonds used in DACs are 0.16–0.5 carat brilliant-cut gem stones, which can now be made artificially. The culet diameter conventionally ranges from 50 to 500 μm, and the smaller the diameter, the higher the potential maximum pressure. 500 μm-culet diamonds will apply a load of 35 GPa; 200 μm flats can generate pressures of over 100 GPa. To obtain higher pressures, the diamonds have to be beveled (see Fig. 4.5). Since

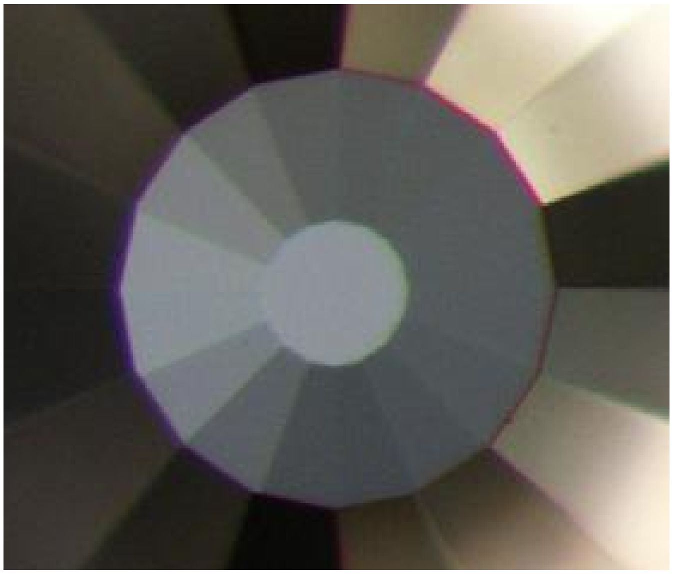

Figure 4.5. Top view of a beveled diamond.

its first use by Mao and Bell [115], it has been found that the shear stress at the eight corners is minimized greatly by beveling the anvil face. 300–500 μm culets can a beveled face of 25–100 μm in diameter.

A gradient of pressure along the face of the culet can significantly reduce the maximum attainable pressure in the chamber, as the inhomogenous pressure distribution may cause the diamonds to prematurely break. So it is important that the opposing diamonds are aligned with their axes, and that the faces are as parallel as they can be. Modern piston-cylinder DACs, such as the membrane DAC, are manufactured so precisely that the latter now is a non-issue, and the former can be resolved by adjusting the WC seats (on which the diamonds are epoxied) with the set screws.

Gaskets

The gasket in a DAC provides containment of the sample by acting as walls of the chamber. The gasket is created by drilling a tiny hole through a thin piece of metal, but not before pre-indenting it with the DAC. A thick gasket has a risk of its hole expanding beyond the culets, and pre-indentation avoids this. The gasket is indented to have a thickness of 25–40 μm. Then the chamber is created by drilling a hole with an electric discharge machine that uses a copper spark drill. A diameter that is equal to or less than half of that of the culet is chosen, and care should be taken during the drilling process so the gasket hole and culet are concentric.

The most common gasket material is rhenium, due to its great strength and high malleability. Strength is required to maintain the chamber walls at ultra-high pressures, and malleability is needed so that the gasket won't break. Re however has a high absorption for x-rays, and therefore is unsuitable in cases such as XRD settings in which the incident and emitted beams make a 90° angle, and inelastic x-ray scattering, as the x-ray has to travel through the gasket. For these types of experiments, a Be gasket is used instead. Be is more brittle than Re, but it has the advantage of having an x-ray absorption that is even lower than that of diamond. For magnetic measurements such as resistivity and susceptibility, a material called MP35N (a nickel-cobalt base alloy) may be used. MP35N not only has exceptional strength, toughness, ductility, and corrosion resistance, but it additionally has low magnetization and its resistivity is temperature-independent.

Pressure media and gas medium loading

The pressure medium plays an important role in the DAC, as it increases pressure uniformity within the chamber. Without a pressure medium, the uniaxial force generated by the DAC creates non-hydrostatic conditions, which may result in very different properties than when the sample is under hydrostatic pressure. Of course, there would be no point to the medium if it were to have high shear strength. Moreover, the appropriate medium has to be chosen so as not to mar the measurement at hand. Powdered NaCl is a soft solid that is a good pressure-transmitting medium below 30 GPa, and can double as a pressure sensor for XRD. When it is ideal to have no diffraction patterns, liquids such as mineral oil, silicon oil, and methanol-ethanol mixtures are commonly used, though they become quite non-hydrostatic beyond 10–15 GPa.

Newer technology has made possible the use of noble gases—Ar, He, H_2, and Xe. These are the best pressure media for they are inert and maintain relative softness at high pressures. While a medium like mineral oil is easy to deal with (although it requires a steady hand to transfer a microscopic drop on the tip of a needle into the sample chamber, it can be done at room temperature), difficulty arises in loading a noble gas

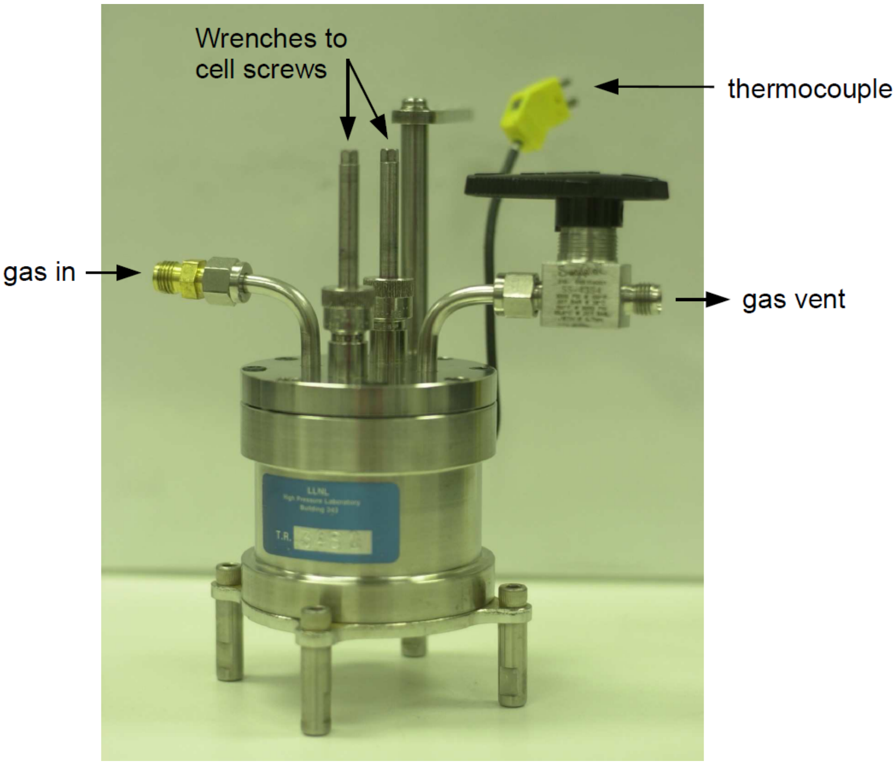

Figure 4.6. Cryogenic gas loader. The DAC is placed inside the airtight loader, and gas can flow from one end to the other or gain pressure by closing the vent valve. The sample may be exposed to the gas by opening its chamber with the two feed-through allen wrenches. The loader is immersed in liquid cryogen to liquefy the gas. Temperature in the loader is monitored by a type-K thermocouple.

in the DAC, since it actually has to be in the denser liquid form to be useful. One way to accomplish this is by using a cryogenic gas loader, seen in Fig. 4.6. The DAC with the prepared gasket is inserted in the loader before the loader is sealed tightly. Two wrenches are engaged to two of the four cell-tightening screws, allowing for the sample chamber to be opened externally. The inert gas is fed into and out of the loader, and, after some flushing, the vent valve is closed to create pressure within the loader. The entire loader is immersed in liquid N_2 or liquid Ar to liquefy the pressure medium, after which the chamber is opened to invite the liquid in. The cell (chamber) is then closed with the liquid gas trapped inside.

Another method is to use a high pressure gas loader. This is especially apt when the inert gas of choice has a lower boiling point than than of liquid N_2. A standard gas cylinder supplies the gas, which is transferred to the loading system, shown in Fig.

Figure 4.7. 30,000 psi high pressure gas loader. Gas is loaded from the cylinder (closed in this image) into the loader, and the pressure within is increased little by little, by turning the pressure intensifier ([mechanical name for the PI]).

4.7. The cell is placed inside the loader, and like the cryogenic loader, there is access to the external opening and closing of the sample chamber. The gas is pressurized by turning the handle [need better name], called the pressure intensifier, which pushes a rod inward to decrease the gas volume. A little more gas is introduced and gets compressed as well. This process is performed several times, until the loader reaches a pressure of 25,000–30,000 psi. This is enough for the gas to liquefy and be suitable for loading into the sample chamber.

Pressure sensors and pressure calibration

A pressure sensor, or pressure standard or marker, is usually placed inside the cell chamber along with the sample. A good pressure sensor should be able to accurately represent its pressure. Almost as significant as the invention of the DAC was the introduction of the ruby fluorescence method, by Forman et al. [116] in 1972, as a means of calibrating pressure inside the DAC. In years prior, pressure was estimated by applied load over area or by the XRD patterns of pressure media like NaCl. But ruby fluorescence via optical spectroscopy became the quick and easy way to make precise pressure measurements, when it was observed [116] that the wavelength of the R-line luminescence shifts linearly with pressure in the 0.1–2.2 GPa range, and that the lines broaden under non-hydrostatic pressures. Ruby is Al_2O_3 with Cr^{3+} sitting in place of some of the Al atoms. When excited by a laser, the Cr electrons will jump to a higher-energy state. Soon they decay to lower metastable states, from which they fall back into the ground state. The last step of the process is manifested via fluorescing. For ruby, two signals will seen—one due to the electric dipole transition from the lowest excited metastable energy, the other from the second lowest. In 1975, Piermarini et al. [117] showed the R_1 line (R_1 and R_2 respectively correspond to the larger and smaller signals in Fig. 4.8) is linear up to 19.5 GPa when calibrated against the compression of NaCl, using the Decker equation of state (EOS) [118]. In 1986, Mao et al. [119] revised the pressure formula based on Cu and Ag EOSs for up to 80 GPa:

$$P = \frac{A}{B}\left[\left(1 + \frac{\Delta\lambda}{\lambda_0}\right)^B - 1\right], \tag{4.1}$$

where P is the pressure in megabars, $A = 19.04$ Mbar (initial slope obtained from Ref. 117), $B = 7.665$, $\Delta\lambda$ is the R_1-line shift, and λ_0 is the wavelength of the R_1 line (the zero-pressure value of λ_0 is known to be 694.2 Å). More recently (in 2007), Silvera et al. updated the parameter values to $A = 18.76$ Mbar and $B = 10.71$.

Above 100 GPa, ruby's fluorescence weakens dramatically, and other pressure sensors are used instead. Just as NaCl can be a pressure marker when XRD measurements are being performed, so can Cu, Au, Ag, Pt, and Ta. These simple metals are used in particular due to their higher symmetry, which results in fewer diffraction lines, and the fact that their respective phases are stable up to high pressures.

4.3 X-ray Diffraction at High Pressure

XRD is a very useful diagnostic tool that can determine the crystral structure of a material. When the material is in a DAC at high pressures, however, typical laboratory x-ray diffractometers are not intense nor concentrated enough. The DAC chamber will have

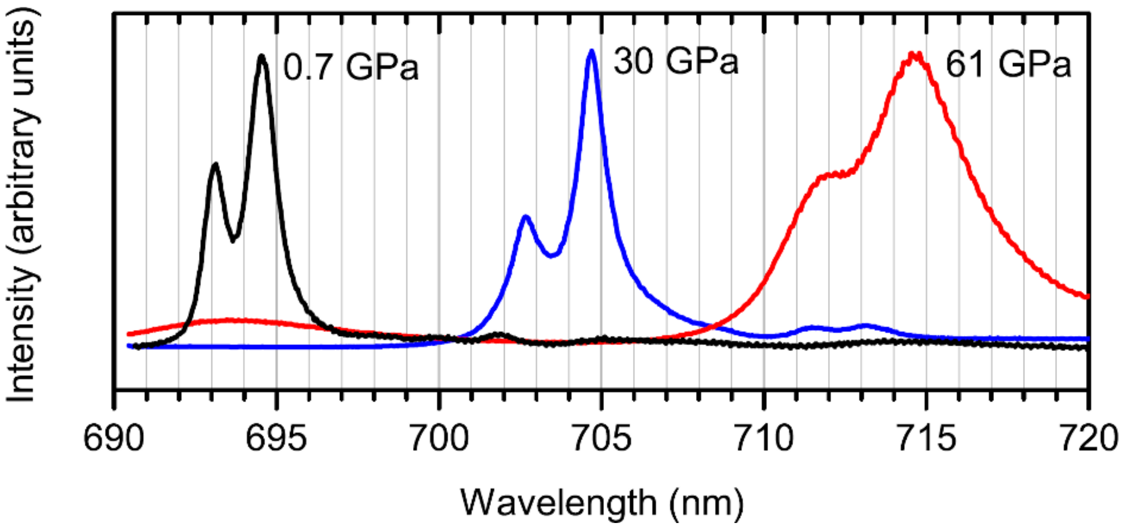

Figure 4.8. Three pairs of R_1 (bigger, right) and R_2 (smaller, left) ruby fluorescence lines for a sample of Li_2O at different pressures. Figure courtesy of Ref. 10.

a diameter of 50 μm or smaller, so an x-ray beam of a very tight focus is imperative. Moreover, the x-rays have to be hard enough to penetrate diamonds. These features are available only at third-generation synchrotrons, such as the Advanced Photon Source (APS) in Argonne, IL, the European Synchrotron Radiation Facility in France, and the Super Photon Ring in Japan, as only they can provide the exceptionally bright and collimated x-rays that make high pressure XRD experiments possible.

4.3.1 X-ray diffraction

In 1913, W. H. and W. L. Bragg, father and son, discovered that a crystalline solid produced methodical patterns of scattered x-rays, and formulated Bragg's law,

$$n\lambda = 2d \sin\Theta, \tag{4.2}$$

where d is the atomic spacing of the crystal and Θ is the angle of incident light. The integer n is called the order of reflection. A schematic of a Bragg reflection is shown in Fig. 4.9. Light is constructively reflected when the above equation holds, and intense peaks of radiation are produced, creating an XRD pattern. For a powder crystal, layers of a certain distance d can be sectioned into different layers of a different distance d' (and different Θ'), which will contribute additionally to the diffraction pattern. XRD is observed because the x-ray wavelengths are comparable to interatomic distances, and it

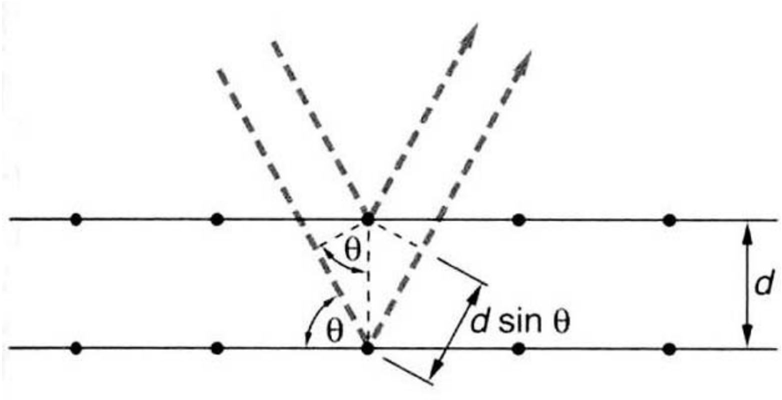

Figure 4.9. Bragg reflection from lattice planes separated by a distance d. Rays are incident and reflected. The path difference is $2d\sin\Theta$.

is possible by Rayleigh scattering.

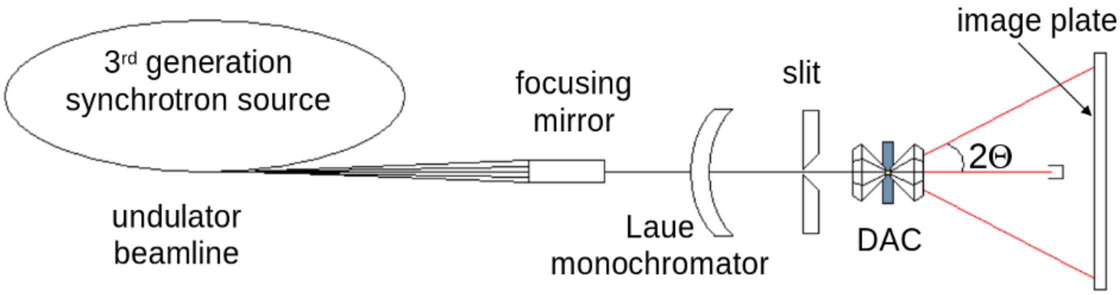

Figure 4.10. Schematic of a DAC XRD experiment. The x-ray from the beamline is fed through a focusing mirror, a monochromator, a slit, and the first diamond. The beam is then scattered by the sample, and the diffraction pattern is recorded on an image plate.

As can be seen in Fig. 4.10, the x-ray from the beamline penetrates the first diamond and scatters off the sample in the DAC chamber and through the other diamond, resulting in a diffraction pattern of Debye-Scherrer rings like Fig. 4.11 (in this case the sample is a polycrystalline powder). The intensity of an x-ray reflection has the relation

$$I(\mathbf{q}) \propto \left| \int d\mathbf{r} e^{i\mathbf{q}\cdot\mathbf{r}} \rho(\mathbf{r}) \right|^2 , \tag{4.3}$$

where $\mathbf{q}$ is the difference between the incident and reflected wave vectors, and therefore dependent on Θ, and ρ is the charge density. Hence, knowledge of Θ leads to knowledge of the lattice spacing, and the intensity of the peaks provides information on the interatomic positions.

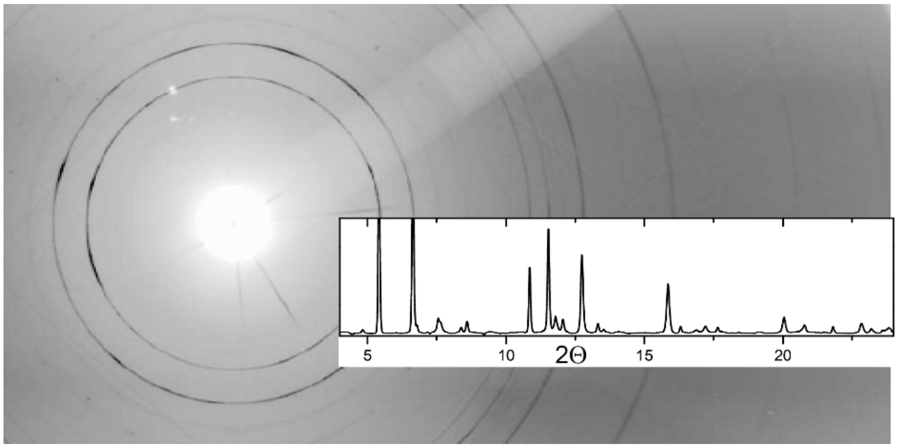

Figure 4.11. Powder XRD diffraction rings and corresponding integrated two-dimensional spectrum. Taken from Ref. 10.

Figure 4.12. View of the Advanced Photon Source. Image courtsey of Ref. 11.

As mentioned above, Fig. 4.11 shows the Debye pattern data, which collected onto an image plate. The pattern is processed with a program called Fit2D, which integrates the two-dimensional diffraction image to create a one-dimensional pattern as a function of 2Θ, also shown in Fig. 4.11.

4.3.2 The APS

The XRD measurements discussed in this work have all been taken at the APS at Argonne National Lab, so the specifics of the APS will be detailed here. At the APS, electrons are emitted from a cathode and sent through strong alternating electric fields in the linear accelerator (see Fig. 4.12), causing the electrons to accelerate to relativistic speeds with an energy of 450 MeV. They then move to the injector or "booster synchrotron", where in half a second, with the help of bending and focusing magnets, they are boosted to an energetic 7 GeV. The electrons are taken to the 350 m-diameter storage ring, which is made up of more than a thousand powerful electromagnets. The lattice of these magnets is what produces the exceedingly narrow and parallel x-rays, with a spectral brilliance of over 10^{15} photons/s/mrad^2/mm^2/0.1%bandwidth.

The HPCAT facility

APS Sector 16 is run by the High Pressure Collaborative Access Team (HPCAT), whose members are the High Pressure Physics Group of LLNL, the Geophysical Laboratory of Carnegie Institution of Washington, the Carnegie DOE Alliance Center, and the High Pressure Science and Engineering Center of University of Nevada at Las Vegas. Sector 16 has four beamlines in nine hutches. Two (16 ID) of the four, shown in Fig. 4.13, originate at dual undulator insertion device, and the other two (16 BM) start from the storage ring bending magnet. The bending magnet radiation covers a broad photon energy range, but it does not cover all hard x-rays and is not as bright as an undulator beam. In fact, the x-ray experiments done on $CaLi_2$ in 16 BM-D did not produce worthy results, due to the large beam size. The 16 ID beam on the other hand is undulated by the magnets of alternating polarity. By the time it has passed through the undulators, the beam is very intense and greatly collimated. Then the beam is split by a diamond double-crystal monochromator into a white beam, which goes to the 16 ID-D hutch, and a monochromatic beam, which is sent through another monochromator, made of a Si (220) single crystal. The monochromatic beam is focused by a pair of Kirkpatrick-Baez mirrors before it reaches 16 ID-B.

The 16 ID-B hutch

All of the successful XRD research discussed in this work has been done in the 16 ID-B hutch. The 16 ID-B beam boasts an energy range of 27–36 keV (over 10 keV is required to go through the diamond), a flux of 5×10^{10} photons/s at the sample position, and a spatial resolution of less than 10 μm.

In 16 ID-B, the experimental equipment is there to aid with cryogenic conditions. Hence, low-temperature XRD experiments are possible here. This entails inserting the DAC in a CRYO Industries He gas-flow cryostat, shown in Fig. 4.14, which allows for liquid He to continuously flow through. The DAC is in contact with a copper block to promote heat transfer. Two thermocouples touch the DAC and one touches the copper block. All of the electrical wire can be connected externally, as can been seen above the lid in the left-hand photo. In principle the temperature inside the cryostat can be brought down to 4.2 K.

16 ID-B supports angle-dispersive XRD (ADXRD). Another kind of XRD is energy-dispersive XRD (EDXD), which uses a polychromatic x-ray at a fixed angle. EDXD however usually has a low resolution and a lower flux (since x-rays are gathered at only one solid angle). The Debye rings may not turn out uniform, and sometimes some reflections are completely missed, particularly at high pressures; this is because the sample may favor a certain orientation due to non-hydrostatic stresses in the DAC. ADXRD on the other hand uses a single, monochromatic source of x-ray, so all angles (to a degree) are covered, and it is entirely possible to use a high-resolution, high-flux beam; it is therefore the preferred approach for high pressure XRD. Fig. 4.15 shows the ADXRD setup in 16 ID-B.

For the x-ray experiments explained in this dissertation, the mar345 Image Plate was used. The x-ray ionizes the Eu^{2+} ions on the image plate to $\mathrm{Eu}^{3}+$ ions at the point of contact. The excess electrons are excited to the conduction band, and drop back to recombine with the ions or get stuck in color centers. Color centers, or F centers, normally refer to vacancy defects in a crystal, but the color centers of the image plate are deliberate. F centers attract electrons because they are missing a halogen anion. The trapped electrons stay stuck until the image plate is irradiated (with a blue light, to allow recombination with Eu^{3+}) to reuse for a different diffraction run.

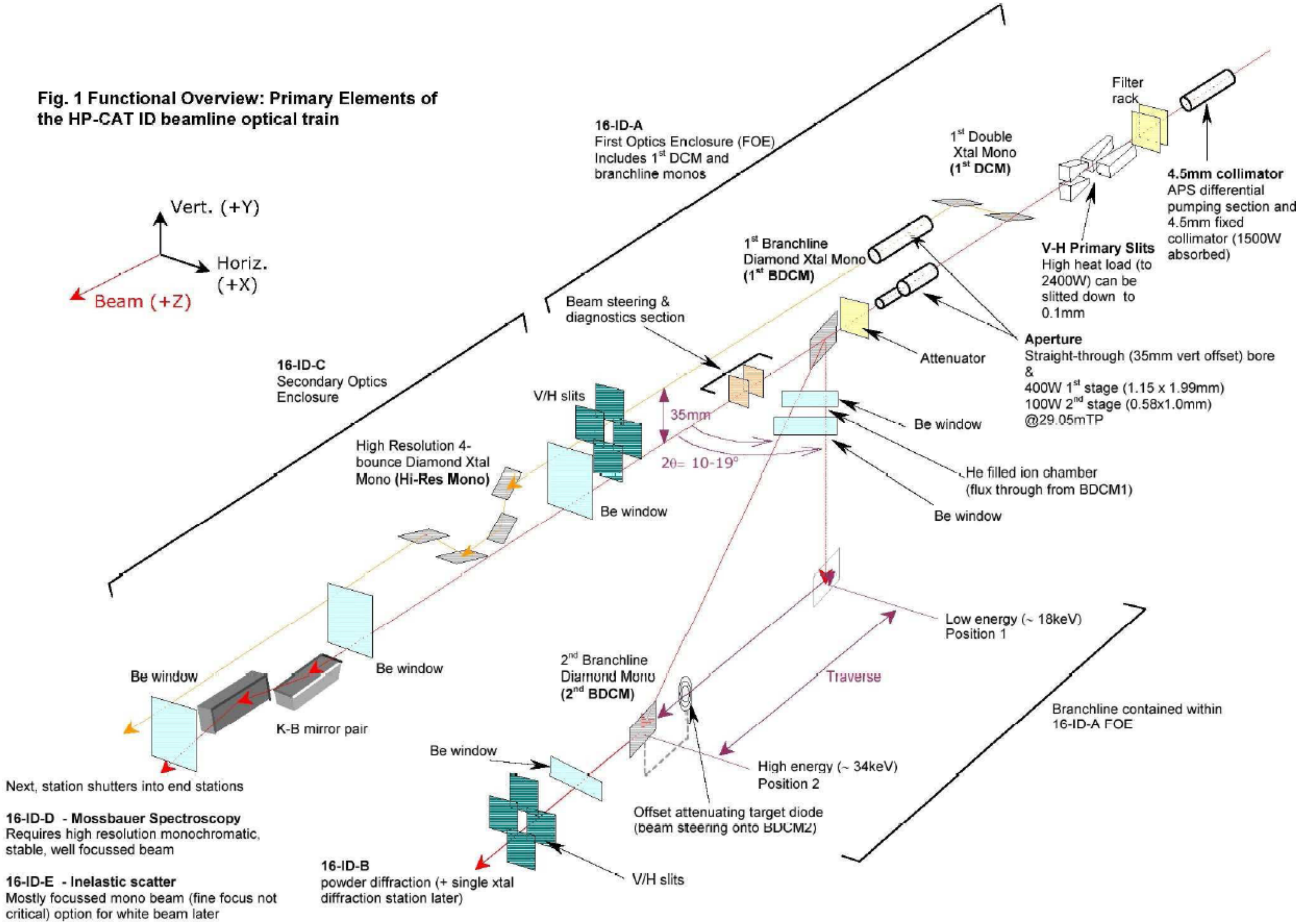

Figure 4.13. APS Sector 16 insertion device beamline optical train.

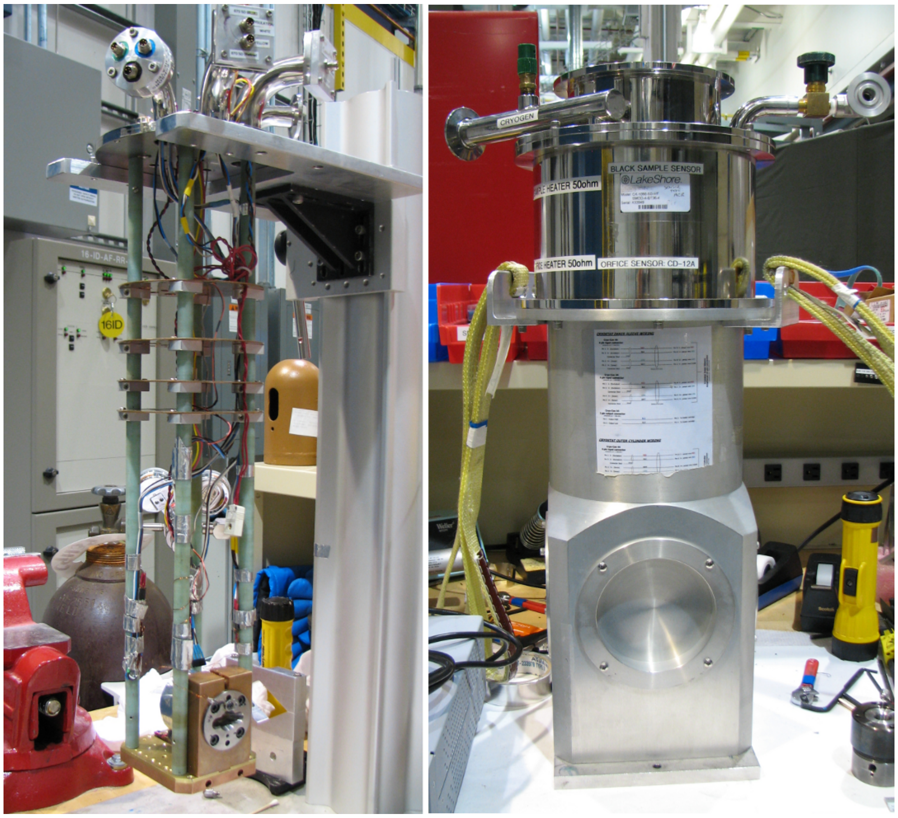

Figure 4.14. (Left) inner components and (right) outer shell of the CRYO Industries continuous He gas-flow cryostat at 16 ID-B. The shell's circular "window" is made out of sapphire.

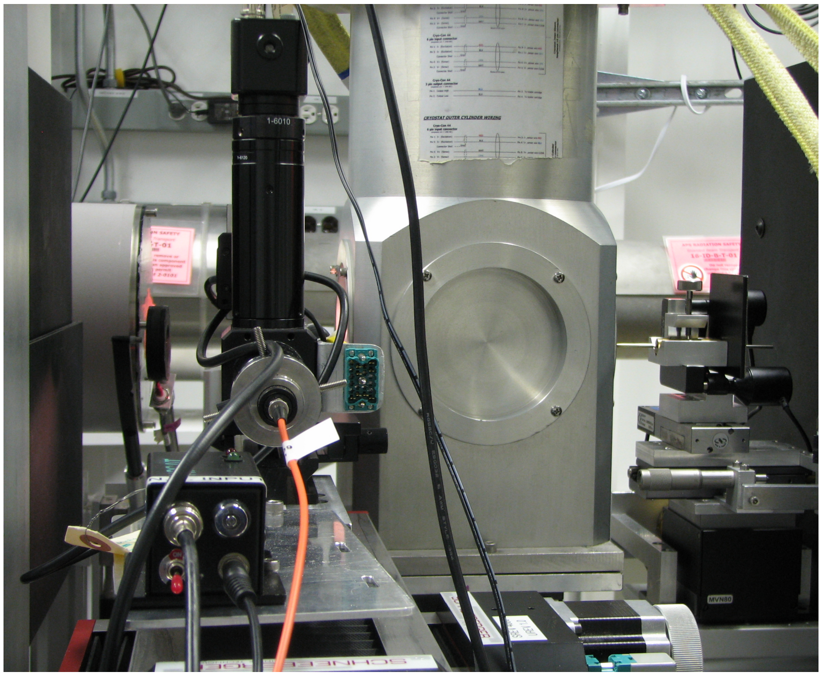

Figure 4.15. [NEED TO ALTER THIS] The cryostat mounted at the beam of 16 ID-B. The x-ray beam shoots out from the right, through the sapphire windows and DAC, and to the image plate, hidden behind the black covers in this picture.

Chapter 5

NaAlSi: A Self-Doped Semimetallic Superconductor

This work was done in collaboration with S. Banerjee, E. R. Ylvisaker, and W. E. Pickett of UC Davis, and pubished in Ref. 120.

5.1 Introduction

The discovery of new superconductors in unexpected materials brings the potential to understand something deeper, or perhaps something different, about the underlying properties that favor superconducting pairing. The discovery of high-temperature superconductivity (to 56 K so far) in Fe-pnictides [32] is a recent spectacular example, and is also an example of close relationships between magnetism and superconductivity, though the connections are still far from clear.

New superconductors where little or no magnetic effects are present are also arising, and these clearly involve different physics fromthe cuprate or Fe-pnictide high-temperature superconductors. Electron-doped MNCl, where M = Zr or Hf, becomes superconducting immediately upon undergoing the insulator-to-metal transition [121–124], which, in the case of M = Hf, is higher than 25 K. The similarly layered, electron-doped, ionic insulator TiNCl superconducts up to 16 K. Magnetic behavior in these materials is at most subtle, amounting to an enhancement in Pauli susceptibility near the metal-to-insulator transition [125].

In this chapter we address the ternary silicide NaAlSi (space group $P4/nmm$, $Z = 2$), another ionic and layered material that shows unexpected superconductivity, and does so in its native (without doping or pressure) stoichiometric state, at 7 K [126]. NaAlSi introduces new interest from several viewpoints. First, it is an *sp* electron superconductor, with a high T_c for such materials at ambient pressure. Pb is an *sp* superconductor with comparable T_c (7.2 K) but with simple metallic bonding and heavy atoms, making it very different. Doped Si [127] and doped diamond [128] superconduct in the same range, and are of course very different classes of materials. A more relevant example is the pseudo-ternary compound $\mathrm{Ba}_{1-x}\mathrm{K}_x\mathrm{BiO}_3$ (BKBO), which undergoes an insulator-to-metal transition for $x \approx 0.4$, beyond which its T_c surpasses 30 K [129, 130].

Second, the Al-Si layered substructure is like that of the Fe-As layer in the Fe-pnictide superconductors, raising the possibility of some connections between their electronic structures. In fact, NaAlSi has the same structure as the Fe-pnictide “111” compounds, with Al being tetrahedrally coordinated by Si (analogous to Fe being tetrahedrally coordinated by As). In spite of their structural similarities, these compounds have major differences; for example, the Fe pnictides are 3*d* electron systems with magnetism, while NaAlSi is an *sp* electron system without magnetism.

Third, NaAlSi is the isovalent sister (one row down in the periodic table for each atom) of LiBC. LiBC itself is (in a sense) isovalent and also isostructural to MgB_2; however due to the B-C alternation around the hexagon in the honeycomb-structure layer, LiBC is insulating rather than conducting. When hole-doped while retaining the same structure, $\mathrm{Li}_{1-x}\mathrm{BC}$ has stronger electron-phonon coupling than does MgB_2 [50]. While NaAlSi has a substantially different structure than LiBC, its isovalence and its combination of covalence with some ionic character is shared with LiBC.

Yet another closely related compound is CaAlSi, whose two different stacking polymorphs and parent structure superconduct in the 5–8 K range [49, 131]. Linear-response and frozen-mode calculations indicate electron-phonon coupling is the likely mechanism; in particular, an ultra-soft phonon mode appears and is suggested to play a role in the superconductivity [132–137]. It is curious that in this compound, where divalent Ca (comparing it with NaAlSi) contributes one additional electron into the Al-Si *sp* bands, the preferred structure is that of AlB_2 (*i.e.*, MgB_2) with sp^2 planar bonding [132, 133, 135] rather than the more sp^3-like bonding in NaAlSi. Electronic structure

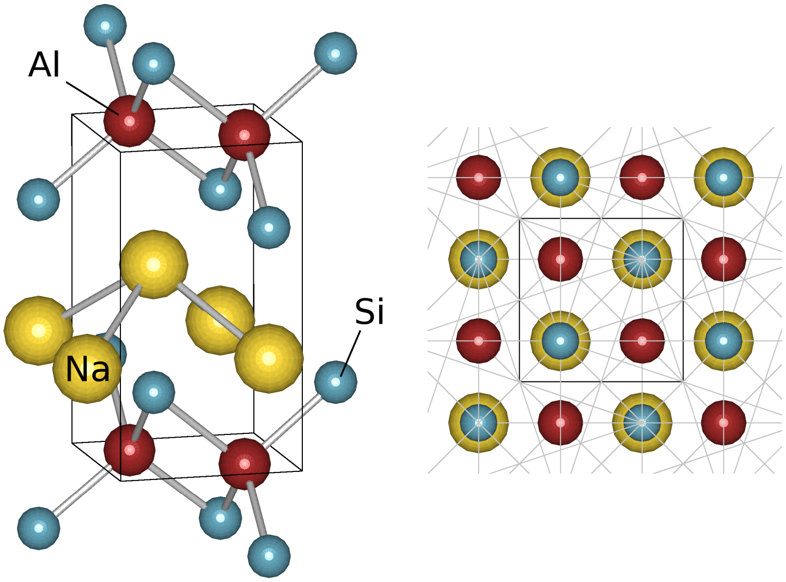

Figure 5.1. Crystal structure obtained using VESTA [12] of NaAlSi. Four Si atoms tetrahedrally surround an Al atom, and these Al-Si networks sandwich the Na atoms. The unit cell is outlined in black.

calculations show that CaAlSi has one electron in the conduction band above a bonding-antibonding band separation at the NaAlSi band-filling level, a situation which would not appear to be particularly favorable for sp^2 bonding.

In this paper we analyze first-principles electronic structure calculations that reveal that NaAlSi is a naturally self-doped semimetal, with doping occurring—thus charge transfer occurring—between covalent bands within the Al-Si substructure and 2D free-electron-like bands within the Al layer. The resulting small FSs are unusual, complicated by the small but seemingly important interlayer coupling along the crystalline z-axis.

5.2 Computational Methods

First-principles, LDA calculations were carried out using the full-potential local-orbital scheme [94]. A k-point mesh of $20 \times 20 \times 12$ was used, and the Perdew-Wang 92 approximation [79] was applied for the exchange-correlation potential. The experimental lattice constants obtained by Kuroiwa *et al.* [126] ($a = 4.119$ Å and $c = 7.632$ Å) and internal coordinates of $z_{Na} = 0.622$, $z_{Si} = 0.223$, published by Westerhaus and Schuster [138], were used in our calculations.

5.3 Electronic Structure

5.3.1 Discussion of the band structure

The calculated band structure of NaAlSi is shown in Fig. 5.2. As expected, the Na ion gives up its electron to the Si-Al-Si trilayer (see Fig. 5.1), which may have some ionic character, though it is not easy to quantify (the valence bands have much more Si character than Al character, seemingly more than suggested by their number of valence electrons). There are several readily identifiable classes of bands. Two primarily Si 3s bands, with a small amount of Al 3s character, are centered 9 eV below the Fermi level ε_F and have a width of 2.5 eV. Above them there is a six-band complex of Al-Si s-p bands (heavily Si) that are very nearly filled, the band maximum only slightly overlapping ε_F.

Above ε_F lie non-bonding and antibonding bands, and the Na s bands. Among these there are a pair of distinctive bands, which can be identified most easily by their Al s character in the top panel of Fig. 5.2. These bands are nearly free-electron-like with large dispersions, and cross many other bands with little mixing. Along Γ-M they are degenerate and easily identifiable in Fig. 5.2, as they disperse up through the Fermi level to nearly 10 eV at the M point. Along Γ-X, and similarly at the top of the zone Z-R, they are distinct: one again disperses upward rapidly, cutting through many other bands, also to nearly 10 eV at X; the other disperses much more weakly to X, with a bandwidth of about 2 eV. Their Al s character and nearly vanishing Si character identify these as free-electron states, in which electrons move down channels of Al atoms separately in x and y directions. (Note that their lack of k_z dispersion identifies them as planar bands.) There is some coupling to the states in a parallel channel of Al atoms, giving rise to the 2 eV transverse dispersion. These bands lie 0.5 eV below ε_F at Γ and contain electrons. Without interference with other bands near the Fermi level and supposing them to be isotropic in the plane (but see below), such FSs might include 3–4% of the area of the zone, which would equate to an intrinsic electron doping for two bands, both spins of around 0.12–0.16 carriers per unit cell, and the concentration of hole carriers would be equal. The anisotropy, discussed below, makes the actual carrier concentration much lower.

The small overlap of valence and conduction bands results in semimetallic character

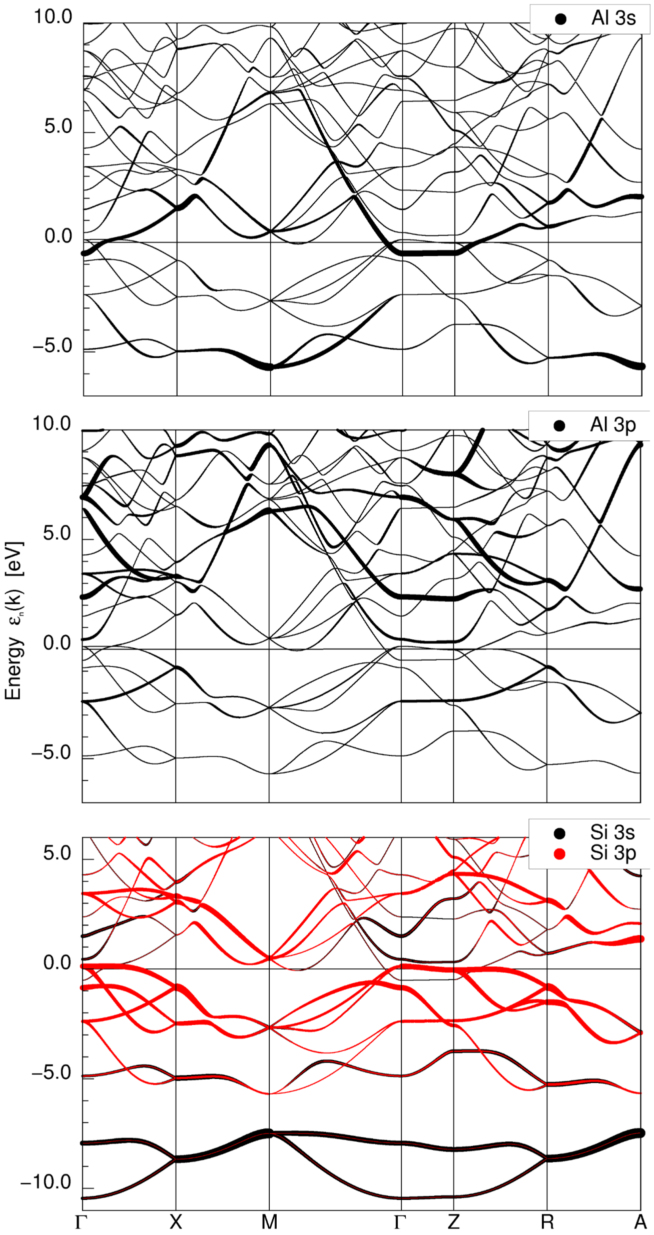

Figure 5.2. Band structure, with projected fatbands, of NaAlSi. Top panel: the Al $3s$ character of bands is indicated by broadening. A doubly degenerate pair of broad bands is evident along the Γ-M direction. Middle panel: Al $3p$ character is weak below 2–3 eV. Bottom panel: Si $3s$ (black) bands below -8 eV, and Si $3p$ in the valence bands and lower conduction bands.

and small Fermi surfaces. The valence bands are quite anisotropic. Looking at the valence bands along Γ-X, one might try to characterize them as one "heavy-hole" and one "light-hole" band, degenerate at Γ, with the band maximum lying 0.13 eV above ε_F. However, the heavy hole band is actually almost perfectly flat for the first third of the

Γ-X line, before dispersing downward across ε_F and farther below. Due to this flatness, the band cannot be characterized by an effective mass. The conduction bands contribute the pair of light electron bands described above. In addition, one conduction band dips slightly below the Fermi level along Γ-M near M.

The fatbands representation in Fig. 5.2 that reveals the dominant band character shows that the Si $3p_x$, $3p_y$, and Al $3s$ orbitals dominate the valence states near ε_F. As anticipated from consideration of the layered structure as mentioned earlier, the electronic structure is quasi-2D, with generally small dispersion along k_z near ε_F. However, the small k_z dispersion of one band is important in determining the geometry of the FSs, as discussed in more detail below.

5.3.2 Density of states

Figure 5.3 shows the total, partial, and projected DOSs of NaAlSi, in units of states per eV per unit cell. The Na contribution near the Fermi level is negligible and thus not shown. Except for a strong dip ("pseudogap") near the Fermi level and a less severe dip in the -3 to -4 eV range, the DOS hovers around 3 states/eV throughout both valence and conduction bands. Within the pseudogap encompassing the Fermi energy, there is an anomalous sharp and narrow peak with ε_F lying on its upper slope, as noted previously by Kuroiwa *et al.* [126]. The value of $N(\varepsilon_F)$ is 1.1 states/eV (both spins). We discuss below the FSs of both hole (Si) and electron (Al) character.

It seems clear that the transport properties and low-energy properties (which have not yet been reported), and in particular the superconductivity of NaAlSi, are intimately associated with this sharp and narrow peak in the DOS, which includes the Fermi level. The projected DOS shows the flat bands that give rise to this peak are very strongly Si-derived. There is Al $3s$ character that turns on just below ε_F, but it is relatively small compared to the Si character at ε_F, and its magnitude remains low and nearly constant through the peak. There is Al $3p$ character of the same magnitude in the vicinity of the Fermi level.

Due to the curious nature of the peak and its importance because it lies very near ε_F, we have investigated its origin. The top edge of the peak coincides with the flat band along Γ-X at 0.13 eV. The width of the peak, about 0.35 eV, must be due to dispersion

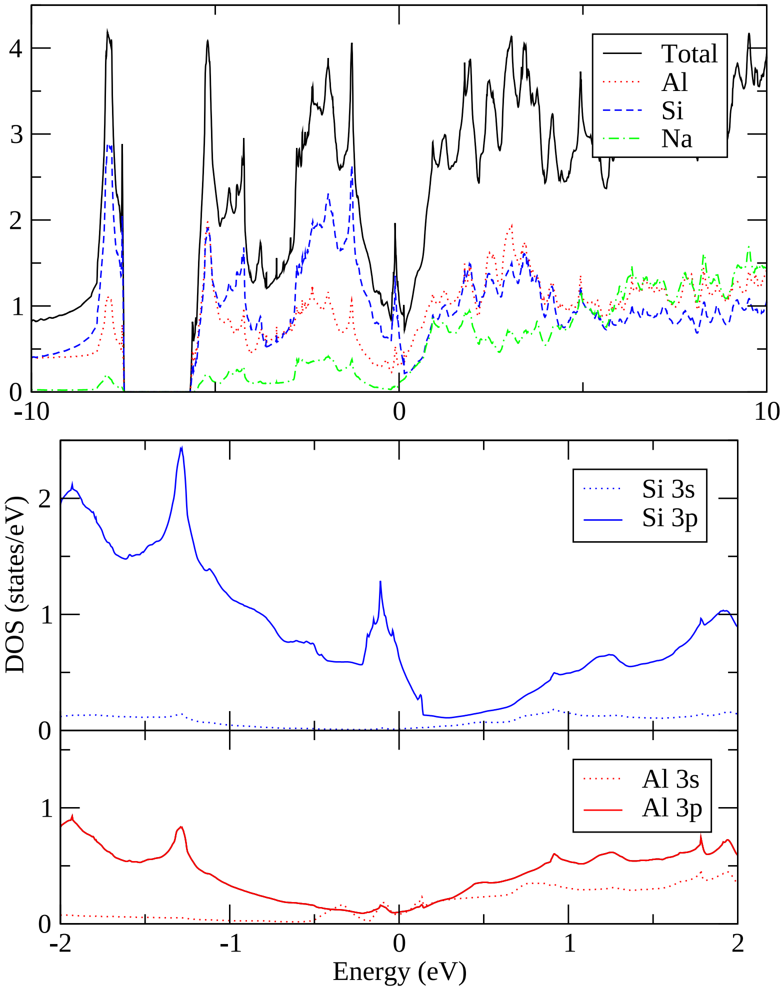

Figure 5.3. Total and partial (atom- and orbital-projected) DOSs of NaAlSi. Top panel: Total and atom-projected DOS in a 20 eV-wide region, showing the pseudogap centered at the Fermi level (the zero of energy) punctuated by the curiously narrow and sharp peak at the Fermi level. Middle panel: expanded view of the peak, and the variation of the DOS near the Fermi level, separated into Si s and p contributions. Lower panel: the Al s and p character; the s character "turns on" just below the Fermi level.

and band mixing away from the symmetry lines. Since these effects are not evident in the band structure, we have examined the bands off symmetry lines, and specifically in the $k_z = 0.6\pi/c$ plane, since this is the value of k_z where the weakly dispersing band near ε_F crosses the Fermi level. The bands in two directions in the plane, from ($0.042\pi/a$, 0, $0.6\pi/c$) to two zone boundary points are pictured in Fig. 5.4. The Al-derived conduction band is highly dispersive, and moreover hardly mixes with the valence bands, so it is not relevant. Although only $0.042\pi/a$ off the Γ-Z line, the valence bands' degeneracy is split by 0.2 eV, and in the k_x direction one band is strongly dispersive downward, while

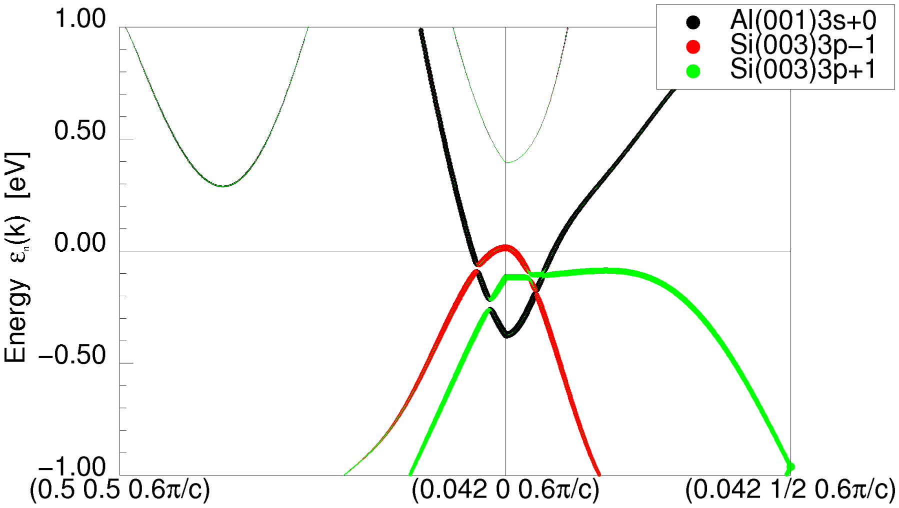

Figure 5.4. Bands along two lines in the $k_z = 0.6\pi/c$ plane, near the Fermi level, showing a flat band (one of the two Si-derived valence bands) lying at the energy of the DOS peak.

the other is flat halfway across the zone, as is also the case for $k_z = 0$ (the original band structure plot). It is this region of the zone, and this band, that contributes to the peak, and is not due to mixing of bands but rather to small but important disperion along k_z but practically no dispersion in k_x until halfway across the zone.

Nonetheless, the slope of the DOS at ε_F is rather steep, and this feature, along with the low value of $N(\varepsilon_F)$, may give rise to high thermopower for the material, as often occurs in doped semiconductors. The standard low-temperature limit of thermopower (the Seebeck coefficient tensor) $\mathbf{S}(T)$ in semiclassical Bloch-Boltzmann theory is

$$\mathbf{S}(T) \to -\frac{\pi^2 k_B}{3e} \left.\frac{d \ln \boldsymbol{\sigma}(\varepsilon)}{d\varepsilon}\right|_{\varepsilon_F} k_B T. \tag{5.1}$$

The conductivity tensor $\boldsymbol{\sigma}(\varepsilon)$ can be written in terms of the average velocity ($\vec{v}(\varepsilon)$) product, DOS, and scattering time $\tau(\varepsilon)$ over the constant energy (E) surface:

$$\boldsymbol{\sigma}(\varepsilon) = 4\pi e^2 \langle \vec{v}(\varepsilon)\vec{v}(\varepsilon)\rangle N(\varepsilon)\tau(\varepsilon). \tag{5.2}$$

The thermopower thus picks up contributions from the energy variation of three quantities: the dyadic product $\langle \vec{v}\vec{v}\rangle$, $N(\varepsilon)$, and $\tau(\varepsilon)$. Often the energy dependence of τ is neglected, out of lack of detailed knowledge, though it also can be argued to follow roughly $1/\tau(\varepsilon) \propto N(\varepsilon)$ for elastic scattering. The energy dependence of $v^2(\varepsilon)$ also counteracts the energy dependence of $N(\varepsilon)$. Nevertheless it is observed that materials with large slope in $N(\varepsilon)$ frequently have large thermopower. For NaAlSi we calculate $d\ln N(\varepsilon)/d\varepsilon|_{\varepsilon_F} = -4.0$ eV^{-1}. This value can be compared with other materials that have fine structure near the Fermi level: TiBe$_2$, where $d\ln N(\varepsilon)/d\varepsilon|_{\varepsilon_F} = 10$–$12$ eV^{-1} and $N(\varepsilon_F)$ also is much larger [139]; and MgCNi$_3$ with its very impressive peak very near ε_F, for which $d\ln N(\varepsilon)/d\varepsilon|_{\varepsilon_F}$ ranges from -15 to -20 eV^{-1} [140].

For a diagonal conductivity tensor, as is the case here, the energy derivative of diagonal elements of $\boldsymbol{\sigma}$ that occurs in Eq. 5.1 can also be expressed, straightforwardly from the expression given by Ashcroft and Mermin [141] following an integration by parts, as

$$\frac{1}{\sigma}\frac{d\sigma}{d\varepsilon} = \frac{d\ln\tau(\varepsilon)}{d\varepsilon} + \mathcal{M}^{-1}(\varepsilon)[v^2(\varepsilon)]^{-1}, \tag{5.3}$$

where $\mathcal{M}^{-1}(\varepsilon)$ is (a diagonal element of) the inverse mass tensor (second derivative of ε_k) averaged over the constant energy surface. This expression provides an alternate viewpoint to the usual expression follow from the equations above,

$$\frac{d\ln\sigma}{d\varepsilon} = \frac{d\ln\tau(\varepsilon)}{d\varepsilon} + \frac{d\ln v^2}{d\varepsilon} + \frac{d\ln N(\varepsilon)}{d\varepsilon}. \tag{5.4}$$

and this latter expression is more stable to evaluate numerically.

For any quantitative estimate for a semimetal, the expression must be generalized to two-band form (electrons and holes). The valence and conduction bands have differing signs of their effective masses, and for NaAlSi the effective mass $\mathcal{M}$ will be energy dependent (the bands are not simply parabolic at $E(\varepsilon_F)$). The energy variation of the scattering time for elastic scattering might lead to a simplification, since it should be dominated by the availability of final states—*i.e.*,

$$\frac{d\ln\tau(\varepsilon)}{d\varepsilon} \approx \frac{d\ln N(\varepsilon)}{d\varepsilon} \tag{5.5}$$

holding separately for electrons and holes.

A significant complication arises, however, because the thermopower is not a response function itself, but rather the ratio of two response functions, each of which involves a sum over bands. In addition, the temperature dependence of the electron and hole chemical potentials (hence carrier densities) are coupled. Even in the simple case of a semimetal arising from quadratic bands, the expressions lose any pedagogic value, although their evaluations require modest numerical calculations.[142] The generalization

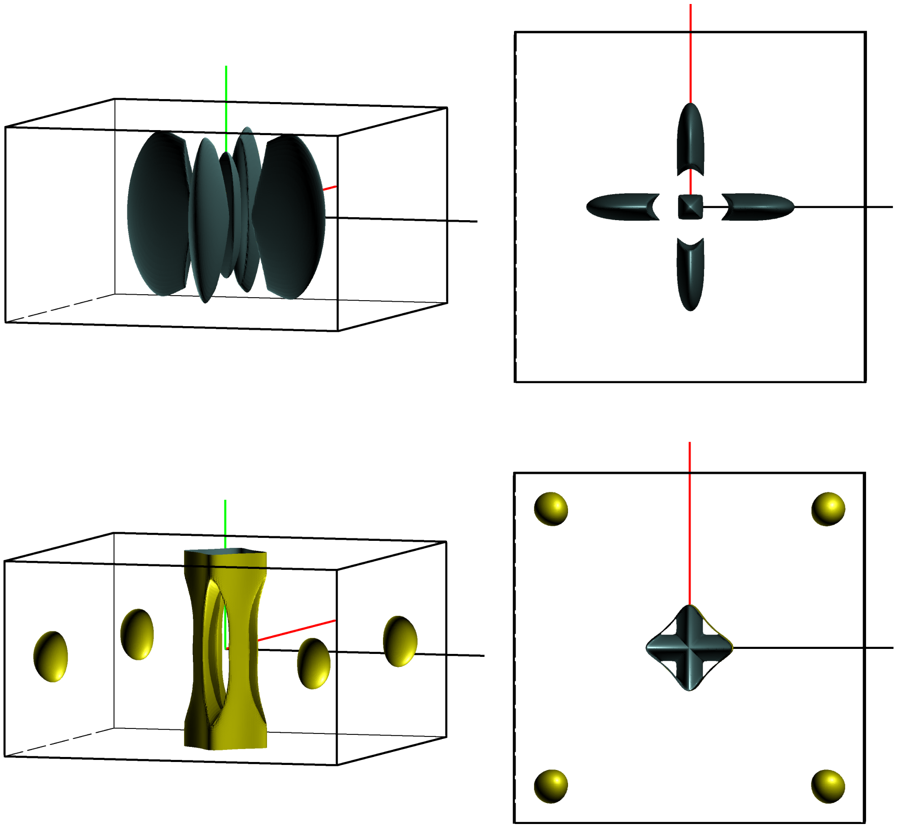

Figure 5.5. Views from the xy-plane (left) and top (right) of the FSs of NaAlSi, centered at Γ. The blue (dark) surfaces enclose holes and the yellow (light) surfaces enclose electrons.

to non-quadratic bands as in NaAlSi is beyond the scope of this paper, though a measurement of the thermopower might make it worthwhile to perform the calculation and make the comparison.

5.3.3 Unusual Fermi surfaces

Fig. 5.5 depicts the calculated FSs. In spite of the generally 2D band structure, the small k_z dispersion of bands at ε_F make some of the FSs surprisingly three-dimensional. Electron pockets and hole pockets coexist in the Brillouin zone, with electron and hole concentrations necessarily being equal.

Hole surfaces. Four hole “fan-blade” surfaces lie oriented in the xz- and yz-planes. At the center, extending from Γ halfway to Z, lies a long and narrow surface with square cross section. The top view allows the origin of these surfaces to be understood. The cross sections in the xy-plane are of two ellipses that are very anisotropic (in the xy-plane) and at right angels to each other. Each corresponds to a dispersion that is weak in one direction (the long major axis) and strong in the other (minor axis). These bands would intersect, but in fact are intersected by the electron band that cuts a squarish hole (rotated by 45°), within which the elongated hole surface inside re-emerges.

Electron surfaces. In the bottom panels of Fig. 5.5, the squarish electron surface (with k_z variation and resulting holes, shown in the lower two panels of Fig. 5.5) that cuts the aforementioned hole surface is pictured, and substantiates the discussion provided just above. In addition, there are simple electron ellipsoids centered along the Γ-M lines. It is curious that in a band structure that is for the most part strongly 2D, all the FSs have a rather definite three-dimensional character. Although the bands show little dispersion along Γ-Z, the bands just above the the Fermi level are quite different depending on whether $k_z = 0$ or $k_z = \pi$. In particular, the lowest band along R-A is rather flat, but the lowest conduction band along X-M has a dispersion of nearly 2 eV. Similar comparisons can be made for the bands along Γ-X and Z-R. The k_z dispersion is not nearly as strong near $k_x = k_y = 0$, which is clear from both the band structure and the FS.

Short discussion. It was noted in the Sec. 5.1 that the NaAlSi structure is the same as the Fe-pnictide "111" structure. Moreover, in both compounds, the relevant bands involve only the (Si-Al-Si or As-Fe-As) trilayer. The top view of the fan-blade surfaces have characteristics in common with those of some of the Fe pnictides,[143, 144] all of which have this same trilayer. The similarity is that the top view of the fan blades (if one ignores the diamond-shaped cutout at the intersection, centered at Γ) appears to show intersecting FSs, neither of which has the square symmetry of the lattice.

Such occurrence of intersecting FSs, each with lower symmetry than the lattice, has been analyzed for LaFeAsO (a "1111" compound) by Yaresko *et al.* [145]. A symmetry of the Fe_2As_2 (also Al_2Si_2 substructure is a non-primitive translation connecting Fe atoms (respectively, Al atoms) followed by z-reflection. This operation leads to symmetries that allow $k_z = 0$ bands to be unfolded into a larger Brillouin zone (that is, a "smaller unit cell" having only one Fe atom) which *un*folds the band structure and the intersecting FSs. The NaAlSi FSs appear to have this similar crossing (albeit interrupted by

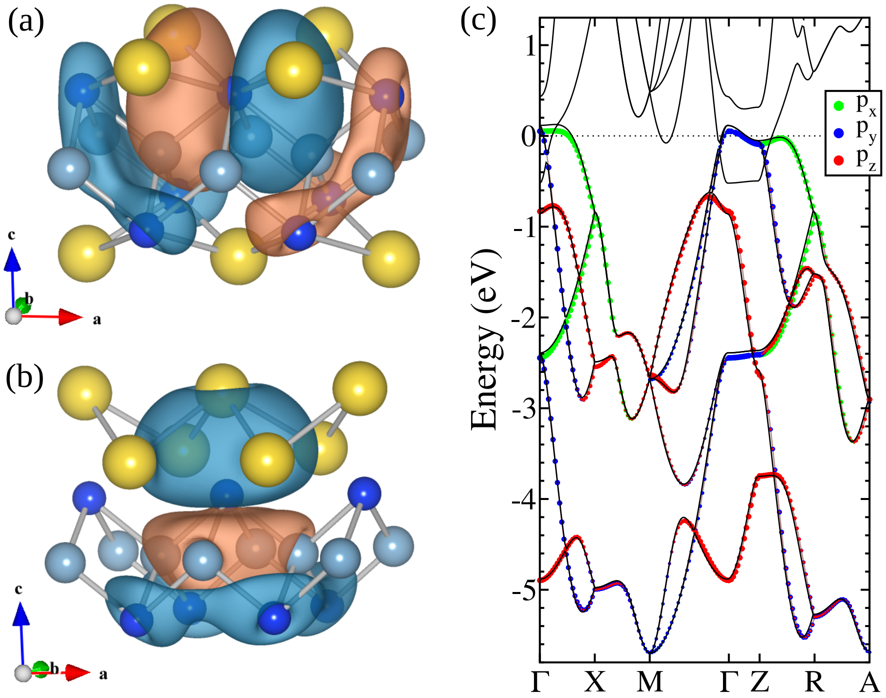

Figure 5.6. Isosurface of the WFs for (a) Si $3p_x$ and (b) Si $3p_z$. Na atoms are large and yellow (light) colored, Si atoms are small and blue (dark) colored. The two colors of the isosurface represent different signs. (c) The tight-binding fatbands band structure described in the text for the WFs, compared to the DFT band structure (black lines).

the free-electron bands), and the highly anisotropic dispersion is due to distinct (but symmetry-related) hopping along each of the crystal axes. In this respect NaAlSi may clarify the electronic structure of the pnictides: by analogy, there are separate bands that disperse more strongly along the $(1, 1)$ direction or the $(1, -1)$ direction, and give rise to the intersecting, symmetry-related surfaces. In NaAlSi the bands are much more anisotropic in the plane (approaching one-dimensional), making such character much clearer. A difference that complicates the analogy is that in the pnictides the bands near ε_F are derived from the Fe atoms, which comprise the center layer of the trilayer, whereas in NaAlSi the bands under discussion are derived from the Si atoms, which comprise the two outer layers.

		p_x	p_y	p_z
a	p_x	761		60
	p_y		-62	60
	p_z	60	60	-40
2a	p_x	128		27
b	p_x	361	300	360
	p_y	300	361	360
	p_z	360	360	360
$\mathbf{b}^*$	p_x	12	5	50
	p_y	5	12	50
	p_z	50	50	185

Table 5.1. Selected hopping integrals in meV for the Si $3p$ WFs along the vectors $\mathbf{a} = (a, 0, 0)$ (hopping within a Si layer), $\mathbf{b} = (a/2, a/2, d)$ (hopping across an Al layer), and $\mathbf{b}^* = (a/2, a/2, c - d)$ (hopping across a Na layer). d is the distance in the z direction between Si atoms above and below Al planes.

5.3.4 Wannier functions

Pictured in Fig. 5.6 are symmetry-projected Wannier functions (WFs) projected onto Si $3p$ orbitals. The extension of the WFs shows considerable involvement from nearby Al and Si atoms, and in addition have some density extending into the Na layers. The p_x WF consists of an atomic p_x function, with its density shifted downward by the bonding contribution of Al sp^3 hybrid orbitals. Beyond the p_x lobes the nearest Si atoms form a bonding lobe that connects to the "small" side of the Al sp^3 function. The large p_x lobes and the extra contribution from nearby Si atoms are responsible for the largest hopping amplitudes shown in Table 5.1, although there is some phase cancellation between the p_x lobe and the lobe lying beyond the nodal surface.

The p_z WF has one lobe extended well into the Na layer; this is responsible for the largest hoppings along $\mathbf{b}^*$ in Table 5.1, and they create the large dispersion in the p_z bands seen in Fig. 5.6(c). Again, the Al atoms contribute with an sp hybrid orbital, although it appears to be more sp^2-like than sp^3-like. There is also a "ring" structure below the Al layer, where an sp hybrid orbital from the Si atoms forms a bonding combination, but it is antibonding with the p_z function on the central Si. The largest

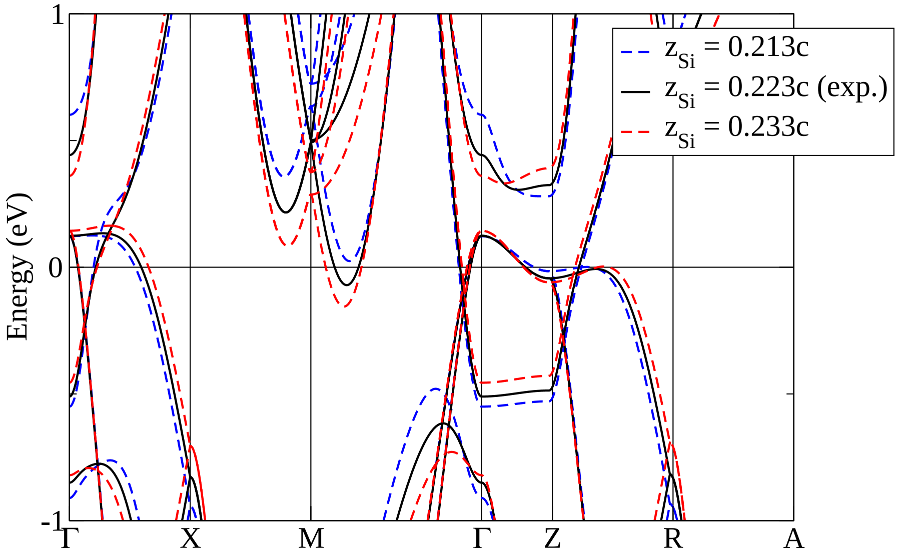

Figure 5.7. Comparison of band structures near ε_F for different z_{Si} values.

contribution to near-neighbor hopping in the Al-Si plane between p_z and p_x or p_z is most likely due to this ring structure, as the p lobes are confined to the inside of a square of near-neighbor Al atoms, which are only edge sharing with the nearest Si atoms along **b** vectors. This is the likely reason that all the hoppings along **b** are approximately of the same magnitude. The dispersion which creates the FSs along Γ-Z (seen in Fig. 5.5) is composed only of the p_x and p_y WFs. This is not caused by the large hoppings, but by smaller hoppings along $\mathbf{b}^*$ between p_x and p_y WFs. Without these small hoppings, the band just above ε_F is dispersionless along Γ-Z.

5.4 Response to changes

5.4.1 Electron-ion coupling

A deformation potential $\mathcal{D}$ is the shift in an energy band with respect to sublattice atomic displacement. One can freeze in phonon modes to calculate deformation potentials, which at the FS are directly connected to electron-phonon matrix elements [146].

Moving the Si atoms in the z direction by ±1% of the experimental parameter, such that the tetrahedra surrounding the Al atoms stretch or flatten (while remaining centered on Al), gives an average deformation potential of ~0.8 eV/Å over five band positions near the Fermi level. The largest shift is for the ellipsoidal electron pockets, with $\mathcal{D} \sim 1.2$

eV/Å. These ellipsoids disappear when the Si atoms are displaced toward the Al plane (see Fig. 5.7).

Flattening the Na bilayer, so as to remove the buckling of the Na atoms, requires a (very large) 12% change in the z component of the Na atoms. We chose such a large displacement because we do not expect a substantial deformation potential for Na movement. Even this large displacement does not alter very much the valence bands, as expected, and the hole FSs remain virtually unchanged. The conduction bands at the Fermi level however shift appreciably, resulting in a modulation of the electron ellipsoids along (1,1) near M. In addition, the accidental four-band near-degeneracy that is 0.5 eV above ε_F at M splits the two separate doubly-degenerate states, opening up a gap of ~0.7 eV, which is equivalent to a deformation potential of ~0.8 eV/Å (but the bands are not at ε_F).

These values of $\mathcal{D}$ are very small when compared to that of the E_{2g} phonon mode in MgB_2, which has a value of 13 eV/Å [35]. The C atom displacements in B-doped diamond ($T_c = 4$ K) give rise to two large deformation potentials of 14 eV/Å and 7 eV/Å [147]. However, these are the largest values known, far larger than in several good superconductors. In Li_2Pt_3B, a superconductor at $T_c = 8$ K, the deformation potential was calculated for Pd motions in the $\langle 011 \rangle$ direction. For about 25 calculated values near the Fermi surface, the mean value was $\mathcal{D} = 1.15$ eV/Å, with values covering a wide range from 0.15–4 eV/Å [148]. Values for motions of the Li atom in this compound were about an order of magnitude smaller. The values we calculate for NaAlSi are comparable to the mean value for Pt motion in Li_2Pt_3B, which is not certain to be phonon-coupled but for which no serious alternative has been suggested. The large variation calculated in Li_2Pt_3B warns against drawing any conclusions from a small sample.

5.4.2 Magnetic susceptibility

When an external magnetic field is applied to a material, its quasiparticle energies shift and magnetic dipole moments are induced. The material's magnetic spin susceptibility χ is the degree to which it can be magnetized in the magnetic field and is given by

$$\chi = \frac{\partial M}{\partial H} = (\partial^2 E/\partial M^2)^{-1}.$$

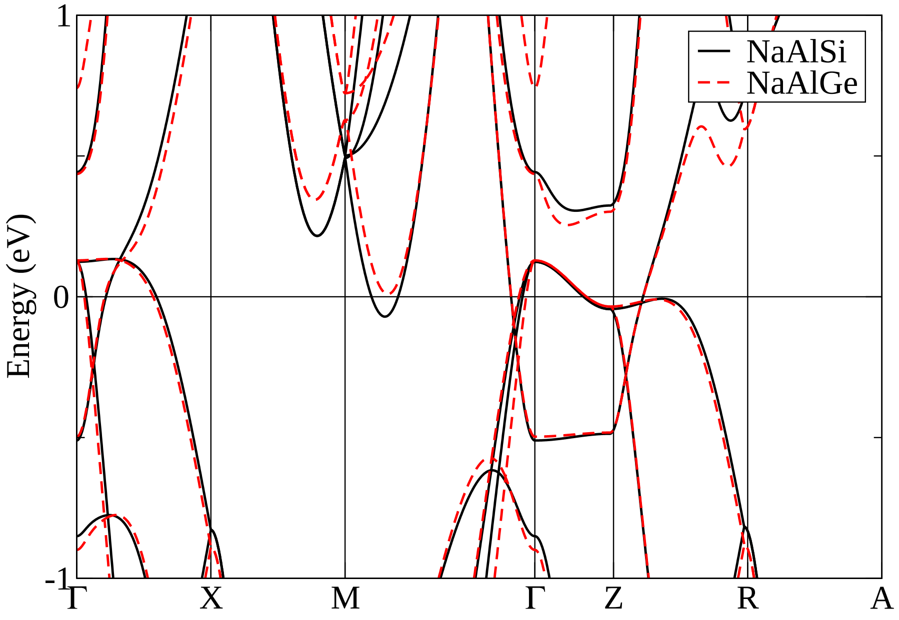

Figure 5.8. Blowup of the band structures of NaAlSi and NaAlGe near ε_F.

where M is the volume density of the magnetic dipole moment (a microscopic current), and H is the external magnetic field (associated with macroscopic currents). Fixed-spin-moment calculations were conducted to produce an energy-vs.-moment $E(M)$ curve, resulting in a susceptibility of $\chi = 1.30\ \mu_{\mathrm{B}}^2\ \mathrm{eV}^{-1}$ (per u.c.). The susceptibility has contributions from electron-electron interactions, but it is related to the noninteracting Pauli susceptibility χ_0, as follows:

$$\chi = \frac{\chi_0}{1 - IN(\varepsilon_F)} = \frac{\mu_B^2 N(\varepsilon_F)}{1 - IN(\varepsilon_F)}. \tag{5.6}$$

I is the Stoner enhancement factor, and the relation $\chi_0 = \mu_B^2 N(\varepsilon_F)$ was used to obtain the last expression. Using the calculated bare Pauli susceptibility $\chi_0 = 1.11\ \mu_{\mathrm{B}}^2\ \mathrm{eV}^{-1}$, exchange-enhancement of the susceptibility is

$$S = \frac{\chi}{\chi_0} = 1.17.$$

A small enhancement of roughly this magnitude (17%) is expected for an *sp* metal; for comparison, Janak [149] obtained the value $S = 1.34$ for Al directly from density functional theory in the $H \to 0$ limit.

5.4.3 Comparison to NaAlGe

Isostructural and isovalent NaAlGe is not superconducting (above 1.6 K, at least), so it should be instructive to compare its electronic structure to that of NaAlSi. Using the experimental lattice and internal parameters of NaAlGe [138], we have calculated its band structure and compared it with that of NaAlSi on a rather fine scale in Fig. 5.8. The band structures are extremely similar near ε_F, the only noticeable difference being that the band along Γ-M near M does not cross ε_F in NaAlGe. The free-electron band is also identical.

Supposing (first) the tiny bit of FS along Γ-M cannot account for the difference in superconducting behaviors, the factors relevant for electron-phonon coupling will be the difference in mass (Ge is more than twice as heavy as Si) and the difference in electronic character, which can affect force constants and electron-phonon matrix elements. Thus electron-phonon coupling that is concentrated in the Si vibrations might be consistent with the decrease (or disappearance) of T_c. However, an electron-phonon coupled semimetal with $T_c = 7$ K would be remarkable.

Another possibility, especially considering the low energy electronic behavior to be expected in a two dimensional compensated semimetal with low carrier density, is that the pairing mechanism is electronic rather than phononic. In three dimensions purely electronic pairing mechanisms have attracted serious study (albeit in the homogeneous electron gas approximation, by Sham and collaborators [150, 151] for example). However, 2D semimetals introduce new features that deserve detailed study, such as the 2D plasmon that goes to zero as $\sqrt{q}$. A model in which the electronic response of a 2D electronic superlattice plays a central role in the mechanism has been previously studied [152, 153] using a model of parallel conducting sheets separated by a dielectric spacer. This model may be useful as a starting point for understanding NaAlSi, with or without phonon processes.

Another possibility is that the small FS pockets are important. In the scenario that superconductivity arises from an enhancement of electron-phonon coupling, it would require a new and unusual contribution of a small density of additional electrons with non-adiabatic coupling to phonons. These tiny pockets will contribute additional low frequency electronic response as well, including low frequency plasma oscillations, intervalley electron-hole polarization at large momentum, and additional interband transitions. As noted in the Introduction, NaAlSi adds another low carrier density, two dimensional system to the list of unusual and unexplained superconductors, and it may be especially useful for further study specifically for the reason that it does not contain any transition metal.

5.5 Concluding Remarks

The classes of materials that contain relatively high temperature superconductors [154] continues to expand. Superconductors derived from doped 2D semiconductors pose many of the most interesting issues in superconductivity today. The cuprates and the Fe-pnictides (and -chalcogenides) are strongly magnetic, and comprise one end of the spectrum (though they are themselves quite different). On the other end lie those with little, perhaps negligible, magnetism: electron-doped ZrNCl and HfNCl, and electron-doped TiNCl. There are several other, lower-T_c systems, whose behavior seems different still (hydrated Na_xCoO_2, $Li_{1-x}NbO_2$, and several transition-metal disulfides and diselenides).

A common feature of most of these systems is that they have strong 2D features and have a small, but not tiny (as in superconducting doped $SrTiO_3$), concentration of charge carriers, often in the range of 0.05–0.15 carriers per unit cell (u.c.). These materials also have ionic character, although in the Fe pnictides and NaAlSi the ionic character is not easily quantified. NaAlSi differs from the other mentioned superconductors in that it has *sp* carriers—the others have carriers in *d* bands—and it is self-doped, being a compensated semimetal. Our results suggest that a useful view of NaAlSi is that it be regarded as arising from an underlying ionic semiconductor, but that it has a small *negative* gap rather than a true gap. Without the overlap of the valence and conduction bands, it would be a 2D, partially ionic, partially covalent semiconductor like the aforementioned nitridochloride compounds, which superconduct in the 15–25 K range. Comparing the characteristics of these two classes of superconductors should further the understanding of 2D superconductivity.

A further distinction of NaAlSi is that, in spite of a strongly 2D band structure overall, the small k_z dispersion of the doubly degenerate band at the Fermi level gives three dimensional Fermi surfaces. One of these two bands also has extremely strong anisotropy within the 2D plane, especially for a compound with tetragonal symmetry, which further serves to produce intricate Fermi surfaces and contributes to the peculiar peak in the density of states at ε_F.

In summary, NaAlSi contains a number of peculiarities compared to related superconductors with strongly layered structure, and it seems certain that the pairing mechanism, whether phononic or electronic, will require an increase in understanding of the relatively low energy electronic behavior in this compensated semimetal. Further study of this compound should help to generalize our understanding of superconductivity in low density, layered materials.

5.6 Acknowledgments

This work was supported by DOE grant DE-FG02-04ER46111, the Strategic Sciences Academic Alliance Program under grant DE-FG03-03NA00071, and by DOE SciDAC Grant No. DE-FC02-06ER25794.

Chapter 6

Determining the Structure of Superconducting CaLi$_2$

This work was done in collaboration with W. J. Evans and H. Cynn of Lawrence Livermore National Laboratory and W. E. Pickett and R. T. Scalettar of UC Davis.

6.1 Introduction

Hexagonal CaLi$_2$, though not known to superconduct at ambient pressure, has been reported to exhibit superconductivity at high pressures, its transition temperature reaching as high as 13 K near 40 GPa [13, 14]. This discovery came shortly after Feng *et al.* theorized the possibility of superconductivity for the system [62].

It is natural to look for superconductivity in CaLi$_2$, as Ca and Li each possess a high superconducting transition temperature, and CaLi$_2$ is the sole intermetallic compound at ambient pressure between the two elements. A maximum superconducting transition temperature of 14 K at 30 GPa has been observed in Li [5], and Ca, though not known superconductor at ambient pressure, has the highest T_c of all elements—25 K at 160 GPa [60]. Ca and Li are simple, free electron-like metals at ambient pressure, yet they are both easily compressible, allowing room for radical changes in their electronic properties under pressure. As pressure is increased, the overlapping of ionic cores in CaLi$_2$ causes the conduction electrons to be pushed out to interstitial sites—a phenomenon observed in elemental Li [155]—forming a low-valence charge distribution between the nearest Li-Li neighbors. This results in lower symmetry and a drastic departure from the nearly free electron model to one closer to that of a d-electron metal. Contradictory to these observations, however, the bandwidth of CaLi2 decreases upon pressurization [62]. Our interest in $CaLi_2$ derives from such anomalous characteristics, and yet we may also find some familiar features in the material stemming from those same anomalies. For example, the redistribution of valence electrons in the system suggests regions of electron-phonon interaction equivalent to the B planes in MgB_2.

What with Li having a maximum T_c that is similar to—and that is occuring around the same pressure as—$CaLi_2$, it cannot be ruled out that the compound segregates into its elemental components at higher pressures, allowing for Li to superconduct. Debessai *et al.* conducted x-ray diffraction on $CaLi_2$ up to 54 GPa, and showed a gradual structural phase transition above 23 GPa to an orthorhombic structure [13]. No dissociation of the compound was observed. These measurements however were done at 150 K, not in the superconducting temperature range. tse-cali2 *et al.* also examined the structure of $CaLi_2$, with contrary results to those of Debessai's group; they observed an increasing amount of Ca and decreasing amount of $CaLi_2$ starting at 14 GPa, suggesting the possibility of dissociation [63]. They support this with enthalpy calculations that are in agreement with their experimental observation. But again, this investigation was done at room temperature and up to only 20 GPa. Lastly, Xie *et al.*'s enthalpy calculations predict dissociation at pressures 20–35 GPa, but the elements recombine into a monoclinic structure for $P = 54$–105 GPa [64].

In our study, high pressure XRD measurements in a diamond anvil cell were performed at varying low temperatures in order to ascertain the structure of $CaLi_2$ in the superconducting phase and beyond. At 10 K, our results show a structural distortion beginning at 24 GPa, and no elemental dissociation, agreeing more so with the findings of Debessai.

6.2 Experimental Procedure

Our $CaLi_2$ sample was synthesized by D. P. Young and A. B. Karki of Lousiana State University, by placing stoichiometric amounts of Ca and Li metal in an aluminum oxide crucible and melting them together in a radio-frequency induction furnace under an atmosphere of ultra high purity argon gas. The temperature was slowly raised to 900

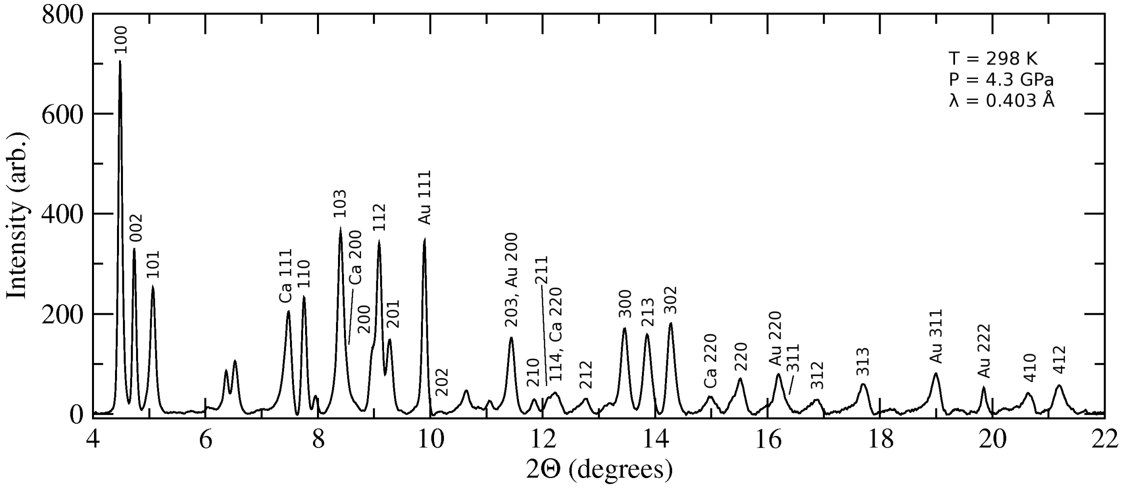

Figure 6.1. XRD pattern of CaLi$_2$ at 298 K and 4.3 GPa. Unmarked peaks are from unknown impurities.

°C, until both metals melted together. The furnace was maintained an additional 10–15 minutes and shut off. The sample was then removed and immediately sealed in a quartz tube under vacuum to prevent oxidation.

Angle-dispersed XRD was carried out using a membrane DAC at the HPCAT beamline (ID-B) of the Advanced Photon Source. The x-ray beam had a diameter of 10 μm and an energy of 31 keV. Brilliant-cut diamonds with 0.3 mm flats and a Re gasket were employed in the DAC. The brittle CaLi$_2$ was broken up, and the powder was loaded into the DAC in an argon glove box to prevent oxidation. There was no pressure medium, and gold was used as an internal pressure sensor. To lower the sample temperature, the DAC was inserted in a CRYO Industries He gas-flow cryostat. Temperatures as low as 10 K and pressures as high as 38 GPa were achieved. The XRD patterns were recorded onto a MAR 345 image plate detector, and the Debye-Scherrer images were integrated by the FIT2D software to produce the diffraction patterns, which were subsequently analyzed using the program XRDA [156].

6.3 Results

XRD measurements were done in the temperature range of 9–298 K and up to 50 GPa in pressures. Fig. 6.3 shows the pattern of CaLi$_2$ at room temperature and 4.3 GPa, and confirms the MgZn$_2$-type Laves structure. At this pressure, the lattice parameters are

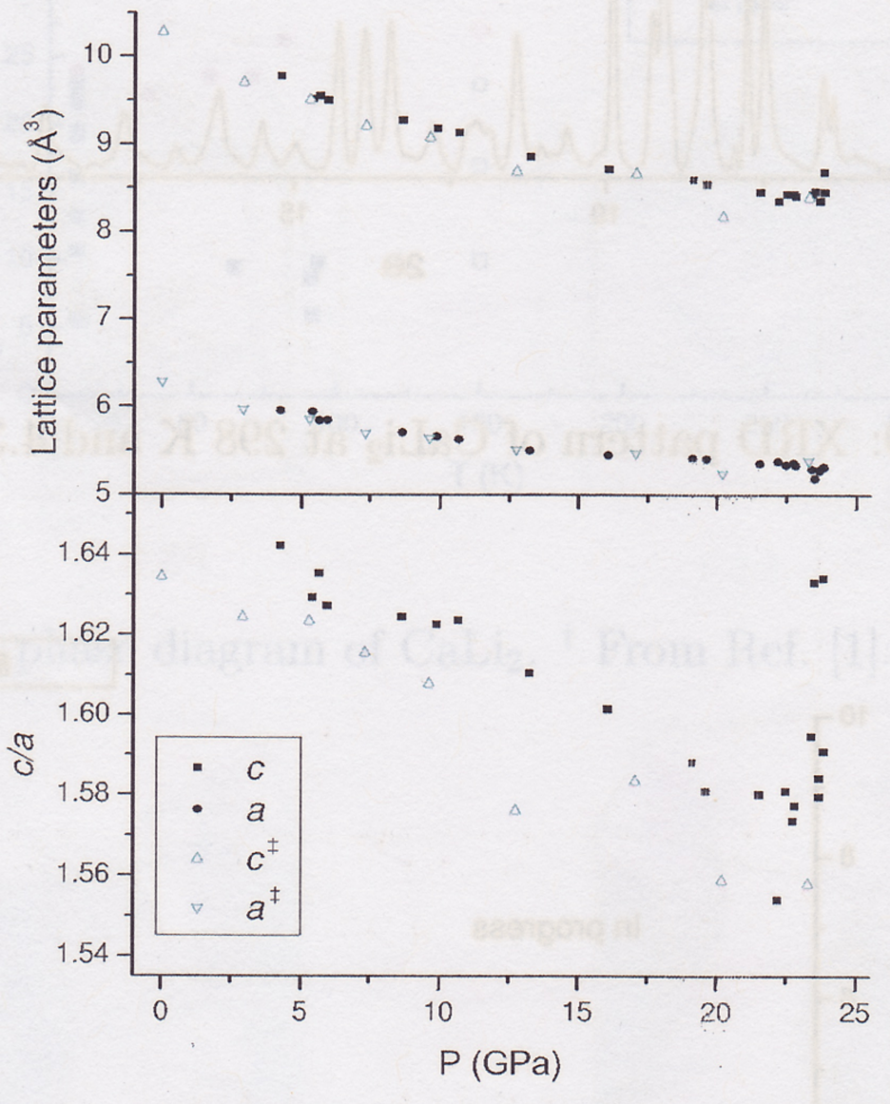

Figure 6.2. Lattice parameters c and a vs. pressure of CaLi$_2$. Our data is overlayed with Debessai's (‡Ref. [13]). [Note: This figure will be replaced!]

$a = 5.9504$ Å and $c = 9.6717$ Å which match well with the equations of state published in Ref. 13 (see Fig. 6.3 for a comparison). The unassigned peaks are unknown but speculated to be due to oxidized impurity phases. A significant amount of FCC Ca is apparent, but it does not increase or decrease as pressure is raised.

In Fig. 6.3, XRD patterns at 10 K and different pressures have been selected. The cryostat has a beryllium window through which the x-rays pass, which creates unwanted diffraction patterns. The size of the window also limits the extent of the diffraction angle 2Θ, making it all the more difficult to determine the structure. The HCP structure

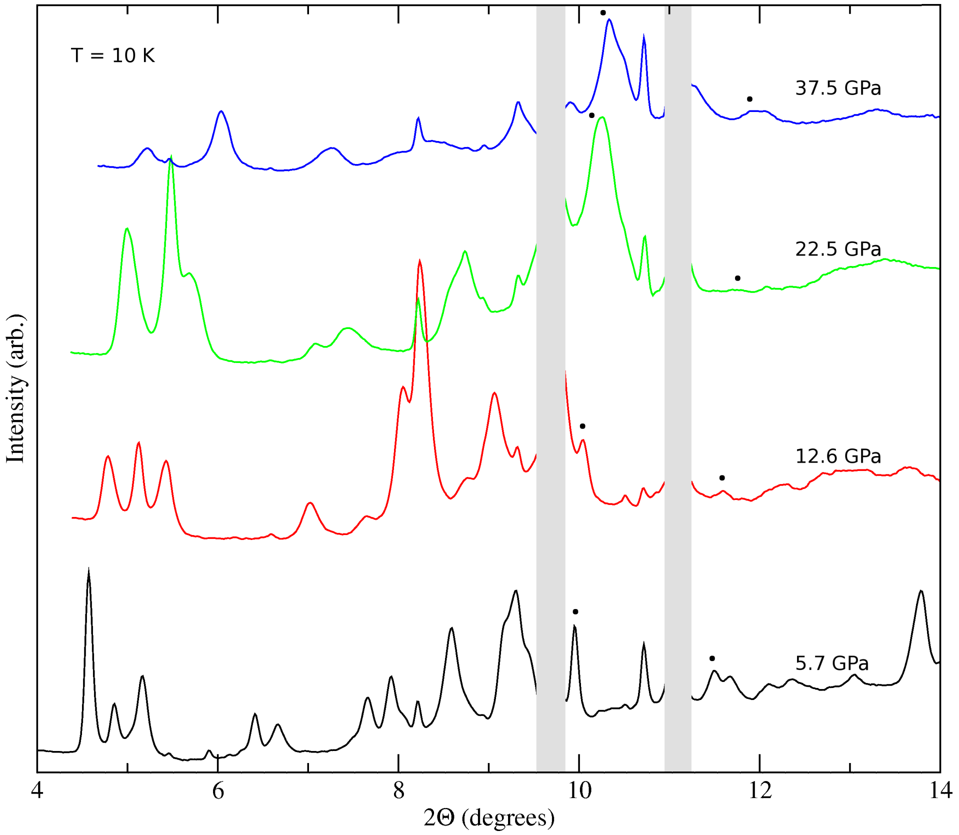

Figure 6.3. XRD patterns for CaLi$_2$ at 10 K and various pressures. Black dots indicate Au peaks below. Gray bars cover peaks diffracted by the Be window of the cryostat. The bottom three plots fit the HCP structure nicely; the top-most pattern is distorted from HCP.

remains stable up to 24 GPa, at which point peak refinement becomes difficult. Upon further compression, the structure strays even further away from the original HCP. Our pattern at 37.5 GPa and 10 K is not unlike Debessai's at 35 GPa at 150 K, but whether this new structure is orthogonal, monoclinic, or, as Feng has considered, an elongation or compression in only one lattice direction [62] is unclear. According to ac susceptibility measurements performed on CaLi$_2$ [13], our sample should be in the superconducting regime for the top XRD plot in Fig. 6.3. There is no evidence of increased elemental Ca there.

Fig. 6.3 is the pressure-vs.-temperature phase diagram for CaLi$_2$. Included are all of our results from this experiment and the results of Debessai as well as Matsuoka. As shown, the hexagonal structure is stable for all low pressures, regardless of temperature. Whether $T = 10$ K or 150 K, deviation from HCP occurs around the same pressure of 24

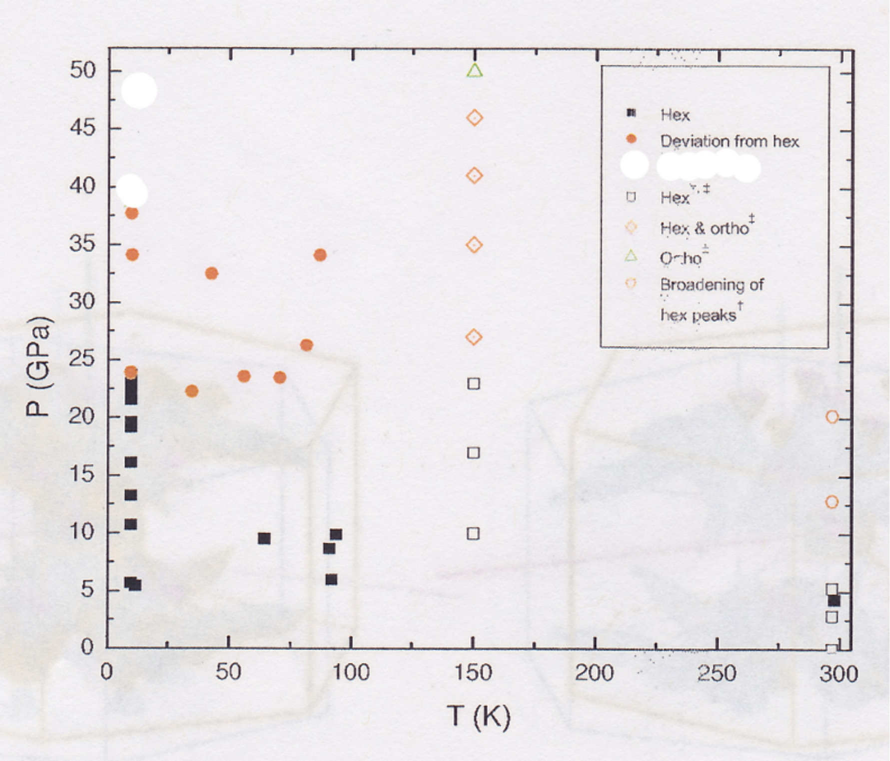

Figure 6.4. The structural phases of $CaLi_2$ (†Ref. [14]. ‡Ref. [13]. [Note: This figure will be replaced!]

GPa. More experiments need to be done in order to conclusively determine the structure when $CaLi_2$ is superconducting.

6.4 Conclusion

In summary, our research on $CaLi_2$ shows that elemental decomposition is unlikely in the superconducting regime, but a gradual phase transition to an as-of-yet unknown structure does occur. Seeing as how our data match well with what is reported in Ref. [13], it is likely the superconductor is orthorhombic.

Chapter 7

PuPt_2In_7: A Computational and Experimental Investigation

This work was done in collaboration with F. Ronning, J. X. Zhu, E. D. Bauer, J. N. Mitchell, P. H. Tobash, B. L. Scott, and J. D. Thompson of Los Alamos National Laboratory, Y. Jiang and C. H. Booth of Lawrence Berkeley National Laboratory, and W. E. Pickett of UC Davis.

7.1 Introduction

Magnetically mediated superconductivity in heavy-electron systems, specifically Ce and U compounds, has been known to exist for over 30 years [29, 53, 54, 157]. Among the known heavy fermion superconductors a particularly rich family include the 115, 127, and 218 structures which are all variants of the '103' parent compound, crystallizing in the $\text{Ho}_m\text{Co}_n\text{Ga}_{3m+2n}$ architecture (see Fig. 7.1) [158]. Many of these are known to be superconducting [30, 56, 159–166]. It is widely expected that in these systems, spin fluctuations are what bind the Cooper pairs together, and the balance between these local-moment fluctuations and long-range magnetism toward a quantum critical point is crucial for superconductivity to take place. There are however compounds that structurally belong in this family but don't superconduct, as they tend to shy away from this ideal balance. For example, the f electrons in the U-115s, -218s, and the Np-115s are too itinerant to exhibit superconductivity [167–172], and in AmCoGa_5 they are too localized [173, 174]. CeRhIn_5, CePt_2In_7, and Ce_2RhIn_8, all nonsuperconducting anti-

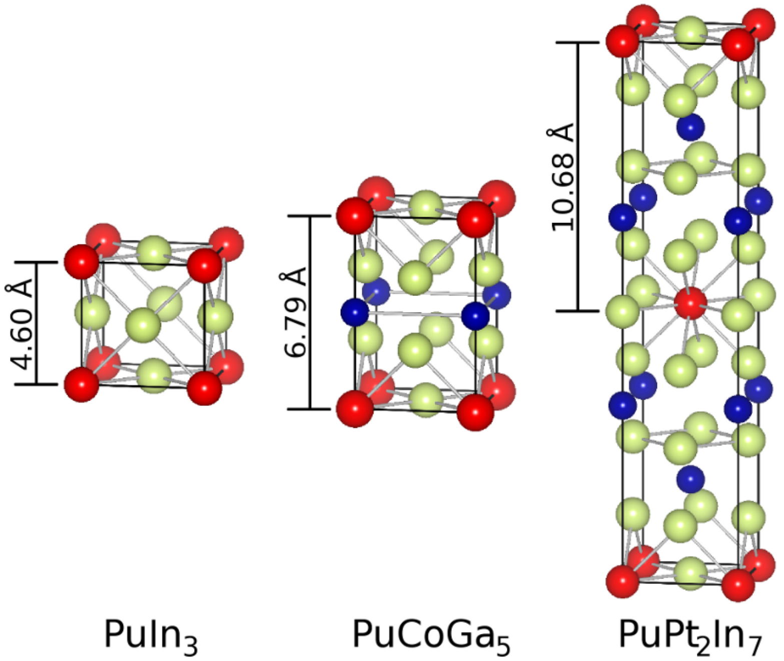

Figure 7.1. Crystal structures obtained using VESTA [12] of some Pu-based compounds. The Pu atoms are colored red, Pt/Co atoms dark blue, and In/Ga atoms light green.

ferromagnets at ambient pressure, require compression to delocalize the f electrons and make them available for electron-electron pairing [159, 165, 175]. Pu-based compounds are particularly interesting, because within the actinides it is the Pu that straddles the line between bearing localized and itinerant $5f$ electron states.

Pu compounds are often considered the hole analog of their Ce counterparts, for having five f electrons in the $5f_{5/2}$ spin-orbit split multiplet. In fact, the two 115 subgroups manifest very similar behaviors from their Curie–Weiss-like magnetic susceptibilities [159, 163, 176, 177] to their quasi-two-dimensional Fermi surfaces (FSs) [178–180]. The indide members show remarkably similar properties as well: PuIn$_3$ is a 14 K antiferromagnet [181], while CeIn$_3$ is a 10 K antiferromagnet [30], and PuCoIn$_5$ and CeCoIn$_5$ are both 2 K superconductors [160, 166]. Why the T_c's of the PuCoGa$_5$ and PuRhGa$_5$ superconductors are so much higher however remains elusive.

Based on the impressive list of superconductors discovered in the past 25 years with 2D structures and properties, a guideline can be made that more 2D structures are more favorable for superconductivity and will therefore give rise to a higher T_c. The average spin fluctuation frequency is higher in quasi-2D systems than 3D, and this brings about a larger Cooper pairing energy [3]. Indeed, the $\mathrm{PuRh_{1-x}Co_xGa_5}$ ($0 \leq x \leq 1$) compounds follow a linear relation in T_c vs. axial ratio c/a [182], which is also observed in $\mathrm{Ce}M\mathrm{In_5}$ (and, interestingly, with an almost identical slope to its Pu-based cousins') [177, 183]. Recently, $\mathrm{CePt_2In_7}$—a structurally and electronically more 2D version of 115—was discovered [165, 184]. Although T_c was not enhanced, it did achieve a maximum superconducting transition temperature of 2.1 K, comparable to the other Ce-based 115s'.

In this chapter, we report the discovery of the Pu analog to $\mathrm{CePt_2In_7}$. We find $\mathrm{PuPt_2In_7}$ is a mass enhanced paramagnet which lacks superconductivity down to 2 K. We report electronic structure calculations on $\mathrm{PuPt_2In_7}$, including densities of states, band structures, and Fermi surfaces. We present also analogous analyses on isovalent $\mathrm{PuPt_2Ga_7}$, which has yet to be synthesized. In addition, we have calculated the constant-matrix-element noninteracting magnetic susceptibilities of $\mathrm{PuPt_2In_7}$ and $\mathrm{PuPt_2Ga_7}$, as well as $\mathrm{PuCoGa_5}$ and $\mathrm{PuCoIn_5}$ as points of comparison. While the Fermi surfaces of the 127 compounds is qualitatively distinct from the 115s', all four Pu compounds exhibit a row of peaks in the susceptibility at $q_x = q_y = 0.5$. We discuss the possible implication of these results for understanding Pu superconductivity.

7.2 Experiment

Single crystals of $\mathrm{PuPt_2In_7}$ were grown by the self flux method from the respective elements with an excess of In metal. The reactions were loaded in the ratio Pu:Pt:In (1:4:30) using 2 $\mathrm{cm^3}$ alumina crucibles which were sealed under vacuum in quartz ampoules. The isolated single crystals crystallized with a plate-like habit and were found to be $\mathrm{PuPt_2In_7}$ based on single crystal X-ray diffraction analysis. The single crystal X-ray data was collected on a Bruker D8 equipped with a APEX2 CCD detector. Full spheres of data were collected at room temperature and the collections were handled in batch runs at different ω and ϕ angles. The structure was refined using the atomic coordinates from the isostructural $\mathrm{CePt_2In_7}$ compound. The data integration and refinement procedures were completed using SAINT-Plus, SHELXS97, and SHELXL97 programs. $\mathrm{PuPt_2In_7}$ stabilizes into a body-centered tetragonal structure (see Fig. 7.1, Table 7.2).

Space group	$I4/mmm$
a (Å)	4.5575(7)
b (Å)	4.5575(7)
c (Å)	21.362(6)
Volume (Å^3)	443.71(16)
Formula units/cell	$Z = 2$

Atom	x	y	z
Pu	0	0	0
Pt	0	0	0.32626(6)
In1	0	0	0.5
In2	0	0.5	0.2500
In3	0	0.5	0.10597(11)

Table 7.1. Table of structural parameters and atomic positions for $\mathrm{PuPt_2In_7}$ determined from single crystal X-ray diffraction.

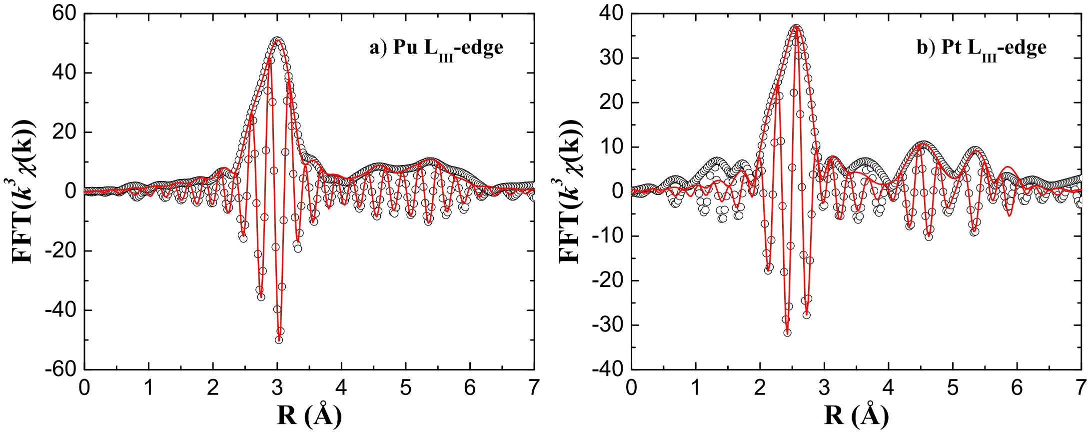

Figure 7.2. Fast Fourier Transformed r-space data (open symbol) and the fit (solid line) for a) Pu L_{III}-edge and b) Pt L_{III}-edge. Both EXAFS data were measured at $T = 30$ K, with the FT k range of 3.5–13.5 Å^{-1} and the Gaussian window of 0.3 Å^{-1}. The r-space fit range is 2.1–5.4 Å for both edges. Here only the real part, Re, and the amplitude, $\sqrt{\mathrm{Re}^2 + \mathrm{Im}^2}$, of $\mathrm{FFT}(k^3\chi(k))$ were plotted.

While in $\mathrm{PuCoGa_5}$ the $\mathrm{PuGa_3}$ layer and $\mathrm{CoGa_2}$ layer stack alternately, $\mathrm{PuPt_2In_7}$ has two layers of $\mathrm{PtIn_2}$ for each $\mathrm{PuIn_3}$.

To understand the local structure of $\mathrm{PuPt_2In_7}$, fluorescence x-ray absorption fine

	N	σ^2 (Å^2)	R (Å)	σ^2_{static} (Å^2)	θ_{cD} (T)
Pu-In(3)/In(1)	12	0.002(3)	3.224(4)	0.0001(1)	211(2)
Pu-Pu	4	0.004(2)	4.567	0.0015(5)	145(9)
Pu-Pt	8	0.005(3)	4.925	0.0039(4)	238(15)
Pt-In(3)/In(2)	8	0.0003(2)	2.745(6)	-0.0003(5)	266(29)
Pt-In(1)	1	0.0003	3.702	0.0009(18)	408(368)
Pt-Pt	8	0.0006(5)	4.561	-0.0001(8)	255(33)
site-interchange	Pu/In(1)	Pu/In(2)	Pu/In(3)	Pu/Pt	Pt/In(1)
fraction (%)	6±4	15±6	0±4	3±5	18±21

Table 7.2. EXAFS fit results for the Pu and Pt L_{III}-edges on PuPt$_2$In$_7$. Fit and FT ranges are listed in the caption of Fig. 7.2. Though we only show single-scattering peaks shorter than 5.0 Å, all single- and multiple-scattering peaks within the fit range are included. To obtain a better estimate of the contribution from the farther atoms in the fit range, the single-scattering peaks between 5.4 and 6.0 Å are also included in the fit and are held together with one single σ^2. Coordination numbers N are held fixed to the nominal structure. A small vibration of the lattice is allowed by constraining the shifts of all longer bonds to the shortest bonds and keep the shortest ones free to move. In addition, in the Pt edge fit, the Pt-Pu pairs at ∼4.92 Å are fixed to the Pu-Pt pairs with the same R, and σ^2 to reduce the fitting parameter. S_0^2, ΔE, and the fit quality are 0.90(1), $-10.0(1)$ eV, and 7.6% for the Pu edge, respectively, and 0.90(1), $-8.1(15)$ eV, and 18.20% for the Pt edge. (Note that the bad fit quality for the Pt edge fit and large uncertainty in the correlated Debye fit for the Pt-In(1) pair are caused by the background oscillation around 3.5 Å.) The number of free parameters in the fits are 14 for the Pu and 15 for the Pt edge, far below the number of independent data points as given by Stern's rule [15], which is ∼23 for both fits. The fraction of ion/ion site interchange are shown in units of percentage.

structure (XAFS) data were collected at the Stanford Synchrotron Radiation Lightsource (SSRL) on the Pu and Pt L_{III}-edges at beamline 11-2, using a half-tuned double crystal Si(220) monochromator, with a slit height of 0.6 mm and 0.5 mm for the measurement of each edge, respectively. A six-month old crystal sample was triply contained in a sample holder with Kapton mylar, and was 45° to the incident X-ray beam. 3 scans were collected for each edge at T = 30, 100, 200 and 300 K with a temperature deviation of less than 0.2 K. The self-absorption corrected XAFS data are reduced using standard procedures outlined in Refs. 185 and 186, including fitting an embedded-atom absorption function $\mu_0(E)$ using a 7-knot cubic spline function with a maximum photoelectron wave vector k of 15 Å^{-1}. The XAFS function is then defined as $\mu(k)/\mu_0(k)-1$, where μ is the absorption coefficient, $k=\sqrt{(2m_e/\hbar^2)(E-E_0)}$ is the photoelectron wave vector, m_e is the electron rest mass, E is the incident energy, and E_0 is the absorption edge threshold energy, which is defined arbitrarily to be the half height of the edge and allowed to vary in the fit.

k^3-weighted EXAFS data, $k^3\chi(k)$, are fast Fourier transformed (FFT) to r space (FFT($k^3\chi(k)$)), with the FFT range of k = 3.5–13.5 Å^{-1} and Gaussian window of 0.3 Å^{-1}, for both Pu and Pt edges. The r-space EXAFS data are then fit with theoretical *FEFF* functions calculated based on the $I4/mmm$ lattice structure. The r-space data versus fit are shown in Fig. 7.2; the Debye-Waller factors, $\sigma^2(T)$, for some atom pairs ($<$ 5 Å) are fit to the correlated Debye model [187] to obtain the static distortion, σ^2_{stat}, and the correlated Debye temperature, θ_{cD} (shown in Table 7.2). The Pu occupancy ($\sim$98±16%) is estimated by allowing the amplitude of the Pu-Pu peak (4.56 Å) to vary in the Pu edge fit, though the fit quality doesn't change from the previous fit, which assumes 100% Pu occupancy. By arbitrarily constraining $\sigma^2_{stat} \geq 0$ for the Pu-Pu pair, the Pu occupancy is estimated to be $>$ 83%. Possible ion/ion site interchange, such as Pu to In(1,2,3), and Pt to In(1), are also examined using a similar method as in Ref. 188. From these fits, the percentage of Pu site-interchange with other ions, shown in lower part of Table 7.2, is estimated to be close to zero within a small error. Hence, the fit results indicate well ordered local lattice structure around both Pu and Pt ions.

Specific heat data is shown in Fig. 7.3. A fit of the data to $C/T=\gamma+\beta T^2$ between 7 and 13 K gives an enhanced Sommerfeld coefficient of 250 mJ/mol K^2 and β = 3.67 mJ/mol K^4. Using the formula $\Theta_D=(12/5*\pi^4 nk_B)^{1/3}\beta$—where k_B is the Boltzmann constant and n, the number of atoms per formula unit, is equal to 10—we get a Debye temperature, Θ_D = 174 K. The sommerfeld coefficient is larger than that of PuCoGa_5 ($\gamma \simeq$ 100 mJ/mol K^2). Thus the value of γ for PuPt_2In_7 likely represents a reduction in the characteristic spin fluctuation temperature of PuPt_2In_7 relative to PuCoGa_5. At temperatures below 7 K, a small hump is seen in the specific heat which may represent short range correlations. Susceptibility measurements down to 2 K (see Fig. 7.4) have no evidence for superconductivity or long ranged magnetic order.

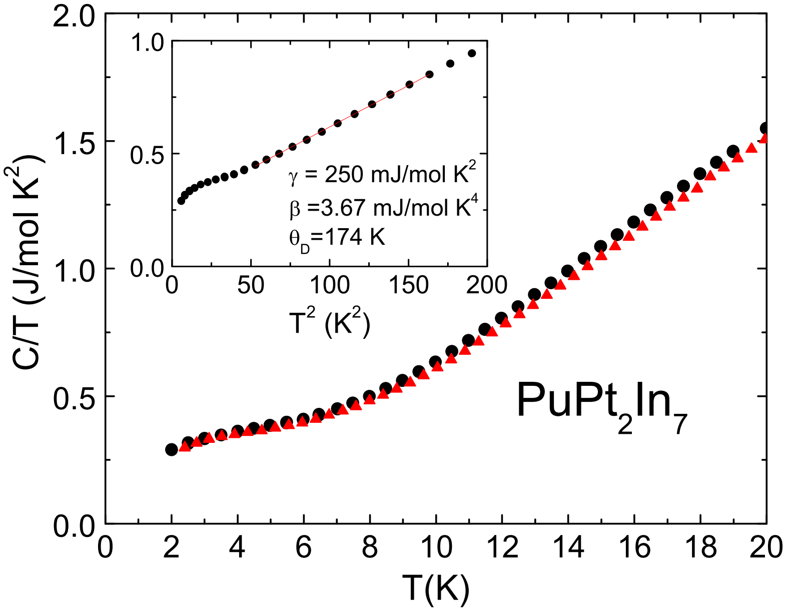

Figure 7.3. (Color online) Specific heat data (C/T) vs. temperature of PuPt$_2$In$_7$, taken in zero field (black circles) and 6 T (red triangles). Inset shows the data plotted vs. T^2 along with a linear fit between 7 and 13 K, from which estimates of the Sommerfeld coefficient and Debye temperature were obtained.

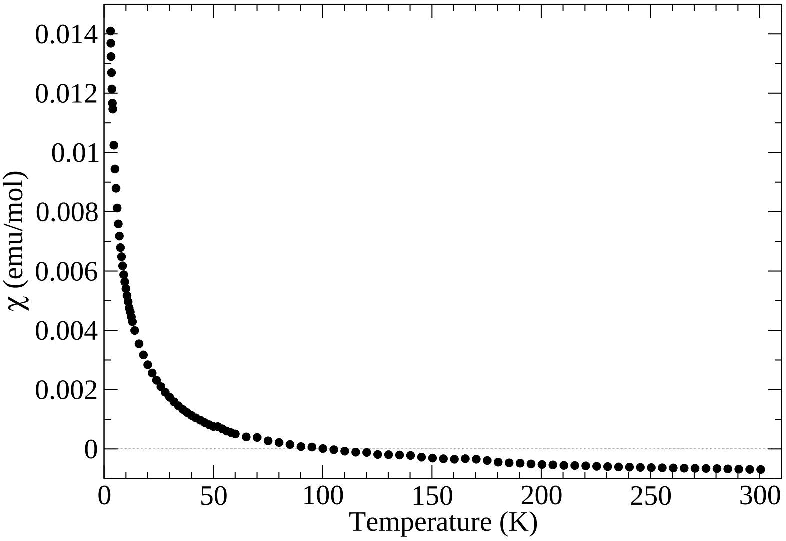

Figure 7.4. Susceptibility of PuPt$_2$In$_7$ at 5 T.

7.3 Computational Results

Electronic structure calculations using the generalized gradient approximation (GGA) within density functional theory were carried out with WIEN2k [92], which employs full-potential linearized augmented planewaves and local orbitals. We adopted the Perdew-Burke-Ernzerhof [85] exchange-correlation potential based on the generalized gradient approximation, and we included spin-orbit (SO) interactions through a second variational method. We performed calculations with and without the Hubbard U (using the around mean field double-counting correction [189]) and exchange J; we used the widely accepted values of $U = 3$–4 eV, $J = 0.6$ eV for Pu [170, 190–193].

The experimental lattice parameters of $PuPt_2In_7$ were used. They were also used to estimate the size of the hypothetical compound $PuPt_2Ga_7$, by means of extrapolating the lattice differences of $PuCoGa_5$ (Ref. 56) and $PuCoIn_5$ (Ref. 166). The inferred lattice parameters for $PuPt_2Ga_7$ are thus $a = 4.22$ Å and $c = 19.51$ Å. The same internal parameters for $PuPt_2In_7$ were used for $PuPt_2Ga_7$.

Paramagnetic (PM), ferromagnetic (FM), and two different antiferromagnetic (AFM) calculations were performed for both $PuPt_2In_7$ and $PuPt_2Ga_7$, and the relative energies are listed in Table 7.3. AFM I represents a configuration in which the antiferromagnetic $\mathbf{q}$-vector is $(1/2, 1/2, 0)$, and AFM II has a wavevector of $(0, 0, 1/2)$. In the GGA scheme, the ground-state configuration of $PuPt_2In_7$ is AFM I, but the FM and AFM II systems become more stable when U is set to 3 eV. At 4 eV, the AFM II configuration has the lowest energy, with the FM state just 2 meV higher. Regardless of the value of U, the energy of PM $PuPt_2In_7$ stays far above those of the other magnetic configurations—a contrast from experimental observations. Even though the AMF double-counting method was implemented specifically for its suppression of magnetism [95], and has correctly predicted the nonmagnetic ground state for δ-Pu, $PuCoGa_5$, and the Pu-218s [170, 178, 194] when no other double-counting approach has been successful, it fails to have the same effect on $PuPt_2In_7$. A reason for this may be that the distance between the Pu atom and its nearest neighbor is greater in $PuPt_2In_7$ (3.2 Å) than the other compounds (it is 3.0 Å for $PuCoGa_5$, 2.5 Å for Pu_2CoGa_8, and 2.6 Å for Pu_2RhGa_8; δ-Pu does not have a ligand but the Pu-Pu distance is 3.1Å), which would provide more room for larger local moments.

$PuPt_2Ga_7$'s energies at $U = 0$ are not unlike $PuPt_2In_7$'s, but when U is turned on, competition for the ground state is not between FM and AFM II but the two antiferromagnetic flavors. It is likely that $PuPt_2Ga_7$ will also be a paramagnet but with a

Table 7.3. Relative total energies (in eV) from GGA and GGA+U calculations of different magnetic configurations of the Pu-127s. The AFM I configuration has a **q**-vector of $(1/2, 1/2, 0)$, AFM II has one of $(0, 0, 1/2)$. $J = 0.6$ eV for all $U \neq 0$ calculations.

		PM	FM	AFM I	AFM II
$PuPt_2In_7$	$U = 0$ eV	+1.15	+0.09	0.00	+0.09
	$U = 3$ eV	+0.57	0.00	+0.01	0.00
	$U = 4$ eV	+0.17	+0.002	+0.04	0.00
$PuPt_2Ga_7$	$U = 0$ eV	+0.93	+0.10	0.00	+0.11
	$U = 3$ eV	+0.41	+0.03	0.00	+0.001
	$U = 4$ eV	+0.06	+0.06	+0.01	0.00

local-moment arrangement that is weaker and qualitatively different.

7.4 Electronic structure

Fig. 7.5 shows the calculated density of states (DOS) of paramagnetic $PuPt_2In_7$ from a GGA calculation without the Coulomb U, and that from a GGA+U calculation ($U = 3$ eV and $J = 0.6$ eV are used for any GGA+U calculation mentioned henceforth). In both pictures, the Pt manifold, predominantly $5d$ in character in the region shown, ends near the -2 eV mark and is fully occupied; such is the general case for $4d$ and $5d$ metals in the 115s and 218s. In the GGA case, the two large Pu peaks correspond to the $5f_{5/2}$, $5f_{7/2}$ SO splitting. The peaks are separated by roughly 1 eV, which is the expected splitting level for Pu compounds.

With the addition of U, the Pu peaks each split into multiple smaller peaks. The left-hand peak broadens to span a range of 1.5 eV; the other peak shifts 0.8 eV to the right and creates a trail of f character up to above 4 eV. The Pu bands widen as a result of the on-site Coulomb repulsion and exchange interaction J. The DOS at ε_F is $N(0) = 6.32$ eV^{-1} (down from the GGA DOS of 9.07 eV^{-1}), which gives a noninteracting electronic specific heat coefficient of 15 mJ/mol-K^2. Comparison with the experimentally measured Sommerfeld coefficient of 250 mJ/mol K^2 gives a mass renormalization of ∼10, which cannot be captured by our static mean-field calculations. Dynamical correlations as in the Kondo effect are responsible for this discrepancy, as observed for the other Pu

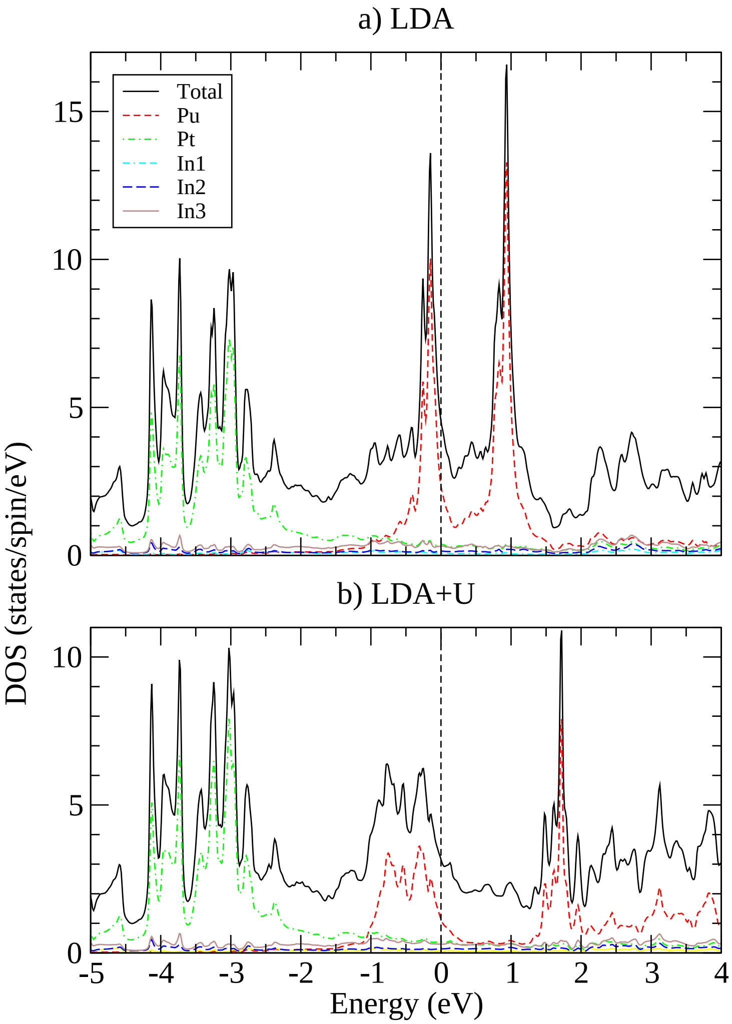

Figure 7.5. Total and partial DOSs of PM PuPt$_2$In$_7$ from a) GGA and b) GGA+U ($U = 3$ eV, $J = 0.6$ eV) calculations.

compounds in this family.

Fig. 7.6 provides the DOS of nonmagnetic PuPt$_2$Ga$_7$ from GGA and GGA+U calculations. As in PuPt$_2$In$_7$, the Pt 5d states are filled and the Pu 5f peaks, which are located between -1 and $+1.5$ eV before the implementation of U, spread to a wider range when U is turned on. The bands are generally broader compared to PuPt$_2$In$_7$, due to the smaller structure of PuPt$_2$Ga$_7$ (the smallness of the structure overrides the shortness of the Ga wavefunction). When the states near ε_F are decomposed into their total angular momentum quantum numbers m_j, we find the Pu states with $m_j = \pm 3/2$ dominate the Fermi energy. This is consistent with the idea that the most relevant hy-

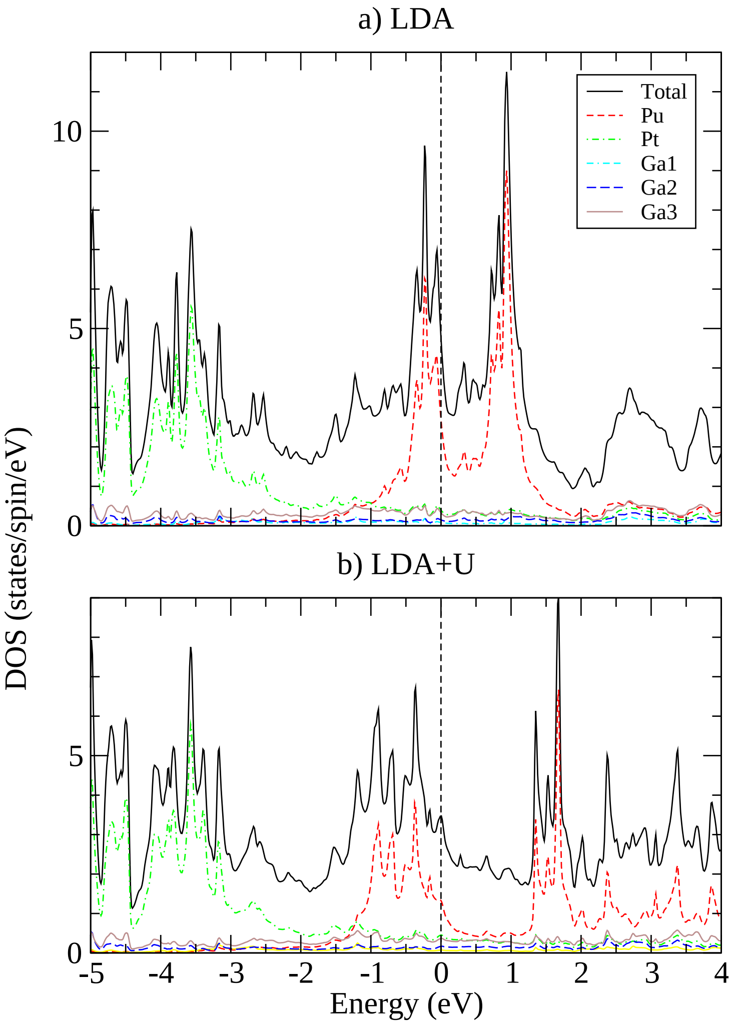

Figure 7.6. Total and partial DOSs of PM PuPt$_2$Ga$_7$ from a) GGA and b) GGA+U ($U = 3$ eV, $J = 0.6$ eV) calculations.

bridization will be between Pu and its nearest neighbors, which are not the in-plane but off-plane In atoms.

Figs. 7.7 and 7.8 are the band structures of PM PuPt$_2$In$_7$ and PuPt$_2$Ga$_7$ obtained from GGA+U calculations, with f-weight fatbands. The band structure of PM PuCoGa$_5$ is shown in Fig. 7.9 for comparison. The highly dispersive band, which spans almost 2 eV from Z to Γ and crosses the Fermi energy in PuCoGa$_5$, barely reaches ε_F in the 127s and creates a small hole Fermi surface pocket at the center of the zone (see Fig. 7.10). This indicates a reduction in dimensionality when going from the 115 to the 127, but the reduction effect is not as obvious when looking at the FSs as a whole; i.e., the

127 FSs don't seem necessarily more 2D than those of the 115s, nor vice versa [178]. Careful analysis of the band structures shows that the large 3D sheet which the 127s bear (colored turquoise in Fig. 7.10) is analogous to the 115s' large 3D piece (colored green in Fig. 7.11) *and* the red sphere centered at Γ, combined. The 127s' torquoise sheet is actually doubly layered, creating a membrane that encloses electrons, and the analogous volume in the 115s is that which is in between the 3D piece and the sphere. The detachment of these two pieces of FSs is due to the band that starts 0.8 eV above ε_F at the Γ point and disperses below the Fermi level a third of the way through X (see Fig. 7.9). This band is responsible for the 115s' spherical hole pocket centered at Γ, but, in the case of the 127s, the same band rises back above ε_F, to create the outer layer of the large turquoise piece. The lack of upturn of the band makes way for the circular tunnels that connect to adjacent BZs.

The existence of cylindrical electron pockets centered at the zone corners are a commonality amongst the Pu compounds. The cylinders of PuPt$_2$Ga$_7$ and PuCoGa$_5$ show slightly less dispersion along k_z than do, respectively, PuPt$_2$In$_7$ and PuCoIn$_5$. We used WIEN2K to calculate the plasma frequency ratio $\omega_{p,xx}/\omega_{p,zz}$ of PuPt$_2$In$_7$, PuPt$_2$Ga$_7$, PuCoIn$_5$, and PuCoGa$_5$, and they are 2.34, 3.22, 1.46, and 1.68, respectively. As expected, all four ratios are > 1. The larger value of PuPt$_2$Ga$_7$ (PuCoGa$_5$) indicates two-dimensionality is enhanced when compared to PuPt$_2$In$_7$ (PuCoIn$_5$), despite its smaller structure.

If, as in the case of the Ce-based superconductors, the presence of superconductivity relies on the proximity to an antiferromagnetic state, we would like to know the relative degree of localization in the various Pu-115, -127, and -218 compounds. From the DFT calculations we can get an estimate for the relative strength of the c-f hybridization. We take the f-electron density within the Pu muffin-tin sphere as a measure of this strength of hybridization. For identically sized MT spheres we find values of 5.11, 5.14, 5.23 and 5.24 for PuCoIn$_5$, PuPt$_2$In$_7$, PuCoGa$_5$, and PuPt$_2$Ga$_7$, respectively. Thus, we obtain that PuCoIn$_5$ is the least hybridized while PuPt$_2$Ga$_7$ would be the most strongly hybridized. This thought alone does not indicate the degree of localization. However, dynamical mean-field theory (DMFT) calculations show that the more weakly hybridized PuCoIn$_5$ indeed results in a smaller Kondo scale, T_0, relative to PuCoGa$_5$, and hence

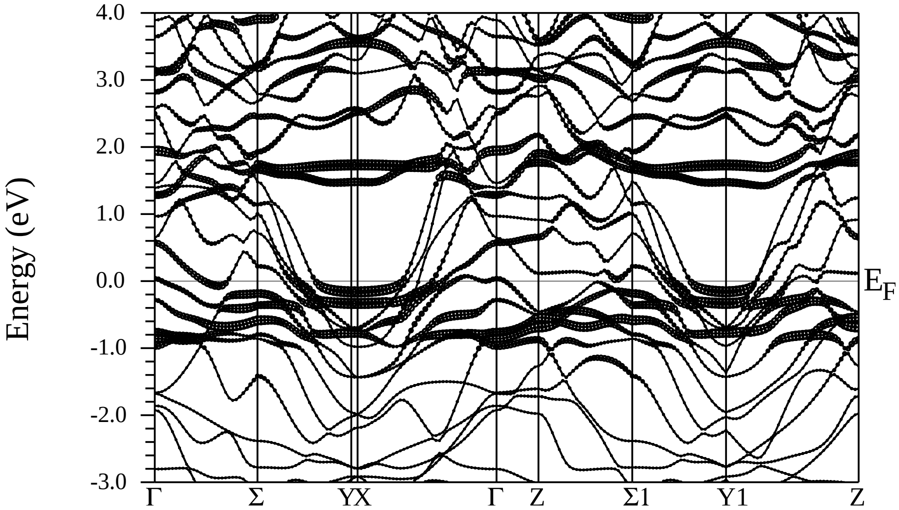

Figure 7.7. GGA+U band structure of PM PuPt$_2$In$_7$, with f-weight fatbands.

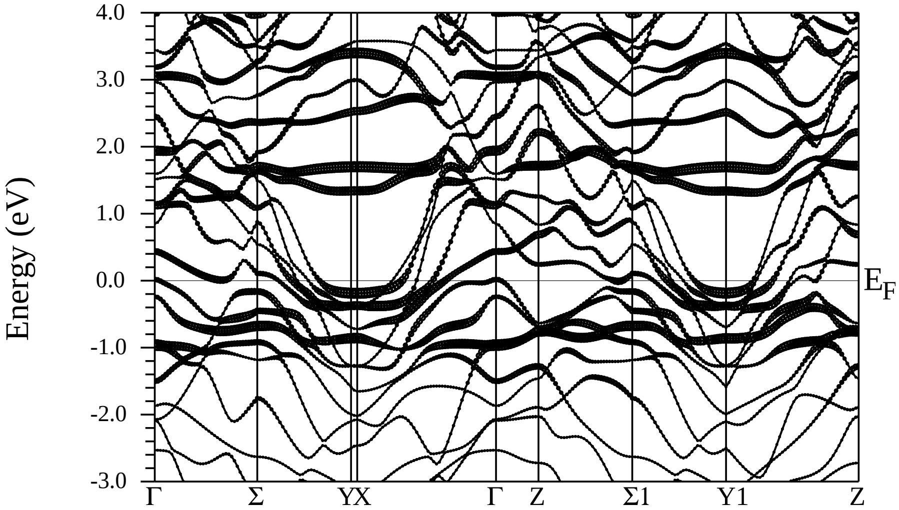

Figure 7.8. GGA+U band structure of PM PuPt$_2$Ga$_7$, with f-weight fatbands.

can be considered as more localized [195]. Thus, we can now equate the relative degree of hybridization with the relative degree of localization, and conclude that from PuCoIn$_5$ to PuPt$_2$In$_7$ to PuCoGa$_5$ to PuPt$_2$Ga$_7$ the compounds are becoming increasingly itinerant. As a result, since PuCoIn$_5$ is non-magnetic it was to be expected that PuPt$_2$In$_7$ would also be non-magnetic.

The role of the electronic structure in determining superconductivity depends on the mechanism. In some cases, superconductivity can be driven by Fermi surface nesting. Nesting, which indicates instability in the FS, can give rise to a spin density wave or

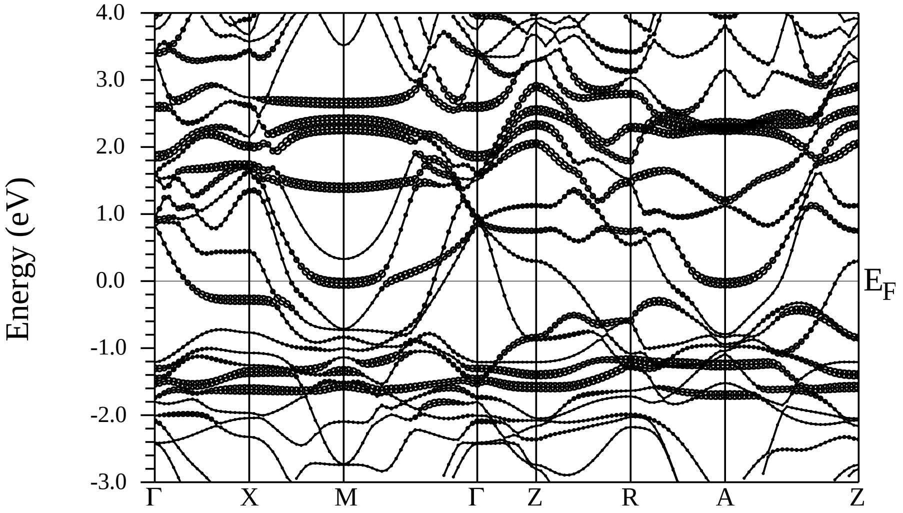

Figure 7.9. GGA+U band structure of PM PuCoGa$_5$, with f-weight fatbands.

charge density wave. In a BCS-like mechanism, even if the pairing fluctuations do not originate directly from a FS instability, the electronic structure will at a minimum determine the SC gap symmetry. In the Pu-218s, Elgazaar *e*t al. have argued that the additional FS sheets may provide sufficient differences to suppress the occurrence of superconductivity [170]. In order to see if there is any nesting present in the Pu-127s, we used the GGA band structures to calculate the real part of the constant-matrix-element noninteracting susceptibility for PuPt$_2$In$_7$ and PuPt$_2$Ga$_7$ (see Fig. 7.12). In the interest of finding nesting features that are unique to the superconductors, we calculated the susceptibilities of PuCoGa$_5$ and PuCoIn$_5$ as well. The generalized susceptibility is

$$\chi(\mathbf{q}) = -\sum_{\alpha\beta\mathbf{k}} \frac{f(\varepsilon_{\alpha,\mathbf{k}}) - f(\varepsilon_{\beta,\mathbf{k+q}})}{\varepsilon_{\alpha,\mathbf{k}} - \varepsilon_{\beta,\mathbf{k+q}} + i\delta},$$

where f denotes the Fermi distribution function, $\varepsilon_{\alpha,\mathbf{k}}$ is the energy dispersion, and α and β are band indices. Alongside the conventional $\chi(\mathbf{q})$, we also calculated the susceptibility incorporating the relative weight of the Pu f orbital, so as to pick out the attributes dominated by Pu f character. In the style of Mazin as in Ref. 196, the *weighted* susceptibility $\tilde{\chi}(\mathbf{q})$ is

$$\tilde{\chi}(\mathbf{q}) = -\sum_{\alpha\beta\mathbf{k}} \frac{f(\varepsilon_{\alpha,\mathbf{k}}) - f(\varepsilon_{\beta,\mathbf{k+q}})}{\varepsilon_{\alpha,\mathbf{k}} - \varepsilon_{\beta,\mathbf{k+q}} + i\delta} W_{\alpha,\mathbf{k}} W_{\beta,\mathbf{k+q}},$$

where W is the weight of the f orbital. As shown in Fig. 7.12, in which the susceptibilities are normalized and plotted along the $q_x q_y$ plane for $q_z = 0.5$, in all four cases non-

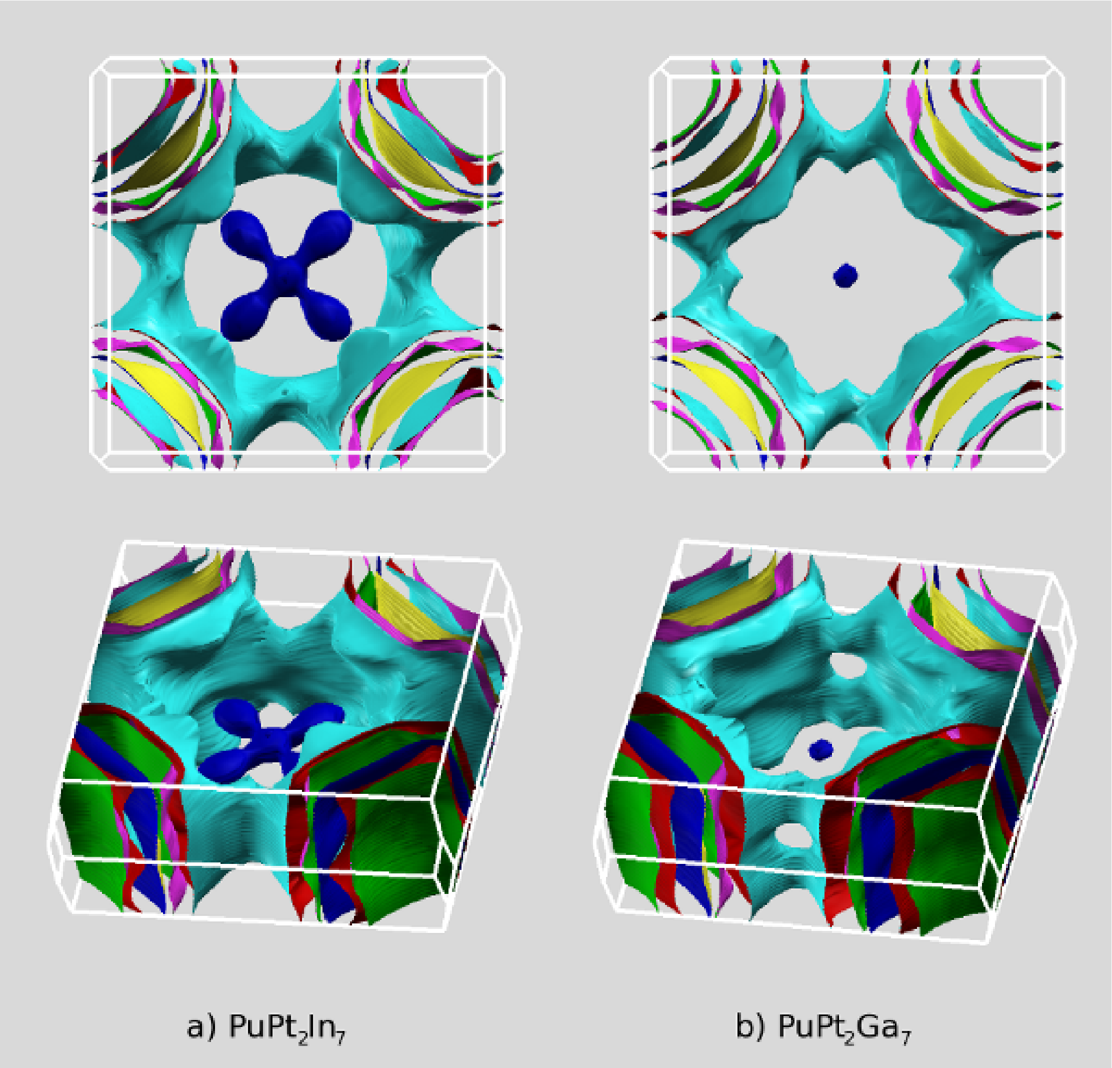

Figure 7.10. (Color online) Calculated FSs of a) PuPt$_2$In$_7$ and b) PuPt$_2$Ga$_7$ in the GGA+U scheme. Γ is located in the center of the unit cell. For clarity, the 3D FSs are reproduced in the bottom figures.

weighted $\chi(\mathbf{q})$ and f-weighted $\tilde{\chi}(\mathbf{q})$ look almost identical, demonstrating that the weights of other atoms and orbitals were negligible to begin with. PuPt$_2$In$_7$ and PuPt$_2$Ga$_7$ have similar-looking susceptibility plots, as do PuCoGa$_5$ and PuCoIn$_5$. Moreover, the susceptibilities of the 115s aren't very dissimilar to those of the 127s. The primary difference is that the 127s feature elevated values along $(0.5, q_x)$ (and equivalently, $(q_y, 0.5)$), which can also be seen, to a much lesser degree, in PuCoIn$_5$. The peak-like character is most pronounced for PuCoGa$_5$, which has the highest T_c of the four compounds.

Wang *et* al. [197] noted two peaks in PuCoGa$_5$'s $\chi(\mathbf{q})$, at $\mathbf{q} = (0.5, 0.5, 0)$ and $\mathbf{q} =$

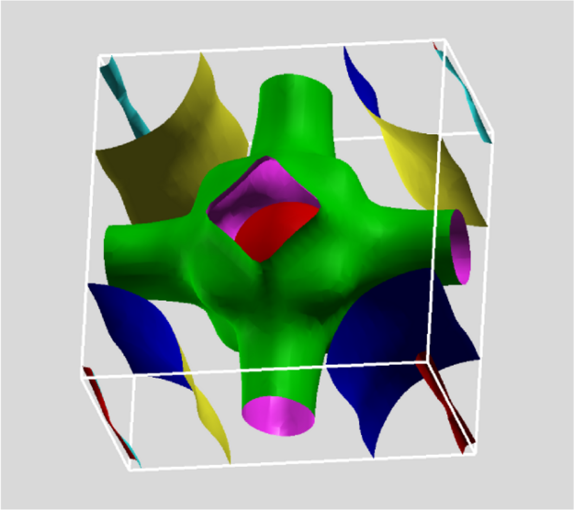

Figure 7.11. (Color online) Calculated FSs of PuCoGa$_5$ in the GGA+U scheme. Γ is located in the center of the unit cell.

$(0.5, 0.5, 0.5)$. More accurately, the two peaks are part of a relatively broad mountain ridge that, when plotted on the $q_y q_z$ (or, equivalently, $q_x q_z$) plane, spans all the way in the q_z direction. This ridge is seen in all four Pu compounds, and is plotted in Fig. 7.13 for PuCoGa$_5$. When χ and $\tilde{\chi}$ are plotted along a $q_x q_y$ plane for any q_z, the apex appears at the corner of the Brillouin zone ($q_x = q_y = 0.5$), as can be seen in Fig. 7.12. That there is little variation in the landscape when varying q_z indicates a truly 2D topography in the susceptibility for both Pu-115s and Pu-127s.

When it comes to the source of the maxima $(0.5, 0.5, q_z)$, in all cases, the major contribution is interband nesting involving the largest FS sheet. In the 115s, the large sheet connects with the larger of the two 2D cylinders (Fig. 7.11); in the 127s, it maps onto the two of the larger cylinders (Fig. 7.11), where nesting with the bigger of the two cylinders is stronger than nesting with the smaller, by 7%/20% for PuPt$_2$In$_7$/PuPt$_2$Ga$_7$. Nesting between the large sheet and cylinder accounts for, on average, 32% of the susceptibility strength of PuCoGa$_5$, while that factor is only 24% for PuCoIn$_5$. Nestings between the large sheet and each of the two larger cylinders collectively account for 28% for PuPt$_2$Ga$_7$ and 26% for PuPt$_2$In$_7$. (Comparing the contributions from two cylinders in the 127s to the single one in the 115s is sensible in that there are twice as many atoms in the unit cell of the 127s.) PuPt$_2$In$_7$ and PuPt$_2$Ga$_7$ have similar susceptibility plots, as do PuCoGa$_5$ and PuCoIn$_5$, demonstrating the type of ligand atom has very little influence on the

a) Non-weighted susceptibility

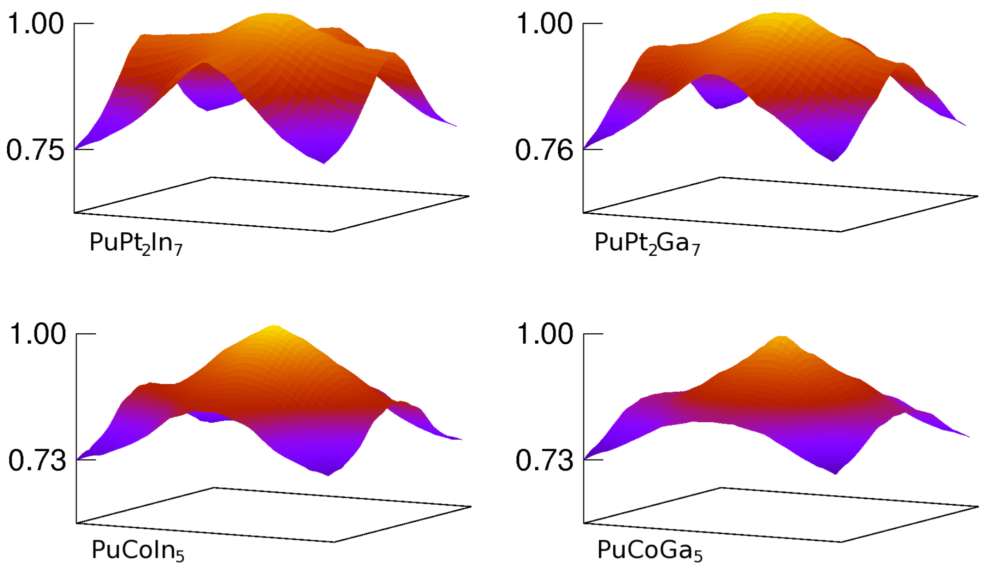

b) f-weighted susceptibility

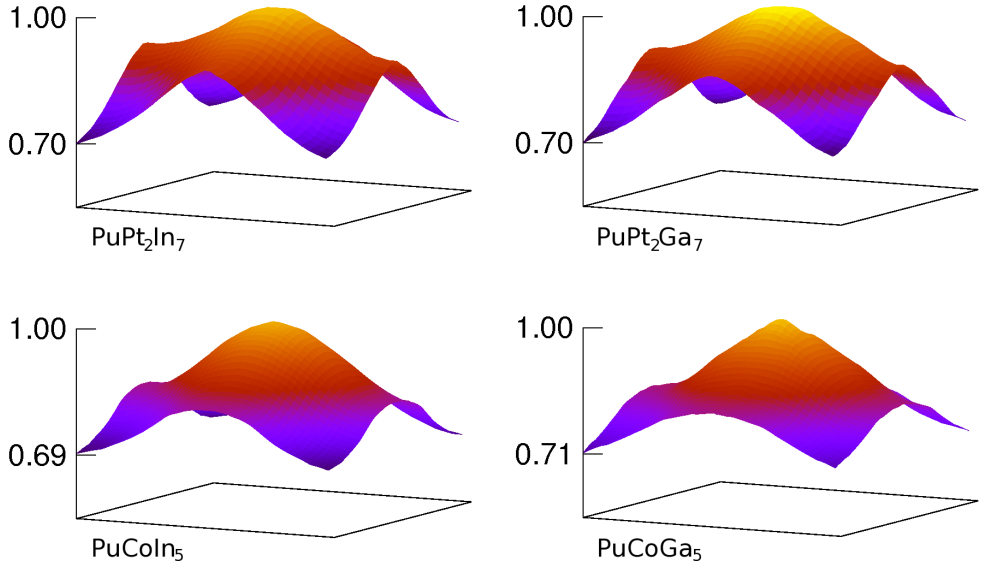

Figure 7.12. (Color online) a) Non-weighted and b) f-weighted normalized noninteracting spin susceptibilities χ and $\tilde{\chi}$, respectively, of Pu-based compounds along the $q_x q_y$ plane in the conventional Brillouin zone for $q_z = 0.5$. $\mathbf{q} = (0, 0, 0)$ are at the corners.

shape of $\chi(\mathbf{q})$. Even the individual band-decomposed $\chi_{\alpha\beta}$'s are consistent throughout the compounds. The aforementioned "elevated values" of the 127 susceptibilities form a cross along the $q_x = 0.5$ line and the $q_y = 0.5$ line in the plots in Fig. 7.12, with the cross intersection coinciding with the apical point $(0.5, 0.5)$. Even though the plot looks as

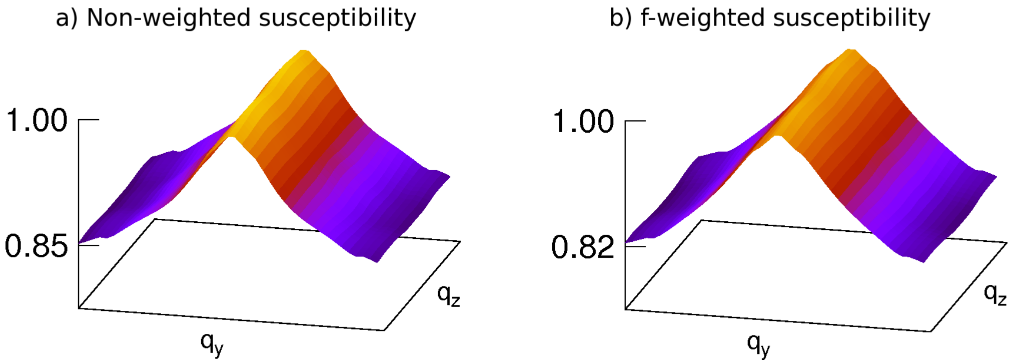

Figure 7.13. (Color online) Normalized a) χ and b) $\tilde{\chi}$ of PuCoGa$_5$ in the conventional Brillouin zone for $q_x = 0.5$. $\mathbf{q} = (0, 0, 0)$ are at the corners. Susceptibilities of the other three Pu compounds look qualitatively equivalent.

though χ remains strong along the cross at $(0, 0.5)$, when considering only contributions from nesting between the large sheet and cylinders, the 127s' susceptibilities take on more of the conical shape that the 115s possess (these contributions at $(0.5, 0.5)$ are 73% stronger than at $(0, 0.5)$).

What do these calculations tell us about superconductivity? Given the virtually identical FSs, $\chi(\mathbf{q})$, and $\tilde{\chi}(\mathbf{q})$ at the DFT level for PuCoIn$_5$ and PuCoGa$_5$ whose superconducting T_c differs by nearly an order of magnitude, suggests an additional energy scale must be important. The most likely candidate is the Kondo energy scale, T_0, extracted from either specific heat measurements or DMFT calculations. As mentioned above, earlier DMFT work on these two compounds shows that the hybridization strength inferred from DFT calculations can predict the relative trend of T_0 between various Pu-based family members [195]. Consequently, our work shows that T_0 increases from PuCoIn$_5$ to PuPt$_2$In$_7$ to PuCoGa$_5$ to PuPt$_2$Ga$_7$. Thus, we naively expect the scale of T_c for PuPt$_2$In$_7$ to be between that of PuCoIn$_5$ and PuCoGa$_5$. As a result, it is surprising that PuPt$_2$In$_7$ is not superconducting, especially given the similarity of the susceptibility between the Pu-115's and the Pu-127's. Of course, subtle differences do exist in $\chi(\mathbf{q})$ which may be sufficient to drive T_c below 2 K in PuPt$_2$In$_7$, and more work is needed to investigate this possibility. However, the fact that PuPt$_2$In$_7$ is non-superconducting and has an intermediate scale of T_0 between PuCoIn$_5$ and PuCoGa$_5$ suggests an alternative scenario where two different instabilities mediate superconductivity in PuCoIn$_5$ and PuMGa$_5$ (M=Co, Rh) respectively [166]. In this case, PuPt$_2$In$_7$ may not be superconducting because it is not sufficiently close to either instability.

Finally, a comment with regards to the pairing symmetry. Without knowledge of the pairing potential it is difficult to make concrete predictions. However, let us assume for the moment that the pairing potential is peaked at $(0.5, 0.5)$ as is almost certainly the case in $\mathrm{CeRhIn_5}$ and $\mathrm{CePt_2In_7}$. This is also the expectation based on our calculated susceptibilities for both Pu-115s and Pu-127s if one were to use a uniform U, weak coupling approach. In this case, since the dominant contribution to the susceptibility at $(0.5, 0.5, q_z)$ is from nesting between the central large FS sheet and the cylinders centered at $(0.5, 0.5)$ we would anticipate the order parameter to change sign between these two FS sheets [198], as is believed to occur in the Fe-based superconductors. However, our analysis of the susceptibility shows that the Pu-127s contain significant intraband nesting as well. A $d_{x^2-y^2}$ like gap structure is preferred if the dominant term in the susceptibility originated from states in the vicinity of $(0.5, 0)$ (and equivalent points) as is the case in the cuprate superconductors. As we mentioned earlier, $\mathrm{PuPt_2Ga_7}$ contains precisely such a contribution.

7.5 Conclusion

We have reported the properties of $\mathrm{PuPt_2In_7}$ a structurally more 2D version of the known Pu-based superconductors. The gross similarities in structure and FSs between $\mathrm{PuPt_2In_7}$ and the other known Pu-based superconductors suggest that $\mathrm{PuPt_2In_7}$ may be a likely candidate to find superconductivity. However no superconductivity or magnetic order was observed down to 2 K. Our calculations suggest two possibilities for the lack of superconductivity in $\mathrm{PuPt_2In_7}$. The first relies on the assumption that superconductivity in $\mathrm{PuCoIn_5}$ and $\mathrm{PuCoGa_5}$ are mediated by two different instabilities[166]. Then, based on the fact that the c-f hybridization of $\mathrm{PuPt_2In_7}$ is intermediate between $\mathrm{PuCoIn_5}$ and $\mathrm{PuCoGa_5}$ it may simply lie too far from either instability to superconduct. Second, the more complex Fermi surface of the Pu-127s suggests that multiple superconducting orders may compete with one another driving T_c below 2 K as a result. Our calculations of a hypothetical $\mathrm{PuPt_2Ga_7}$ reveal strong similarites to $\mathrm{PuPt_2In_7}$ and $\mathrm{PuCoGa_5}$ suggesting that it is a promising candidate to find superconductivity if it can be synthesized. More work is needed to explore these various possibilities.

7.6 Acknowledgments

This work was supported by DOE grant DE-FG02-04ER46111, the Strategic Sciences Academic Alliance Program under grant DE-FG03-03NA00071, and by DOE SciDAC Grant No. DE-FC02-06ER25794. Work at Los Alamos was performed under the auspices of the U.S. DOE, Office of Science, Division of Materials Sciences and Engineering, and supported in part by the Laboratory Directed Research and Development program. Work at Lawrence Berkeley National Laboratory was supported by the U.S. Department of Energy (DOE), Office of Basic Energy Sciences (OBES) under Contract No. DE-AC02-05CH11231. X-ray absorption data were collected at SSRL, a national user facility operated by Stanford University on behalf of the DOE/OBES.

References

[1] P. C. Canfield and G. W. Crabtree, Phys. Today **56**, 34 (2003).

[2] F. M. Grosche, I. R. Walker, S. R. Julian, N. D. Mathur, D. M. Freye, M. J. Steiner, and G. G. Lonzarich, J. Phys.: Cond. Matt. **13**, 2845 (2001).

[3] P. Monthoux, D. Pines, and G. G. Lonzarich, Nature **450**, 1177 (2007).

[4] J. S. Schilling, *Periodic table of superconductivity*, URL `http://physics.wustl.edu/ jss/NewPeriodicTable.pdf`.

[5] S. Deemyad and J. S. Schilling, Phys. Rev. Lett. **91**, 167001 (2003).

[6] M. Cococcioni and S. de Gironcoli, Phys. Rev. B **71**, 035105 (2005).

[7] V. Iota, C.-S. Yoo, J.-H. Klepeis, Z. Jenei, W. Evans, and H. Cynn, Nat. Mat. **6**, 34 (2007).

[8] B. R. Maddox, Ph.D. thesis, University of California, Davis (2006).

[9] A. W. Lawson and T.-Y. Tang, Rev. Sci. Instrum. **21**, 815 (1950).

[10] A. E. Lazicki, Ph.D. thesis, University of California, Davis (2007).

[11] *Aerial photo of the advanced photon source*, URL `http://www.aps.anl.gov/About/APS_Overview/`.

[12] K. Momma and F. Izumi, J. Appl. Cryst. **41**, 653 (2008).

[13] M. Debessai, T. Matsuoka, J. J. Hamlin, A. K. Gangopadhyay, J. S. Schilling, K. Shimizu, and Y. Ohishi, Phys. Rev. B **78**, 214517 (2008).

[14] T. Matsuoka, M. Debessai, J. J. Hamlin, A. K. Gangopadhyay, J. S. Schilling, and K. Shimizu, Phys. Rev. Lett. **100**, 197003 (2008).

[15] E. A. Stern, Phys. Rev. B **48**, 9825 (1993).

[16] K. Onnes, Leid. Comm. **120b** (1911).

[17] K. Onnes, Nature **77**, 581 (1908).

[18] W. Meissner and R. Ochsenfeld, Naturw. **21**, 787 (1933).

[19] F. London and H. London, Physica **2**, 341 (1935).

[20] F. London, Physica **2**, 341 (1935).

[21] F. London and H. London, Proc. R. Soc. Lond. A **149**, 71 (1935).

[22] V. L. Ginzburg and L. D. Landau, Zh. Eksp. Teor. Fiz. **20**, 1064 (1950).

[23] J. Bardeen, L. N. Cooper, and J. R. Schrieffer, Phys. Rev. **106**, 162 (1957).

[24] E. Maxwell, Phys. Rev. **78**, 477 (1950).

[25] C. A. Reynolds, B. Serin, W. H. Wright, and L. B. Nesbitt, Phys. Rev. **78**, 487 (1950).

[26] N. N. Bogliubov, Nuovo Cimento **7**, 794 (1958).

[27] J. G. Valatin, Nuovo Cimento **7**, 843 (1958).

[28] J. G. Bednorz and K. A. Müller, Z. Phys. B **64**, 189 (1986).

[29] F. Steglich, J. Aarts, C. D. Bredl, W. Lieke, D. Meschede, W. Franz, and H. Schäfer, Phys. Rev. Lett. **43**, 1892 (1979).

[30] N. D. Mathur, F. M. Grosche, S. R. Julian, I. R. Walker, D. M. Freye, R. K. W. Hasewimmer, and G. G. Lonzarich, Nature **394**, 39 (1998).

[31] J. Nagamatsu, N. Nakagawa, T. Muranaka, Y. Zenitani, and J. Akimitsu, Nature **410**, 63 (2001).

[32] Y. Kamihara, T. Watanabi, M. Hirano, and H. Hosono, J. Am. Chem. Soc. **130**, 3296 (2008).

[33] J. R. Schrieffer, *Theory of Superconductivity* (Perseus Books, 1999), chap. 2-4: The Pairing Approximation, pp. 36–41.

[34] T. D. Lee, F. E. Low, and D. Pines, Phys. Rev. **90**, 297 (1953).

[35] J. M. An and W. E. Pickett, Phys. Rev. Lett. **86**, 4366 (2001).

[36] J. Kortus, I. I. Mazin, K. D. Belashchenko, V. P. Antropov, and L. L. Boyer, Phys. Rev. Lett. **86**, 4656 (2001).

[37] S. L. Bud'ko, G. Lapertot, C. Petrovic, C. E. Cunningham, N. Anderson, and P. C. Canfield, Phys. Rev. Lett. **86**, 1877 (2001).

[38] A. Sharoni, I. Felner, and O. Millo, Phys. Rev. B **63**, 220508(R) (2001).

[39] D. K. Finnemore, J. E., Ostenson, S. L. Bud'ko, G. Lapertot, and P. C. Canfield, Phys. Rev. Lett. **86**, 2420 (2001).

[40] A. B. Migdal, Sov. Phys. JETP **34**, 1438 (1958).

[41] G. M. Eliashberg, Sov. Phys. JETP **38**, 966 (1960).

[42] D. Rainer, in *Progress in Low Temperature Physics*, edited by D. F. Brewer (Elsevier, 1986), vol. 10, pp. 371–424.

[43] A. Y. Liu, I. I. Mazin, and J. Kortus, Phys. Rev. Lett. **87**, 087005 (2001).

[44] Y. Kong, O. V. Dolgov, O. Jepsen, and O. K. Andersen, Phys. Rev. B **64**, 020501 (2001).

[45] H. Choi, D. Roundy, H. Sun, M. L. Cohen, and S. G. Louie, Phys. Rev. B **66**, 020513 (2002).

[46] K.-P. Bohnen, R. Heid, and B. Renker, Phys. Rev. Lett. **86**, 5771 (2001).

[47] F. Bouquet, R. A. Fisher, N. E. Phillips, D. G. Hinks, and J. D. Jorgensen, Phys. Rev. Lett. **87**, 047001 (2001).

[48] P. Szabó, P. Samuely, J. Kačmarčik, T. Klein, J. Marcus, D. Fruchart, S. Miraglia, C. Marcenat, and A. G. M. Jansen, Phys. Rev. Lett. **87**, 137005 (2001).

[49] S. Kuroiwa, H. Sagayama, T. Kakiuchi, H. Sawa, Y. Noda, and J. Akimitsu, Phys. Rev. B **74**, 014517 (2006).

[50] H. Rosner, A. Kitaigorodsky, and W. E. Pickett, Phys. Rev. Lett. **88**, 127001 (2002).

[51] L. Boeri, J. Kortus, and O. K. Andersen, Phys. Rev. Lett. **93**, 237002 (2004).

[52] J. Kondo, Prog. Th. Phys. **32**, 37 (1964).

[53] H. R. Ott, H. Rudigier, Z. Fisk, and J. L. Smith, Phys. Rev. Lett. **50**, 1595 (1983).

[54] G. R. Stewart, Z. Fisk, J. O. Willis, and J. L. Smith, Phys. Rev. Lett. **52**, 679 (1984).

[55] T. T. M. Palstra, A. A. Menovsky, J. v. d. Berg, A. J. Dirkmaat, P. H. Kes, G. J. Nieuwenhuys, and J. A. Mydosh, Phys. Rev. Lett. **55**, 2727 (1985).

[56] J. L. Sarrao, L. A. Morales, J. D. Thompson, B. L. Scott, G. R. Stewart, F. Wastin, J. Rebizant, P. Boulet, E. Colineau, and G. H. Lander, Nature **420**, 297 (2002).

[57] C. S. Yoo, B. Maddox, J.-H. P. Klepeis, V. Iota, W. Evans, A. McMahan, M. Y. Hu, P. Chow, M. Somayazulu, D. Häusermann, et al., Phys. Rev. Lett. **94**, 115502 (2005).

[58] G. J. Sizoo and H. K. Onnes, Commun. Phys. Lab. Univ. Leiden **180b**, 13 (1925).

[59] J. Tuoriniemi, K. Juntunen-Nurmilaukas, J. Uusvouri, E. Pentti, A. Salmela, and A. Sebedash, Nature **447**, 187 (2007).

[60] T. Yabuuchi, T. Matsuoka, Y. Nakamoto, and K. Shimizu, J. Phys. Soc. Jpn. **75**, 083703 (2006).

[61] Z. P. Yin, F. Gygi, and W. E. Pickett, Phys. Rev. B **80**, 184515 (2009).

[62] J. Feng, N. W. Ashcroft, and R. Hoffmann, Phys. Rev. Lett. **98**, 247002 (2007).

[63] J. S. Tse, D. D. Klug, S. Desgreniers, J. S. Smith, and R. Dutrisac, Europhys. Lett. **86**, 56001 (2009).

[64] Y. Xie, A. R. Oganov, and Y. Ma, Phys. Rev. Lett. **104**, 177005 (2010).

[65] P. Zeeman, Nature **55**, 347 (1897).

[66] P. Hohenberg and W. Kohn, Phys. Rev. **136**, B864 (1964).

[67] W. Kohn and L. J. Sham, Phys. Rev. **140**, A1133 (1965).

[68] V. Fock, Zeits. f. Physik **61**, 126 (1930).

[69] M. Born and R. Oppenheimer, Annalen der Physik **389**, 457 (1927).

[70] R. M. Martin, *Electronic Structure: Basic Theory and Practical Methods* (Cambridge University Press, 2008), chap. Appendix C: Adiabatic approximation, pp. 482–484.

[71] C.-O. Almbladh and U. von Barth, Phys. Rev. B **31**, 3231 (1985).

[72] F. Bloch, Z. Phys. A **52**, 555 (1929).

[73] P. A. M. Dirac, Math. Proc. Camb. Phil. Soc. **26**, 376 (1930).

[74] J. C. Slater, Phys. Rev. **81**, 385 (1951).

[75] D. M. Ceperley and B. J. Alder, Phys. Rev. Lett. **45**, 566 (1980).

[76] S. H. Vosko, L. Wilk, and M. Nusair, Can. J. Phys. **58**, 1200 (1980).

[77] J. P. Perdew and A. Zunger, Phys. Rev. B **23**, 5048 (1981).

[78] L. A. Cole and J. P. Perdew, Phys. Rev. A **25**, 1265 (1982).

[79] J. P. Perdew and Y. Wang, Phys. Rev. B **45**, 13244 (1992).

[80] D. C. Langreth and M. J. Mehl, Phys. Rev. B **28**, 1809 (1983).

[81] D. C. Langreth and J. P. Perdew, Phys. Rev. B **21**, 5469 (1980).

[82] J. P. Perdew and W. Yue, Phys. Rev. B **33**, 8800 (1986).

[83] A. D. Becke, J. Chem. Phys. **96**, 2155 (1991).

[84] J. P. Perdew and Y. Wang, Phys. Rev. B **45**, 13244 (1992).

[85] J. P. Perdew, K. Burke, and M. Ernzerhof, Phys. Rev. Lett. **77**, 3865 (1996).

[86] V. I. Anisimov, J. Zaanen, and O. K. Andersen, Phys. Rev. B **44**, 943 (1991).

[87] J. P. Perdew, R. G. Parr, M. Levy, and J. L. Balduz, Phys. Rev. Lett. **49**, 1691 (1982).

[88] R. W. Godby, M. Schlüter, and L. J. Sham, Phys. Rev. Lett. **56**, 2415 (1986).

[89] V. I. Anisimov, I. V. Solovyev, M. A. Korotin, M. T. Czyżyk, and G. A. Sawatzky, Phys. Rev. B **48**, 16929 (1993).

[90] A. I. Liechtenstein, V. I. Anisimov, and J. Zaanen, Phys. Rev. B **52**, R5467 (1995).

[91] M. T. Czyżyk and G. A. Sawatzky, Phys. Rev. B **49**, 14211 (1994).

[92] K. Schwarz and P. Blaha, Comp. Mat. Sci. **28**, 259 (2003).

[93] P. Blaha, K. Schwarz, P. Sorantin, and S. Trickey, Comp. Phys. Comm. **59**, 399 (1990).

[94] K. Koepernik and H. Eschrig, Phys. Rev. B **59**, 1743 (1999).

[95] E. R. Ylvisaker, W. E. Pickett, and K. Koepernik, Phys. Rev. B **79**, 035103 (2009).

[96] D. D. Koelling and G. O. Arbman, J. Phys. F: Met. Phys. **5**, 2041 (1975).

[97] O. K. Andersen, Phys. Rev. B **12**, 3060 (1975).

[98] J. C. Slater, Phys. Rev. **51**, 846 (1937).

[99] J. Korringa, Physica **13**, 392 (1947).

[100] W. Kohn and N. Rostoker, Phys. Rev. **94**, 1111 (1954).

[101] O. K. Andersen, in *Computational Methods in Band Theory*, edited by P. Marcus, J. Janak, and A. Williams (Plenum Press, New York 1971, 1971), pp. 178–182.

[102] P. M. Marcus, Int. J. Quant. Chem. **1**, 567 (1967).

[103] L. Hodges, R. E. Watson, and H. Ehrenreich, Phys. Rev. B **5**, 3953 (1972).

[104] O. K. Andersen, Solid State Communications **13**, 133 (1973).

[105] D. J. Singh, Phys. Rev. B **43**, 6388 (1991).

[106] P. W. Bridgman, Proc. Am. Acad. Arts Sci. **74**, 425 (1942).

[107] P. W. Bridgman, Proc. Am. Acad. Arts Sci. **81**, 165 (1952).

[108] C. E. Weir, E. R. Lippincott, A. V. Valkenburg, and E. N. Bunting, J. Res. Natl. Bur. Stand. A **63**, 55 (1959).

[109] A. W. Lawson and N. A. Riley, Rev. Sci. Instrum. **20**, 763 (1949).

[110] J. C. Jamieson, A. W. Lawson, and N. D. Nachtrieb, Rev. Sci. Instrum. **30**, 1016 (1959).

[111] H. K. Mao and P. M. Bell, *Carnegie Institution of Washington Year Book* (Carnegie Institution of Washington, 1978), vol. 77, p. 903.

[112] H. K. Mao, Science **200**, 1145 (1978).

[113] G. J. Piermarini and S. Block, Rev. Sci. Instrum. **46**, 973 (1975).

[114] W. A. Bassett, T. Takahashi, and P. W. Stook, Rev. Sci. Instrum. **38**, 37 (1967).

[115] H. K. Mao and P. M. Bell, *Carnegie Institution of Washington Year Book* (Carnegie Institution of Washington, 1977), vol. 76, p. 644.

[116] R. A. Forman, G. J. Piermarini, J. D. Barnett, and S. Block, Science **176**, 284 (1972).

[117] G. J. Piermarini, S. Block, J. D. Barnett, and R. A. Forman, J. Appl. Phys. **46**, 2774 (1975).

[118] D. L. Decker, J. Appl. Phys. **42**, 3239 (1971).

[119] H. K. Mao, J. Xu, and P. M. Bell, J. Geophys. Res. **91**, 4673 (1986).

[120] H. B. Rhee, S. Banerjee, E. R. Ylvisaker, and W. E. Pickett, Phys. Rev. B **81**, 245114 (2010).

[121] S. Yamanaka, H. Kawaji, K.-i. Hotehama, and M. Ohashi, Adv. Mat. **8**, 771 (1996).

[122] S. Shamoto, T. Kato, Y. Ono, Y. Miyazaki, K. Ohoyama, M. Ohashi, Y. Yamaguchi, and T. Kajitani, Physica C **306**, 7 (1998).

[123] S. Yamanaka, K.-I. Hotehama, and H. Kawaji, Nature **392**, 580 (1998).

[124] S. Shamoto, K. Iizawa, M. Yamada, K. Ohoyama, Y. Yamaguchi, and T. Kajitani, J. Am. Chem. Soc. **60**, 1431 (1999).

[125] S. Yamanaka, T. Yasunaga, K. Yamaguchi, and M. Tagawa, J. Mater. Chem. **19**, 2573 (2009).

[126] S. Kuroiwa, H. Kawashima, H. Kinoshita, H. Okabe, and J. Akimitsu, Physica C **466**, 11 (2007).

[127] E. Bustarret, C. Marcenat, P. Achatz, J. Kačmarčik, F. Lévy, A. Huxley, L. Ortéga, E. Bourgeois, X. Blase, D. Débarre, et al., Nature **444**, 465 (2006).

[128] E. Ekimov, V. Sidorov, E. Bauer, N. Mil'nik, N. Curro, J. Thompson, and S. Stishov, Nature **428**, 542 (2004).

[129] L. F. Mattheiss, E. M. Gyorgy, and D. W. Johnson, Phys. Rev. B **37**, 3745 (1988).

[130] S. Jin, T. Tiefel, R. Sherwood, A. Ramirez, E. Gyorgy, G. Kammlott, and R. Fastnacht, Appl. Phys. Lett. **53**, 1116 (1988).

[131] H. Sagayama, Y. Wakabayashi, H. Sawa, T. Kamiyama, A. Hoshikawa, S. Harjo, K. Uozato, A. K. Ghosh, M. Tokunaga, and T. Tamegai, J. Phys. Soc. Jpn. **75**, 043713 (2006).

[132] I. R. Shein, N. I. Medvedeva, and A. L. Ivanovskii, J. Phys.: Condens. Matter **15**, L541 (2003).

[133] G. Q. Huang, L. F. Chen, M. Liu, and D. Y. Xing, Phys. Rev. B **69**, 064509 (2004).

[134] I. I. Mazin and D. A. Papaconstantopoulos, Phys. Rev. B **69**, 180512(R) (2004).

[135] M. Giantomassi, L. Boeri, and G. B. Bachelet, Phys. Rev. B **72**, 224512 (2005).

[136] R. Heid, K. Bohnen, B. Renker, P. Adelmann, T. Wolf, D. Ernst, and H. Schober, J. Low Temp. Phys. **147**, 375 (2007).

[137] S. Kuroiwa, A. Q. R. Baron, T. Muranaka, R. Heid, K.-P. Bohnen, and J. Akimitsu, Phys. Rev. B **77**, 140503 (2008).

[138] W. Westerhaus and H. Schuster, Z. Naturforsch B **34**, 352 (1979).

[139] A. B. Kyker, W. E. Pickett, and F. Gygi, Phys. Rev. B **71**, 224517 (2005).

[140] H. Rosner, R. Weht, M. D. Johannes, W. E. Pickett, and E. Tosatti, Phys. Rev. Lett. **88**, 027001 (2001).

[141] N. Ashcroft and N. Mermin, *Solid State Physics* (Harcourt Brace, 1976), p. Eq. (13.65).

[142] K. Durczewski and M. Ausloos, Z. Phys. B Cond. Matt. **85**, 59 (1991).

[143] D. J. Singh, Phys. Rev. B **78**, 094511 (2008).

[144] I. I. Mazin, D. J. Singh, M. D. Johannes, and M. H. Du, Phys. Rev. Lett. **101**, 057003 (2008).

[145] A. N. Yaresko, G.-Q. Liu, V. N. Antonov, and O. K. Andersen, Phys. Rev. B **79**, 144421 (2009).

[146] F. S. Khan and P. B. Allen, Phys. Rev. B **29**, 3341 (1984).

[147] K.-W. Lee and W. E. Pickett, Phys. Rev. Lett. **93**, 237003 (2004).

[148] K.-W. Lee and W. E. Pickett, Phys. Rev. B **72**, 174505 (2005).

[149] J. F. Janak, Phys. Rev. B **16**, 255 (1977).

[150] H. Rietschel and L. J. Sham, Phys. Rev. B **28**, 5100 (1983).

[151] M. Grabowski and L. J. Sham, Phys. Rev. B **29**, 6132 (1984).

[152] A. Bill, H. Morawitz, and V. Z. Kresin, Phys. Rev. B **66**, 100501 (2002).

[153] A. Bill, H. Morawitz, and V. Z. Kresin, Phys. Rev. B **68**, 144519 (2003).

[154] W. Pickett, Physica B **296**, 112 (2001).

[155] J. Neaton and N. Ashcroft, Nature **400**, 141 (1999).

[156] S. Desgreniers and K. Lagarec, J. Appl. Cryst. **27**, 432 (1994).

[157] D. Jaccard, K. Behnia, and J. Sierro, Phys. Lett. A **163**, 475 (1992).

[158] J. Thompson, R. Movshovich, Z. Fisk, F. Bouquet, N. Curro, R. Fisher, P. Hammel, H. Hegger, M. Hundley, M. Jaime, et al., J. Magn. Magn. Mater. **226–230**, 5 (2001).

[159] H. Hegger, C. Petrovic, E. G. Moshopoulou, M. F. Hundley, J. L. Sarrao, Z. Fisk, and J. D. Thompson, Phys. Rev. Lett. **84**, 4986 (2000).

[160] C. Petrovic, P. G. Pagliuso, M. F. Hundley, R. Movshovich, J. L. Sarrao, J. D. Thompson, Z. Fisk, and P. Monthoux, J. Phys.: Condens. Matter **13**, L337 (2001).

[161] C. Petrovic, R. Movshovich, M. Jaime, P. G. Pagliuso, M. F. Hundley, J. L. Sarrao, Z. Fisk, and J. D. Thompson, Europhys. Lett. **53**, 354 (2001).

[162] G. Chen, S. Ohara, M. Hedo, Y. Uwatoko, K. Saito, M. Sorai, and I. Sakamoto, J. Phys. Soc. Jpn. **71**, 2836 (2002).

[163] F. Wastin, P. Boulet, J. Rebizant, E. Colineau, and G. H. Lander, J. Phys.: Condens. Matter **15**, S2279 (2003).

[164] D. Kaczorowski, A. P. Pikul, D. Gnida, and V. H. Tran, Phys. Rev. Lett. **103**, 027003 (2009).

[165] E. D. Bauer, H. O. Lee, V. A. Sidorov, N. Kurita, K. Gofryk, J.-X. Zhu, F. Ronning, R. Movshovich, J. D. Thompson, and T. Park, Phys. Rev. B **81**, 180507 (2010).

[166] E. D. Bauer, M. M. Altarawneh, P. H. Tobash, K. Gofryk, O. E. Ayala-Valenzuela, J. N. Mitchell, R. D. McDonald, C. H. Mielke, F. Ronning, J.-C. Griveau, et al., J. Phys.: Condens. Matter **24**, 052206 (2012).

[167] V. Sechovský, L. Havela, G. Schaudy, G. Hilscher, N. Pillmayr, P. Rogl, and P. Fischer, J. Magn. Magn. Mater. **104–107**, 11 (1992).

[168] K. Kaneko, N. Metoki, N. Bernhoeft, G. H. Lander, Y. Ishii, S. Ikeda, Y. Tokiwa, Y. Haga, and Y. Ōnuki, Phys. Rev. B **68**, 214419 (2003).

[169] N. Metoki, K. Kaneko, S. Raymond, J.-P. Sanchez, P. Piekarz, K. Parlinski, A. M. Oleś, S. Ikeda, T. D. Matsuda, Y. Haga, et al., Physica B **378–380**, 1003 (2006).

[170] S. Elgazzar, J. Rusz, P. M. Oppeneer, E. Colineau, J.-C. Griveau, N. Magnani, J. Rebizant, and R. Caciuffo, Phys. Rev. B **81**, 235117 (2010).

[171] D. Aoki, Y. Homma, Y. Shiokawa, E. Yamamoto, A. Nakamura, Y. Haga, R. Settai, and Y. Ōnuki, J. Phys. Soc. Jpn. **73**, 2608 (2004).

[172] D. Aoki, Y. Homma, Y. Shiokawa, H. Sakai, E. Yamamoto, A. Nakamura, Y. Haga, R. Settai, and Y. Ōnuki, J. Phys. Soc. Jpn. **74**, 2323 (2005).

[173] I. Opahle, S. Elgazzar, K. Koepernik, and P. M. Oppeneer, Phys. Rev. B **70**, 104504 (2004).

[174] P. Javorský, F. Jutier, P. Boulet, F. Wastin, E. Colineau, and J. Rebizant, Physica B **378–380**, 1007 (2006).

[175] M. Nicklas, V. A. Sidorov, H. A. Borges, P. G. Pagliuso, C. Petrovic, Z. Fisk, J. L. Sarrao, and J. D. Thompson, Phys. Rev. B **67**, 020506(R) (2003).

[176] N. J. Curro, B. Simovic, P. C. Hammel, P. G. Pagliuso, J. L. Sarrao, J. D. Thompson, and G. B. Martins, Phys. Rev. B **64**, 180514 (2001).

[177] P. G. Pagliuso, C. Petrovic, R. Movshovich, D. Hall, M. F. Hundley, J. L. Sarrao, J. D. Thompson, and Z. Fisk, Phys. Rev. B **64**, 100503 (2001).

[178] P. Oppeneer, A. Shick, J. Rusz, S. Lebégue, and O. Eriksson, J. Alloys Compd. **444–445**, 109 (2007).

[179] D. Hall, E. C. Palm, T. P. Murphy, S. W. Tozer, C. Petrovic, E. Miller-Ricci, L. Peabody, C. Q. H. Li, U. Alver, R. G. Goodrich, et al., Phys. Rev. B **64**, 064506 (2001).

[180] R. Settai, H. Shishido, S. Ikeda, Y. Murakawa, M. Nakashima, D. Aoki, Y. Haga, H. Harima, and Y. Ōnuki, J. Phys.: Condens. Matter **13**, L627 (2001).

[181] H. Yasuoka, unpublished.

[182] E. D. Bauer, J. D. Thompson, J. L. Sarrao, L. A. Morales, F. Wastin, J. Rebizant, J. C. Griveau, P. Javorský, P. Boulet, E. Colineau, et al., Phys. Rev. Lett. **93**, 147005 (2004).

[183] R. S. Kumar, H. Kohlmann, B. E. Light, A. L. Cornelius, V. Raghavan, T. W. Darling, and J. L. Sarrao, Phys. Rev. B **69**, 014515 (2004).

[184] M. M. Altarawneh, N. Harrison, R. D. McDonald, F. F. Balakirev, C. H. Mielke, P. H. Tobash, J.-X. Zhu, J. D. Thompson, F. Ronning, and E. D. Bauer, Phys. Rev. B **83**, 081103 (2011).

[185] T. Hayes and J. Boyce, *Solid State Physics* (Academic Press, 1982), vol. 37, p. 173.

[186] G. G. Li, F. Bridges, and C. H. Booth, Phys. Rev. B **52**, 6332 (1995).

[187] E. Crozier, J. Rehr, and R. Ingalls, *X-Ray Absorption: Principles, Applications, Techniques of EXAFS, SEXAFS and XANES* (Wiley, 1988), chap. 9.

[188] E. D. Bauer, C. H. Booth, G. H. Kwei, R. Chau, and M. B. Maple, Phys. Rev. B **65**, 245114 (2002).

[189] M. T. Czyżyk and G. A. Sawatzky, Phys. Rev. B **49**, 14211 (1994).

[190] S. Y. Savrasov and G. Kotliar, Phys. Rev. Lett. **84**, 3670 (2000).

[191] A. B. Shick, V. Janiš, and P. M. Oppeneer, Phys. Rev. Lett. **94**, 016401 (2005).

[192] L. V. Pourovskii, M. I. Katsnelson, and A. I. Lichtenstein, Phys. Rev. B **73**, 060506(R) (2006).

[193] M.-T. Suzuki and P. M. Oppeneer, Phys. Rev. B **80**, 161103(R) (2009).

[194] A. B. Shick, V. Drchal, and L. Havela, Europhys. Lett. **69**, 588 (2005).

[195] J.-X. Zhu, P. H. Tobash, E. D. Bauer, F. Ronning, B. L. Scott, K. Haule, G. Kotliar, R. C. Albers, and J. M. Wills, Europhys. Lett. **97**, 57001 (2012).

[196] I. I. Mazin, Phys. Rev. B **81**, 020507 (2010).

[197] J. Wang, Z. Zeng, and H. Lin, J. Appl. Phys. **99**, 08M505 (2006).

[198] F. Ronning, unpublished.